공학박사학위논문

비선형 정해석 및 동해석을 위한 절대좌표기반 C0 유한요소 개발

Development of C0 ANCF(Absolute nodal coordinate formulation)-based finite elements for nonlinear static and dynamic problems

2019 년 8 월

서울대학교 대학원

기계항공공학부

이 혁

Abstract

In this dissertation, the C0 absolute nodal coordinate formulation (ANCF) element for the nonlinear static and dynamic problem is proposed. Since the ANCF element has an absolute position and its derivative as degrees of freedom, all degrees of freedom appear for the global coordinate. Therefore, this formulation has the advantage that the mass matrix is constant in dynamic simulations. However, existing ANCF elements including differential degrees of freedom have various limitations because they must satisfy C1 continuity. It cannot handle various mesh shapes, and there are many degrees of freedom per node, so more calculation time is required as the elements increase compare to C0 element. In addition, commercial packages are often made up of C0 formulations, so they are not easy to use in commercial packages or in combination with other elements. To overcome these limitations, the C0 formulation of the ANCF element is proposed in this paper.

First, the C0 ANCF 2D plane element and the 3D solid element are formulated by using only the absolute position of each node. For the proposed C0 ANCF element, the equation of motion is solved through Newmark's method and the time response of the structure is verified by a numerical example. In addition, C0 ANCF element is able to simulate the time response of the non-rectangular structure that cannot be covered by the existing ANCF element. It was confirmed that the total energy was conserved for the time response simulation of the conservative system. In addition, the difference between the proposed element and the displacement based element, which is an existing C0 element, is explained.

Second, a plane-beam element and a solid-shell element are proposed by applying the

Enhanced Assumed Strain (EAS) formulation to C0 ANCF plane and solid element. The response to shear locking and volumetric locking is improved in 2D plane beam element static response of C0 ANCF element through applying EAS formulation. In the dynamic response, convergence values are obtained using a smaller number of elements. In the 3D solid-shell element, the results using different numbers of EAS parameters for the static simulation are compared, and the actual solar panel deployment problem for dynamic response is verified.

Finally, researches for improving the performance of the C0 ANCF element are conducted. First, the simulation accuracy is improved by applying the incompatible mode, which can make the absolute position value in the element into the second order. Second, the research to reduce the calculation time is carried out. First, the nonlinear internal force and the tangent stiffness matrix are used as the function of the absolute position using the snapshot data by applying the element-wise stiffness evaluation procedure (E-STEP) method. By doing this, the calculation time is shortened by directing the nonlinear calculation. Next, the calculation time is shortened by reducing the degree of freedom of the equation of motion through proper orthogonal mode (POM) and the singular value obtained by singular value decomposition of the absolute position snapshot by applying the proper orthogonal decomposition (POD) reduction method.

Keywords: Multi-body dynamic simulation, Absolute nodal coordinate formulation, finite element method, Solid-shell element, Reduced order model.

Student Number: 2013-22497

Table of Contents

Table of Contents ..... **iii**

List of Figures ..... **vi**

List of Tables ..... **x**

1. Introduction **1**

1.1. Multi-body dynamic simulation (MBS) 1

1.2. Absolute nodal coordinate formulation (ANCF) 2

1.3. Solid-shell formulation 4

1.4. Reduction of computational time 5

1.5. Motivation and outline of the thesis 7

2. ANCF 2D plane and 3D solid element **10**

2.1. Basic information of ANCF element 10

2.1.1. Plane and Solid ANCF element 10

2.1.2. Limitation of ANCF element 20

2.2. C0 ANCF 2D plane element formulation 22

2.2.1. Four-node quadrangle element 22

2.2.2. Numerical examples 27

2.3. C0 ANCF 3D solid element formulation 34

2.3.1. Eight nodes C0 ANCF solid element 34

2.3.2. Numerical examples 37

2.4. Difference between ANCF and displacement based formulation 40

3. C0 ANCF plane-beam and solid-shell element 65

3.1. Basic information of ANCF beam, plate and shell 66

3.2. Enhanced assumed strain (EAS) formulation with ANCF 68

3.2.1. C0 plane-beam ANCF element 71

3.2.2. C0 solid- shell ANCF element 76

4. Improvement for ANCF element 91

4.1. Incompatible mode 91

4.2. Computational time improvement 94

4.2.1. Proper orthogonal decomposition(POD) reduction method 95

4.2.2. Element-wise stiffness evaluation procedure(E-STEP) method 97

4.2.3. E-STEP and POD mixed formulation 100

4.2.4. Numerical examples 102

5. Concluding remarks 110

Appendix A. Gauss quadrature 113

Appendix B. The Newmark's time integration 115

Appendix C. Singular value decomposition 116

References 117

국문요약 **128**

List of Figures

Figure 2.1. Four node square element in natural coordinate for C1 ANCF element isoperimetric formulation. 43

Figure 2.2. Area coordinate definition in triangle. 43

Figure 2.3. Eight node hexahedron element in natural coordinate for isoperimetric formulation. 44

Figure 2.4. (a) distorted mesh in rectangular structure and (b) non-rectangular structure mesh configuration that cannot be simulated by C1 element 45

Figure 2.5 Computation time comparison with increase of the number of element in C1 element and C0 element 46

Figure 2.6 element degree of freedom in (a) C1 ANCF element and (b) C0 ANCF element 46

Figure 2.7. Four node square element in natural coordinate for C0 ANCF element isoperimetric formulation. 47

Figure 2.8. (a) Example model for patch test and (b) deformed shape and stress distribution of uniaxial tensile test, and (c) model and (d) results for simple shear test. 47

Figure 2.9. Free falling pendulum single-body numerical example problem 48

Figure 2.10. Simulation results of single-body (a) deformation snap-shot, (b) computation time comparison, absolute tip position of (c) x-direction and (d) y-direction 49

Figure 2.11. Energy balance for the free falling pendulum single body 50

Figure 2.12. Free falling multi-body numerical example problem..... 50

Figure 2.13. Simulation results of multi-body pendulum (a) deformation snap-shot, absolute tip position of (b) x-direction and (c) y-direction 51

Figure 2.14. Numerical example problem for non-rectangular mesh configuration, multi-body circle structure. 52

Figure 2.15. Simulation results of multi-body circle (a) deformation snap-shot, absolute tip position of (b) x-direction ,(c) y-direction and (d) energy balance. 53

Figure 2.16. (a) model for vibration simulation and (b) initial state of vibration simulation deformed by initial force. 54

Figure 2.17. Tip position change of 2D plane vibration example (a) without damping (b) and its FFT results, (c) with alpha damping, (d) with beta damping and (e) with alpha and beta damping. 54

Figure 2.18. 3-dimensional dynamic numerical example problem for ANCF simulation(multi-body connected pendulum with regular mesh) 55

Figure 2.19. . Simulation results of 3D multi-body pendulum (a) deformation snap-shot, absolute tip position of (b) x-direction ,(c) y-direction and (d) z-direction. 56

Figure 2.20. 3-dimensional dynamic numerical example problem for ANCF simulation(multi-body connected sphere with non-regular mesh) 57

Figure 2.21. Simulation results of 3-dimensional sphere multi-body (a) deformation snap-shot, absolute tip position of (b) x-direction, (c) y-direction and (d) z-direction 58

Figure 2.22. Energy balance for the of three-dimensional sphere multi-body..... 59

Figure 2.23. (a) 3D vibration example model, and change of the absolute position of center point of disc (a) without damping, (b) with alpha damping, (c) with beta damping, and (e) with alpha and beta damping. 60

Figure 2.24. (a) Simplified wafer transfer robot for practical 3-dimensional motion and vibration example and (b) its deformed shape at T=0.45s 61

Figure 2.25. The absolute position change of WTR tip (a) without Wafer lift(impact) and (b) with wafer lift(impact) at T=0.45s 61

Figure 3.1. Configuration of a ANCF beam element with length : 2 and e=[-1 1 2 -3 1.4 1.4 3 2]^T..... 81

Figure 3.2. Configuration of a ANCF plate element with length : 1, width 1, and e=[-0 0 0 1 0 -1 0 1 1 0 1 -1 1 0 0 1 0 -1 0 1 -1 1 0 1 1 1 0 1 0 -1 0 -1 -1 0 1 1 0 1 0 1 0 -1 0 1 1 1 0 -1]^T 81

Figure 3.3. example problem for shear locking test with various aspect ratio. (a) five versus one, and (b) twenty versus one. 82

Figure 3.4. The tip position change according to the number of element in thickness direction to observe shear locking, (a) results of rive versus one model, and (b) results of twenty versus one model...... 83

Figure 3.5. The results of volumetric locking test. The ratio of tip position in increasing Poisson's ratio. 84

Figure 3.6. Dynamic results of C0 ANCF element and EAS C0 ANCF element. The tip

position of (a) X and (b) Y direction with same number of element and the tip position of (c) X and (d) Y with double the number of element in C0 ANCF element. 85

Figure 3.7. The clamped plate for example problem for 3D EAS-C0 ANCF element static test. 86

Figure 3.8. (a) The center position in thickness direction and (b) the error according to the number of element in length and width direction in the clamped plate test. .. 87

Figure 3.9. (a) The tip position in falling direction according to the number of element and final deformed shape with (b) 2x2 element, (c) 4x4 element, and 8x8 element. .. 88

Figure 3.10. the deployment of solar panel. From initial state to two final states. 89

Figure 3.11. the snap shot of deployment process, sequential deployment for (a) final stat A and (b) final state B and (c) simultaneous deployment for final state B. 90

Figure 4.1. The tapered multi beam example problem to compare results of incompatible mode and C0 ANCF plane element. 105

Figure 4.2. The tip position of (a) X and (b) Y direction of C0 ANCF element and incompatible mode element with same number of element and more element in C0 ANCF element. 106

Figure 4.3. the free falling pendulum single-body numerical example problem to compare computational time of full, E-STEP and E-STEP with POD analysis 107

Figure 4.4. The tip position of (a) X and (b) Y direction with different analysis and (c) computational time of each analysis in one seconds simulation with one second snap shot data. 108

Figure 4.5. The tip position of (a) X and (b) Y direction with different analysis, (c) snapshot of deformed shape of each element, (d) computational time of each analysis in two seconds simulation with one second snapshot data...... 109

List of Tables

Table 2.1. Two-dimensional free falling pendulum properties and simulation coefficients used in single-body simulation 62

Table 2.2. Two-dimensional free falling pendulum properties and simulation coefficients used in multi-body simulation 62

Table 2.3. Two-dimensional free falling multi-body circle properties and simulation coefficients used in simulation 63

Table 2.4. Three-dimensional free falling pendulum properties and simulation coefficients used in multi-body simulation 63

Table 2.5 Three-dimensional free falling sphere properties and simulation coefficients used in multi-body simulation 64

1. Introduction

1.1. Multi-body simulation (MBS)

Multi-body simulations (MBS) are widely used to analyze the relative position, interaction of different bodies. Especially, MBS is an important part of computer-aided design (CAD) and engineering (CAE) and is being applied to a variety of real-world industries such as automobiles, trains, robots, and biotechnology [1]. Most of these MBS applications include nonlinear simulations because they involve large deformations. In the early days, finite element analysis through a computer was very limited due to the limitation of computing power, but it has been widely applied through the rapid growth of computing power. In the early days, finite element analysis through a computer was very limited due to the limitation of computing power. Recently, it has been widely applied through the rapid growth of computing power, and it is possible to be applied to various application such as multi-body dynamic simulation (MBDS).

MBDS can take into account the bodies of three different resolutions. It has a rigid body, flexible body with small deformation with the linear elastic body, and a flexible body with large deformation that includes geometric or material nonlinear deformation [2]. A study on rigid body simulation focusing on how to estimate interaction such as relative position and rotation of multi-bodies has been carried out [3-5].

The flexible multi-body simulation takes into account not only the relative position and interaction of objects but also deformation due to interaction or external forces [6]. Therefore, it is important to model the displacement in the flexible multi-body problem

to include body deformation as well as rotation or rigid body motion. It is applied in various industrial and technical fields such as automobile [7, 8], robotics [9, 10], and aerospace engineering [11-14] and so on [15, 16]. A new different simulation method for flexible multibody dynamics have been developed [17-21] to be applied to mentioned fields and combined with the finite element method [22-26] to be used for practical use. A representative formulation concept is the absolute nodal coordinate formulation, which is discussed in detail in the next section.

1.2. Absolute nodal coordinate formulation (ANCF)

In the early days, the floating frame reference formulation (FFRF) method was widely used to analyze the dynamic response of a beam element. The FFRF method defines displacement in the local coordinate system, defines rigid body motion in the global coordinate system [27]. This method has to consider the Coriolis acceleration because the rigid body motion can change the local coordinate system. Then the mass matrix becomes nonlinear and simulation is very inefficient. In addition, it is difficult to handle large deformation, which makes it difficult to apply geometry nonlinear. To overcome this limitation, Shabana et al. proposed an absolute nodal coordinate formulation (ANCF) [28~31]. ANCF uses the absolute position as the deformation degree of freedom, and its derivatives, the slopes, are used instead of the rotation degree of freedom in the beam element. This differential degree of freedom can be considered as the product of the orthogonal rotation tensor and the stretch tensor, which describes the deformation of the

structure [32]. In addition, because all the degrees of freedom considered in the formulation are defined in the global coordinate, not only one-dimensional deformation but also two or three-dimensional deformation does not have to consider Coriolis acceleration. As a result, the mass matrix is constant for time response deformation and large deformation, and it makes efficient simulation possible. ANCF elements with these advantages have been developed in various fields [28-40] and are widely used in fields requiring multi-body dynamic simulation [49-52].

ANCF has applied various methods to existing beam element and plate or shell element by ANCF researchers. The early ANCF beam element applies the Euler Bernoulli beam theory and employs a linearized strain-displacement relationship [6, 28, 30]. Thereafter, formulations using a nonlinear strain-displacement relation [31, 33] appear, and methods for accounting for shear deformation [34, 35] are proposed.

Plate and shell elements are divided into two types. The first is the method that considers transverse shear insignificantly. In this method, only surface direction slopes are utilized as degrees of freedom [36-39]. The second is the method that considers the transverse shear results in considering not only surface slopes but also thickness direction slope as degrees of freedom [40-42]. Generally, the former is suitable for thin plates and shells and the latter for thicker ones.

ANCF is also applied to plane or solid elements as well as beam, plate and shell elements which include the degree of freedom of rotation [43-46]. ANCF plane and solid element have improved locking effect [47] compared with existing finite element method

and applied to nonlinear damping simulation [48].

1.3. Solid-shell formulation

A typical shell structure is a three-dimensional structure with a two-dimensional or three-dimensional stress state whose thickness is much smaller than the length of another dimension [53]. Since shell structures often appear in engineering analysis, it is important to efficiently analyze shell stress, strain state, and deformation.

The model for shell analysis can be divided into a degenerated shell model and a solid-shell model [54-66]. The degenerated shell model is a method of interpreting the three-dimensional behavior of a structure as a mid-surface description by the following assumptions [56-57]. First, the normal vector of the mid-surface in the initial state is not normal but remains straight in the deformed state, the second is that there is no thickness change, and the third is that the thickness direction stress is ignored. With this assumption, the degenerated shell model can produce good results in most cases, but it has limitations in that it uses rotational degrees of freedom and is formulated at the mid-surface. Boundary condition describing, coupling with three-dimensional elements, rotation degree of freedom in nonlinear analysis and handling of contact analysis is the example. There are also cases where the shell structure needs to solve the problem by applying full three-dimensional constitutive laws including thickness direction.

In order to apply these three-dimensional constitutive equations, a continuum element is required. However, since many elements cannot be used in the thickness direction, studies have been conducted to develop continuum element, whose performance

is similar to degenerated shell element, with one element in thickness direction [53, 58-66]. This element is called a solid-shell element because it is a solid element for shell analysis. Since the solid-shell element does not contain any special assumptions compared to the degenerated shell element, it can be applied as it is, and coupling with other three-dimensional element is easy because it has only displacement freedom.

The most important issue in solid-shell elements is how to handle locking. Volumetric locking and shear locking can be handled through the enhanced assumed strain (EAS) proposed by Simo et al. [60-62]. The EAS formulation solves the locking problem by assuming displacement independent strain modes, and related research to how many modes have to be used in each situation has been conducted [63-66]. As a result, nine, twelve and twenty-one EAS modes have been proposed. Other ways to handle locking include reduced integration, mixed formulation, incompatible mode, and assumed natural strain (ANS).

1.4. Reduction of computational time

The response of the structure of the linear system can be analyzed through a single iteration step, but the analysis of the nonlinear system is performed by iterative calculation of this linear equation. In addition, for dynamic response simulation, iterative computations must be computed every time step, which requires many computer resources to analyze nonlinear dynamic systems [67-69]. Therefore, an important issue in the nonlinear dynamic analysis is to reduce computational resources and computation time. By reducing

computing resources and computation time, problems such as large-scale optimization problems with nonlinear dynamic response, real-time simulation, and the like can be efficiently performed [67-71]. The methods for reducing computing resource and calculation time are typically stiffness evaluation method and model order reduction.

First, the stiffness evaluation method is a method of expressing the nonlinear internal force vector and stiffness matrix as a polynomial function of degrees of freedom [67-69, 72]. The polynomial coefficient, called the stiffness coefficient, is derived from the relationship between snapshot data of internal force and degrees of freedom. Once the coefficient is determined, the global nonlinear internal force can be obtained directly, and the global tangent stiffness matrix can be obtained by differentiation of the polynomial base that consists of degrees of freedom. This saves time dramatically because it does not include the calculation of numerical integration or assembly process that has a large portion on computation time to obtain these values. There are three typical stiffness evaluation methods: stiffness evaluation procedure (STEP), element-wise STEP (E-STEP) and stiffness evaluation based on element connectivity (SEEC).

Second is the model order reduction method, which selecting the representative modes of the full system and reducing the matrix calculated in the full system to a reduced matrix [68]. The model order reduction methods include proper orthogonal decomposition (POD) [74-76], basic method reduction [77], and proper generalized decomposition (PGD) [70] and so on. The POD method is suitable for use together with the stiffness evaluation method because it extracts a representative mode using snapshot data, and it is widely used

for nonlinear problems because it has excellent stability against nonlinear data. The POD method reduces the full system matrix through the proper orthogonal modes (POMs) obtained through singular value decomposition (SVD) of snapshot data. The number of POM to use is determined by the singular value corresponding to the energy ratio of the full system. The stiffness evaluation method and the POD reduction method using snapshot data can be used together to obtain synergy effects.

1.5. Motivation and outline of thesis

The ANCF element has an absolute position in the global coordinate as degrees of freedom, so it does not have to consider Coriolis acceleration, so it has the advantage that the mass matrix is constant throughout the simulation. Because of this advantage, the ANCF element has been researched by many researchers and has been applied in the field of MBDS. However, not much research has been done on elements such as plane, solid, plate and shell except beam elements. This is because the ANCF element must satisfy the C1 continuity because it uses the absolute position as well as the derivatives of the absolute position as its degrees of freedom.

In order to satisfy this C1 continuity, various constraints are followed. First, it cannot handle a distorted mesh. The shape of the element in the global coordinate system determines the shape function obtained from the natural coordinate of the ANCF element. That is, the shape function is a function of the length and width of a rectangle in a 2D element and a function of the length, width, and height of a cube in a 3D element. For a

distorted mesh that is not a rectangle or a cube, it cannot use the shape function in the natural coordinate because length, height, and width of the element cannot be defined. When using a distorted mesh, it is very inefficient to apply a complex Jacobian matrix or to define the shape function for each element separately to satisfy C1 continuity.

The second is the number of degrees of freedom per node. For 2D plane elements, six degrees of freedom per node should be used because they include absolute position, a derivative of x-axis and y-axis. In the case of a 3D solid element, the degree of freedom is twelve per node since each differential and derivative and position of z-axis must be considered. It has 24 degrees of freedom per element in four-node rectangular element from 2D plane analysis, and 96 degrees of freedom per element in the eight-node solid element in the 3D analysis. The increase in the number of degrees of freedom per node greatly affects the calculation efficiency. Figure 2.5 shows the calculation time increase with the increasing number of elements in the C0 element and C1 element. Since the C1 element has more degrees of freedom per node than the C0 element, the total number of degrees of freedom increases much more as the element increases. Therefore, it can be seen that the calculation time of the C1 element increases much more than the calculation time of the C0 element according to increasing the number of the element. Finally, it is the imposition of the boundary condition. In practical terms, constraints on differential degrees of freedom are not intuitive. For example, in the uniaxial tensile test problem, the constraint on differential degrees of freedom should also be considered in the C1 element, although only the absolute position is constrained in the C0 element. Because of these limitations,

commercial packages such as ABAQUS and ANSYS use C0 elements than C1 elements.

In this dissertation, the C0 ANCF element has been proposed to overcome the limitations of the C1 element, while preserving the advantages of the ANCF element resulting from global degrees of freedom. In chapter 2, C0 ANCF plane and solid element are proposed and verified in static and dynamic problems of 2D and 3D. In Chapter 3, plane-beam element and solid-shell element formulation process are introduced by applying the enhanced assumed strain formulation to the C0 ANCF element. In chapter 4, the incompatible mode is applied to improve the performance of the element. In addition, a reduction method and a stiffness evaluation method are applied to shorten the computation time of C0 ANCF element simulation to be efficient.

2. ANCF 2D plane and 3D solid element

In this chapter, the formulation process of the ANCF plane and solid elements is described. First, existing ANCF plane and solid element with C1 continuity will be introduced and limitations of these ANCF elements will be discussed. After that, the formulation process of the C0 ANCF 2D plane element, which has four nodes, and C0 ANCF 3D solid element, which has eight nodes, will be proposed and introduced. The numerical example results for each of the proposed elements will be described. Finally, the differences between the proposed C0 ANCF element and the existing displacement based C0 element will be described.

2.1. Basic information of ANCF element

In this section, the formation process and the limitations of the existing C1 ANCF element is discussed

2.1.1. Plane and solid ANCF element

ANCF elements have an absolute position of each axis and the derivatives of absolute position as degrees of freedom. The number of degrees of freedom per node in a two-dimensional plane element is six, which can be expressed as

$$\mathbf{e}_k = \left\{ \mathbf{r}_k^T \quad \left(\frac{\partial \mathbf{r}_k}{\partial x} \right)^T \quad \left(\frac{\partial \mathbf{r}_k}{\partial y} \right)^T \right\}^T \tag{2.1}$$

, where $\mathbf{r}_k$ is absolute position vector, $\frac{\partial \mathbf{r}_k}{\partial x}$ is x-derivatives of absolute position, and

$\frac{\partial \mathbf{r}_k}{\partial y}$ is y-derivatives of absolute position in global coordinate. Therefore, the degree of freedom of each element can be expressed as

$$\mathbf{e} = \left\{ \mathbf{e}_1^T \quad \mathbf{e}_2^T \quad \mathbf{e}_3^T \quad \mathbf{e}_4^T \right\}^T \tag{2.2}$$

In the three-dimension, the degree of freedom for each node is twelve because it includes $\frac{\partial \mathbf{r}_k}{\partial z}$, which is a z-direction derivative, and can be expressed as

$$\mathbf{e}_k = \left\{ \mathbf{r}_k^T \quad \left(\frac{\partial \mathbf{r}_k}{\partial x} \right)^T \quad \left(\frac{\partial \mathbf{r}_k}{\partial y} \right)^T \quad \left(\frac{\partial \mathbf{r}_k}{\partial z} \right)^T \right\}^T \tag{2.3}$$

The degree of freedom of the eight-node solid element is

$$\mathbf{e} = \left\{ \mathbf{e}_1^T \quad \mathbf{e}_2^T \quad \mathbf{e}_3^T \quad \mathbf{e}_4^T \quad \mathbf{e}_5^T \quad \mathbf{e}_6^T \quad \mathbf{e}_7^T \quad \mathbf{e}_8^T \right\}^T \tag{2.4}$$

The absolute position vector of r, which is the arbitrary point in element, is given by the degrees of freedom of each element in two dimensional as

$$\mathbf{r} = \mathbf{S}(\xi, \eta)\mathbf{e} \tag{2.5}$$

, and three dimensional

$$\mathbf{r} = \mathbf{S}(\xi, \eta, \zeta)\mathbf{e} \tag{2.6}$$

, where $\mathbf{S}$ is shape function, ξ, η and ζ are coordinates of natural coordinates, which can be express as $\xi = x/l$, $\eta = y/w$ and $\zeta = z/h$ respectively, where l, w and h are length, width, and height of the rectangular element or cube element.

- **Shape function of plane element**

The shape function of the ANCF element must satisfy not only the continuity of absolute position, but also the continuity of the derivatives of absolute position. Therefore,

it is necessary to derive a new shape function that is different from the shape function used in the general displacement based finite element. To derive a shape function for a rectangular element, a rectangular element with a width of 1 and a length of 1 in a natural coordinate is assumed as in **Figure 2.1.** Three shape functions (absolute position, x-derivative, y- derivative) must be derived for each node, and since there are four nodes, a polynomial with twelve terms should be assumed. To determine which polynomial base to be used, select the base to be symmetric in the Pascal triangle as

$$\begin{array}{c} 1 \\ \xi \quad \eta \\ \xi^2 \quad \xi\eta \quad \eta^2 \\ \xi^3 \quad \xi^2\eta \quad \xi\eta^2 \quad \eta^3 \\ \xi^3\eta \qquad \xi\eta^3 \end{array} \tag{2.7a}$$

$$\begin{aligned} S_{i,j} = a_0^{i,j} + a_1^{i,j}\xi + + a_2^{i,j}\eta + a_3^{i,j}\xi^2 + a_4^{i,j}\xi\eta + a_5^{i,j}\eta^2 + a_6^{i,j}\xi^3 \\ + a_7^{i,j}\xi^2\eta + a_8^{i,j}\xi\eta^2 + a_9^{i,j}\eta^3 + a_{10}^{i,j}\xi^3\eta + a_{11}^{i,j}\xi\eta^3 \end{aligned} \tag{2.7b}$$

According to the definition of the shape function, the coefficients of each shape function can be determined to satisfy one at each node and zero at other nodes as

$$\begin{aligned} &S_{1,1}(0,0)=1, \;\; S_{2,1}(0,0)=0, \;\; S_{3,1}(0,0)=0, \;\; S_{4,1}(0,0)=0 \\ &\frac{\partial S_{1,2}(0,0)}{\partial\xi}=1, \;\; \frac{\partial S_{2,2}(0,0)}{\partial\xi}=0, \;\; \frac{\partial S_{3,2}(0,0)}{\partial\xi}=0, \;\; \frac{\partial S_{4,2}(0,0)}{\partial\xi}=0 \\ &\frac{\partial S_{1,3}(0,0)}{\partial\eta}=1, \;\; \frac{\partial S_{2,3}(0,0)}{\partial\eta}=0, \;\; \frac{\partial S_{3,3}(0,0)}{\partial\eta}=0, \;\; \frac{\partial S_{4,3}(0,0)}{\partial\eta}=0 \end{aligned} \tag{2.8}$$

The shape function of the four-node ANCF plane element determined by **Equation 2.7** and **8** as

$$
\begin{aligned}
&S_{1,1} = -(1-\xi)(1-\eta)\left(2\xi^2+2\eta^2-\xi-\eta-1\right), \quad S_{1,2} = l\xi(1-\xi)^2(1-\eta) \\
&S_{1,3} = w\eta(1-\xi)(1-\eta)^2 \\
&S_{2,1} = -\xi(1-\eta)\left(2\xi^2+2\eta^2-3\xi-\eta\right), \quad S_{2,2} = -l\xi^2(1-\xi)(1-\eta) \\
&S_{2,3} = w\xi\eta(1-\eta)^2 \\
&S_{3,1} = -\xi\eta\left(2\xi^2+2\eta^2-3\xi-3\eta+1\right), \quad S_{3,2} = -l\xi^2\eta(1-\xi) \\
&S_{3,3} = -w\xi\eta^2(1-\eta) \\
&S_{4,1} = -\eta(1-\xi)\left(2\xi^2+2\eta^2-\xi-3\eta\right), \quad S_{4,2} = l\xi\eta(1-\xi)^2 \\
&S_{4,3} = -w\eta^2(1-\xi)(1-\eta)
\end{aligned}
\tag{2.9}
$$

In conclusion, the shape function matrix for the ANCF plane element becomes

$$
\mathbf{S} = \begin{bmatrix} S_{1,1}\mathbf{I}_2 & S_{1,2}\mathbf{I}_2 & S_{1,3}\mathbf{I}_2 & S_{2,1}\mathbf{I}_2 & S_{2,2}\mathbf{I}_2 & S_{2,3}\mathbf{I}_2 \\ S_{3,1}\mathbf{I}_2 & S_{3,2}\mathbf{I}_2 & S_{3,3}\mathbf{I}_2 & S_{4,1}\mathbf{I}_2 & S_{4,2}\mathbf{I}_2 & S_{4,3}\mathbf{I}_2 \end{bmatrix} \tag{2.10}
$$

, where $\mathbf{I}_2$ is 2 by 2 identity matrix.

The shape function of the triangular element is derived by base on the Specht's shape function. In the derivation process of the triangular element, we use a triangle area coordinate as shown in **Figure 2.2.** The coordinates of the arbitrary point inside the triangle are calculated as

$$
\mathbf{r} = \mathbf{r}_1\Delta_1 + \mathbf{r}_2\Delta_2 + \mathbf{r}_3\Delta_3 \tag{2.11}
$$

, where Δ_i is ratio of triangle area, which satisfy

$$
\begin{aligned}
&\Delta_1 + \Delta_2 + \Delta_3 = 1 \\
&\Delta_i = \frac{\Delta_i^*}{\Delta}, \quad 0 \le \Delta_i \le 1
\end{aligned}
\tag{2.12}
$$

, where Δ is area of triangle element. Δ_i can derived as a function of position of global coordinate through **Equation 2.11 and 2.12** as

$$\Delta_i = \frac{c_{i1}x + c_{i2}y + c_{i3}}{2\Delta} \tag{2.13}$$

, where $c_{i1} = y_j - y_k$, $c_{i2} = x_k - x_j$, $c_{i3} = x_j y_k - x_k y_j$. Finally, the shape function of a triangle element satisfying C1 continuity can be expressed as

$$\begin{aligned} S_{i,1} &= \Delta_i - \Delta_i\Delta_j + \Delta_k\Delta_i + 2P_i - 2P_k \\ S_{i,2} &= c_{j2}\left(P_k - \Delta_k\Delta_i\right) + c_{k2}P_i \\ S_{i,3} &= -c_{j1}\left(P_k - \Delta_k\Delta_i\right) - c_{k1}P_i \end{aligned} \tag{2.14}$$

using a triangle coordinate, where

$$\begin{aligned} P_i &= \Delta_j^2\Delta_j + \frac{1}{2}\Delta_i\Delta_j\Delta_k\left[3\left(1-\mu_k\right)\Delta_i + \left(1+3\mu_k\right)\left(\Delta_k - \Delta_j\right)\right] \\ \mu_k &= \frac{\left(l_j^2 - l_i^2\right)}{l_k^2} \end{aligned} \tag{2.15}$$

The shape function matrix can be derived similar to **Equation 2.10**.

- **Shape function of solid element**

The derivation of the shape function of the eight-node solid element is very similar to that of the four-node rectangular plane element. For the derivation of shape function, a hexahedron whose length is two in natural coordinate and whose center of gravity is at the origin as shown in Figure 2.3 is assumed. Since four shape functions (absolute position, x-derivative, y-derivative and z-derivative) per node must be induced from eight nodes, a polynomial with thirty-two terms has to be assumed. To determine which polynomial base to be used, select the base to be symmetric in the Pascal triangle same Equation 2.7 as

$$
\begin{array}{ccccccccccc}
 & & & & & & \xi^3 & & & & \\
 & & & & \xi^2 & & & & & & \\
 & & & \xi & & & \xi^2\eta & \xi^2\zeta & & & \\
1 & & \eta & & \zeta & \xi\eta & \xi\zeta & \xi\eta^2 & \xi\eta\zeta & \xi\zeta^2 & \\
 & & & \eta^2 & \eta\zeta & \zeta^3 & \eta^3 & \eta^2\zeta & \eta\zeta^2 & \zeta^3 & \\
 & & & & & & \xi^3\eta & \xi^3\zeta & & & \\
 & & & & & & & \xi^3\eta\zeta & & & \\
 & & & & & & \xi^2\eta\zeta & & & & \\
 & & & & & \xi\eta^3 & \xi\eta^2\zeta & \xi\eta\zeta^2 & \xi\zeta^3 & & \\
 & & & & \xi\eta^3\zeta & & & & \xi\eta\zeta^3 & & \\
 & & & \eta^3\zeta & & & \eta\zeta^3 & & & &
\end{array}
\tag{2.16a}
$$

$$
\begin{aligned}
S_{i,j} &= a_0^{i,j} + a_1^{i,j}\xi + a_2^{i,j}\eta + a_3^{i,j}\zeta \\
&+ a_4^{i,j}\xi^2 + a_5^{i,j}\xi\eta + a_6^{i,j}\xi\zeta + a_7^{i,j}\eta^2 + a_8^{i,j}\eta\zeta + a_9^{i,j}\zeta^3 \\
&+ a_{10}^{i,j}\xi^3 + a_{11}^{i,j}\xi^2\eta + a_{12}^{i,j}\xi^2\zeta + a_{13}^{i,j}\xi\eta^2 + a_{14}^{i,j}\xi\eta\zeta + a_{15}^{i,j}\xi\zeta^2 + a_{16}^{i,j}\eta^3 + a_{17}^{i,j}\eta^2\zeta + a_{18}^{i,j}\eta\zeta^2 + a_{19}^{i,j}\zeta^3 \\
&+ a_{20}^{i,j}\xi^3\eta + a_{21}^{i,j}\xi^3\zeta + a_{22}^{i,j}\xi^2\eta\zeta + a_{23}^{i,j}\xi\eta^3 + a_{24}^{i,j}\xi\eta^2\zeta + a_{25}^{i,j}\xi\eta\zeta^2 + a_{26}^{i,j}\xi\zeta^3 + a_{27}^{i,j}\eta^3\zeta + a_{28}^{i,j}\eta\zeta^3 \\
&+ a_{29}^{i,j}\xi^3\eta\zeta + a_{30}^{i,j}\xi\eta^3\zeta + a_{31}^{i,j}\xi\eta\zeta^3
\end{aligned}
\tag{2.16b}
$$

According to the definition of the shape function, the coefficients of each shape function can be determined to satisfy one at each node and zero at other nodes same as **Equation 2.8**. The shape function of the three-dimensional eight-node solid element can be express as

$$
\begin{aligned}
S_{i,1} &= \frac{1}{16}(1\pm\xi)(1\pm\eta)(1\pm\zeta)\left(2\pm\xi\pm\eta\pm\zeta-\xi^2-\eta^2-\zeta^2\right) \\
S_{i,2} &= \pm\frac{1}{32}l\left(1-\xi^2\right)(1\pm\xi)(1\pm\eta)(1\pm\zeta) \\
S_{i,3} &= \pm\frac{1}{32}w\left(1-\eta^2\right)(1\pm\xi)(1\pm\eta)(1\pm\zeta) \\
S_{i,4} &= \pm\frac{1}{32}t\left(1-\zeta^2\right)(1\pm\xi)(1\pm\eta)(1\pm\zeta)
\end{aligned}
\tag{2.17}
$$

In conclusion, the shape function matrix of eight-node ANCF solid element becomes

$$\mathbf{S} = \begin{bmatrix} S_{1,1}\mathbf{I}_3 & S_{1,2}\mathbf{I}_3 & S_{1,3}\mathbf{I}_3 & S_{1,4}\mathbf{I}_3 & S_{2,1}\mathbf{I}_3 & S_{2,2}\mathbf{I}_3 & S_{2,3}\mathbf{I}_3 & S_{2,4}\mathbf{I}_3 & \cdots \\ \cdots & S_{7,1}\mathbf{I}_3 & S_{7,2}\mathbf{I}_3 & S_{7,3}\mathbf{I}_3 & S_{7,4}\mathbf{I}_3 & S_{8,1}\mathbf{I}_3 & S_{8,2}\mathbf{I}_3 & S_{8,3}\mathbf{I}_3 & S_{8,4}\mathbf{I}_3 \end{bmatrix} \tag{2.18}$$

, where $\mathbf{I}_3$ is 3 by 3 identity matrix.

- **Equation of motion**

Since the ANCF element is formulated in global coordinates, kinetic energy can be easily obtained as a product of velocity, since it does not need to consider Coriolis acceleration, as

$$T = \frac{1}{2}\int_V \rho \dot{\mathbf{r}}^T \dot{\mathbf{r}} dV \tag{2.19}$$

, where $\dot{\mathbf{r}}$ is the velocity vector which is corresponding to derivative over time of absolute position vector, ρ is density, and V is volume of structure in unreformed configuration. The velocity vector can be express as

$$\dot{\mathbf{r}} = \frac{\partial \mathbf{r}}{\partial t} = \frac{\partial \mathbf{S}\mathbf{e}}{\partial t} = \mathbf{S}\frac{\partial \mathbf{e}}{\partial t} = \mathbf{S}\dot{\mathbf{e}} \tag{2.20}$$

By substituting **Equation 18** for **Equation 19**, the mass matrix $\mathbf{M}$ can be derived as

$$\begin{aligned} \mathrm{T} &= \frac{1}{2}\int_V \rho \left(\mathbf{S}\dot{\mathbf{e}}\right)^T \mathbf{S}\dot{\mathbf{e}} dV = \frac{1}{2}\int_V \rho \dot{\mathbf{e}}^T \left(\mathbf{S}\right)^T \mathbf{S}\dot{\mathbf{e}} dV = \frac{1}{2}\dot{\mathbf{e}}^T \left[\int_V \rho \left(\mathbf{S}\right)^T \mathbf{S} dV\right]\dot{\mathbf{e}} = \frac{1}{2}\dot{\mathbf{e}}^T \mathbf{M}\dot{\mathbf{e}} \\ \mathbf{M} &= \int_V \rho \left(\mathbf{S}\right)^T \mathbf{S} dV \end{aligned} \tag{2.21}$$

Since the shape function $\mathbf{S}$ is derived from a natural coordinate and the integration is defined in the global coordinate, the coordinate must be modified to coincide. Because the C1 ANCF element uses only rectangular in plane and cube elements in solid problem, it has a constant Jacobian, so the coordinates can be modified as

$$\mathbf{M} = \int_0^1 \int_0^1 \int_0^1 \rho\left(\mathbf{S}\left(\xi,\eta,\zeta\right)\right)^T \mathbf{S}\left(\xi,\eta,\zeta\right)\left|V\right| d\xi d\eta d\zeta$$
$$\left|V\right| = l \cdot w \cdot t \tag{2.22}$$

The equation of motion can be expressed as

$$\mathbf{M}\ddot{\mathbf{e}} + \mathbf{C}\left(\mathbf{e}\right)\dot{\mathbf{e}} + \mathbf{Q}_i\left(\mathbf{e}\right) = \mathbf{Q}_e \tag{2.23}$$

, including the mass matrix, the damping matrix, the internal force, and the external force vector. The damping matrix and internal force are functions related to the absolute position and the mass matrix has a constant value regardless of the absolute position.

The damping matrix uses the Rayleigh damping model, which is derived through the stiffness matrix and the mass matrix. The Rayleigh damping model can be expressed as the sum of mass and tangent stiffness ($\mathbf{K}^t$) matrix as

$$\mathbf{C} = \alpha\mathbf{M} + \beta\mathbf{K}^t \tag{2.24}$$

, where α is the mass proportional coefficient and β is stiffness proportional coefficient of Rayleigh damping model. Generally, the α and β value is derived from the damping ratio (ξ_i) because it is not directly known. The natural frequency and damping ratio of the structure are related to the α and β as

$$\xi_i = \frac{\alpha}{2\omega_i} + \frac{\beta\omega_i}{2} \tag{2.25}$$

where, ω_i is the natural circular frequency of mode i.

The internal force can be induced through the internal energy of the structure. From the viewpoint of the continuum mechanics, the internal energy of the structure can be expressed as

$$U = \frac{1}{2}\int_V \boldsymbol{\varepsilon}^T \mathbf{E}\boldsymbol{\varepsilon} dV \tag{2.26}$$

, where $\boldsymbol{\varepsilon}$ is a nonlinear strain calculated from Green-Lagrange strain as

$$\boldsymbol{\varepsilon} = \frac{1}{2}\begin{bmatrix} \mathbf{r}_{,x}^T\mathbf{r}_{,x}^T - 1 \\ \mathbf{r}_{,y}^T\mathbf{r}_{,y}^T - 1 \\ 2\mathbf{r}_{,x}^T\mathbf{r}_{,y}^T \end{bmatrix} \tag{2.27a}$$

$$\boldsymbol{\varepsilon} = \frac{1}{2}\begin{bmatrix} \mathbf{r}_{,x}^T\mathbf{r}_{,x} - 1 \\ \mathbf{r}_{,y}^T\mathbf{r}_{,y} - 1 \\ \mathbf{r}_{,z}^T\mathbf{r}_{,z} - 1 \\ 2\mathbf{r}_{,x}^T\mathbf{r}_{,y} \\ 2\mathbf{r}_{,y}^T\mathbf{r}_{,z} \\ 2\mathbf{r}_{,z}^T\mathbf{r}_{,x} \end{bmatrix} \tag{2.27b}$$

in case of two-dimensional problem and three-dimensional problem. $\mathbf{E}$ is a matrix of elastic constants as

$$\mathbf{E} = \frac{E}{1-\nu^2}\begin{bmatrix} 1 & \nu & 0 \\ \nu & 1 & 0 \\ 0 & 0 & 2(1-\nu) \end{bmatrix}, \quad \mathbf{E} = \frac{E}{(1+\nu)(1-2\nu)}\begin{bmatrix} 1 & \nu & 0 \\ \nu & 1 & 0 \\ 0 & 0 & \frac{(1-2\nu)}{2} \end{bmatrix} \tag{2.28a, b}$$

$$\mathbf{E} = \frac{E}{(1+\nu)(1-2\nu)}\begin{bmatrix} 1-\nu & \nu & \nu & & & \\ \nu & 1-\nu & \nu & & & \\ \nu & \nu & 1-\nu & & & \\ & & & 2(1-2\nu) & & \\ & & & & 2(1-2\nu) & \\ & & & & & 2(1-2\nu) \end{bmatrix} \tag{2.28c}$$

, two-dimensional plane stress problem, two-dimensional plane strain problem, and three-dimensional solid problem respectively, where E is Young's modulus and ν is Poisson's ratio. The internal force vector can be obtained by differentiating internal strain energy into each degree of freedom.

$$\mathbf{Q} = \frac{\partial U}{\partial \mathbf{e}} = \int_V \left(\frac{\partial \boldsymbol{\varepsilon}}{\partial \mathbf{e}} \right)^T \mathbf{E} \boldsymbol{\varepsilon} dV \tag{2.29}$$

The derivative of strain can be obtained as

$$\frac{\partial \boldsymbol{\varepsilon}}{\partial \mathbf{e}} = \begin{bmatrix} \mathbf{r}_x^T \mathbf{S}_x \\ \mathbf{r}_y^T \mathbf{S}_y \\ \frac{1}{2}\left(\mathbf{r}_x^T \mathbf{S}_y + \mathbf{r}_y^T \mathbf{S}_x \right) \end{bmatrix} \tag{2.30a},$$

$$\frac{\partial \boldsymbol{\varepsilon}}{\partial \mathbf{e}} = \begin{bmatrix} \mathbf{r}_x^T \mathbf{S}_x \\ \mathbf{r}_y^T \mathbf{S}_y \\ \mathbf{r}_z^T \mathbf{S}_z \\ \frac{1}{2}\left(\mathbf{r}_x^T \mathbf{S}_y + \mathbf{r}_y^T \mathbf{S}_x \right) \\ \frac{1}{2}\left(\mathbf{r}_y^T \mathbf{S}_z + \mathbf{r}_z^T \mathbf{S}_y \right) \\ \frac{1}{2}\left(\mathbf{r}_z^T \mathbf{S}_x + \mathbf{r}_x^T \mathbf{S}_z \right) \end{bmatrix} \tag{2.30b}$$

, where $\mathbf{S}_x$, $\mathbf{S}_y$, and $\mathbf{S}_z$ are derivatives of the shape function matrix $\mathbf{S}$. Since the shape functions are function of xi eta zeta, the derivative for x, y and z can be obtained through the change rule.

$$\begin{aligned} \mathbf{S}_x &= \frac{\partial \mathbf{S}}{\partial x} = \frac{\partial \mathbf{S}}{\partial \xi}\frac{\partial \xi}{\partial x} + \frac{\partial \mathbf{S}}{\partial \eta}\frac{\partial \eta}{\partial x} + \frac{\partial \mathbf{S}}{\partial \zeta}\frac{\partial \zeta}{\partial x} \\ \mathbf{S}_y &= \frac{\partial \mathbf{S}}{\partial y} = \frac{\partial \mathbf{S}}{\partial \xi}\frac{\partial \xi}{\partial y} + \frac{\partial \mathbf{S}}{\partial \eta}\frac{\partial \eta}{\partial y} + \frac{\partial \mathbf{S}}{\partial \zeta}\frac{\partial \zeta}{\partial y} \\ \mathbf{S}_z &= \frac{\partial \mathbf{S}}{\partial z} = \frac{\partial \mathbf{S}}{\partial \xi}\frac{\partial \xi}{\partial z} + \frac{\partial \mathbf{S}}{\partial \eta}\frac{\partial \eta}{\partial z} + \frac{\partial \mathbf{S}}{\partial \zeta}\frac{\partial \zeta}{\partial z} \end{aligned} \tag{2.31}$$

However, since the ANCF element can only be used for rectangle and cube elements, it will be zero for values other than the global axis and corresponding axis as

$$\frac{\partial \eta}{\partial x} = \frac{\partial \zeta}{\partial x} = 0, \quad \frac{\partial \mathbf{S}}{\partial \xi} = \frac{\partial \mathbf{S}}{\partial \zeta} = 0, \quad \frac{\partial \xi}{\partial z} = \frac{\partial \eta}{\partial z} = 0 \tag{2.32}$$

Therefore, the derivative of the shape function can be simplified as

$$\mathbf{S}_x = \frac{\partial \mathbf{S}}{\partial x} = \frac{\partial \mathbf{S}}{\partial \xi}\frac{\partial \xi}{\partial x} = \frac{\mathbf{S}_\xi}{l}, \quad \mathbf{S}_y = \frac{\partial \mathbf{S}}{\partial y} = \frac{\partial \mathbf{S}}{\partial \eta}\frac{\partial \eta}{\partial y} = \frac{\mathbf{S}_\eta}{w},$$
$$\mathbf{S}_z = \frac{\partial \mathbf{S}}{\partial z} = \frac{\partial \mathbf{S}}{\partial \zeta}\frac{\partial \zeta}{\partial z} = \frac{\mathbf{S}_\zeta}{t} \tag{2.33}$$

Finally, the internal force $\mathbf{Q}$ can be calculated by integration as

$$\mathbf{Q} = \frac{\partial U}{\partial \mathbf{e}} = \int_0^1\int_0^1\int_0^1 \left(\frac{\partial \boldsymbol{\varepsilon}}{\partial \mathbf{e}}\right)^T \mathbf{E}\boldsymbol{\varepsilon}|V|\, d\xi d\eta d\zeta \tag{2.34}$$
$$V = l \cdot w \cdot t$$

2.1.3. Limitation of ANCF element

The ANCF element must satisfy C1 continuity because it uses derivatives of absolute position as well as the absolute position as a degree of freedom. Therefore, it has limitations in general use.

The first is the limit of the shape of the mesh. As described above, the shape function of the conventional ANCF element is expressed as a function of the length and width of the square element in the case of two dimensions, and the length, width, and height in the case of the three dimensions, as shown in **Equations 2.9 and 2.16.** If a distorted mesh is used, it is very inefficient because a different shape function must be derived for each element in order to satisfy C1 continuity. Therefore, the ANCF element that satisfies C1 continuity cannot analysis or simulate a distorted mesh as shown in **Figure 2.4(a)** or a structure that cannot be represented by a combination of rectangle elements as shown in **Figure 2.4(b)**.

The second is the degradation of computational efficiency with the increasing

number of degrees of freedom per node. Since the C1 ANCF element uses not only the absolute position but also the derivative of the position, the degree of freedom is six per node in 2D and twelve degrees of freedom per node in 3D. Therefore, for an element, twenty-four degrees of freedom in 2D and ninety-six degrees of freedom in 3D must be calculated. This is three times and four times that of the conventional displacement-based formulation, compared to using eight per element in 2D and twenty-four per node in 3D. Since the C1 ANCF element has a large number of degrees of freedom per node, the total number of degrees of freedom increases sharply as the number of nodes increases. The total number of degrees of freedom has a direct effect on the calculation time as shown in Figure 2.5. Compared with the case of using three elements and the case of using 27 elements, the C0 element was 67 times different, but the C1 element was 162 times different. Therefore, by using a C1 element that uses many degrees of freedom per node, the calculation efficiency can be drastically reduced.

Finally, there is a limit to apply to commercial packages. In commercial packages such as ABAQUS and ANSYS, most of them are implemented as C0 elements for plane and solid problems. Therefore, the C1 ANCF element has limitations to use with existing commercial packages.

2.2. C0 ANCF 2D plane element formulation

In order to overcome the various limitations of the C1 element, this dissertation proposes a C0 ANCF 2D plane element. The C0 ANCF 2D plane element uses only the absolute position as degrees of freedom, so that it has only two degrees of freedom compared to six degrees of freedom per node in existing ANCF plane element. In addition, since the shape function does not have to satisfy the C1 continuity, any distorted mesh can be handled very efficiently because it can use the shape function of the natural coordinate directly with applying Jacobian. This section describes the formulation process of the C0 ANCF 2D plane element, and numerical examples.

2.2.1. Four-node quadrangle element

Since the C0 ANCF 2D plane element has only an absolute position as a degree of freedom. **Equation (2.1)** can be reduced as

$$\mathbf{e}_k^0 = \left\{ \mathbf{r}_k{}^T \right\}^T \tag{2.35}$$

, where $\mathbf{e}_k^0$ is degree of freedom in C0 ANCF 2D plane element. The degree of freedom of an element can be expressed by the degree of freedom of each node as

$$\mathbf{e}^0 = \left\{ \left(\mathbf{e}_1^0\right)^T \quad \left(\mathbf{e}_2^0\right)^T \quad \left(\mathbf{e}_3^0\right)^T \quad \left(\mathbf{e}_4^0\right)^T \right\}^T \tag{2.36}$$

For an arbitrary point in an element, C1 ANCF element는 an absolute position of an arbitrary point in an element can be expressed by equation (2.2) and (2.5) with twenty-four degrees of freedom in the existing ANCF plane element as shown in **Figure 2.6 (a)**. In the

case of the C0 ANCF 2D plane element, it can be expressed by eight degrees of freedom as shown in **Figure. 2.6 (b)**, and can be expressed as

$$\mathbf{r} = \mathbf{S}^0\mathbf{e}^0 \tag{2.37}$$

, where $\mathbf{S}^0$ is a shape function matrix of C0 ANCF 2D plane element.

- **Shape function of four node quadrangle C0 ANCF element**

The shape function of the C0 ANCF plane element can be easily obtained by transforming **Figure 2.6 (b)** into a square element of -1 to 1 for the xi and eta axis of the natural coordinate as shown in **Figure 2.7**. In the C0 ANCF plane element formulation process, the range of natural coordinates is [- 1, 1], unlike [0, 1] of existing ANCF, which facilitates the application of numerical integration. Because only the absolute position is used as degrees of freedom, only C0 continuity need to be satisfied. Therefore, only four polynomial bases can express shape function as

$$S_i^0 = a_0^i + a_1^i\xi + a_2^i\eta + a_3^i\xi\eta \tag{2.38}$$

By determining the coefficient through the condition of the shape function, the shape function can be obtained as

$$\begin{aligned} S_1^0 &= \frac{(1-\xi)(1-\eta)}{4}, \quad S_2^0 = \frac{(1+\xi)(1-\eta)}{4}, \\ S_3^0 &= \frac{(1+\xi)(1+\eta)}{4}, \quad S_4^0 = \frac{(1-\xi)(1+\eta)}{4} \end{aligned} \tag{2.39}$$

, where the shape function matrix can be expressed as

$$\mathbf{S}^0 = \begin{bmatrix} S_1^0\mathbf{I}_2 & S_2^0\mathbf{I}_2 & S_3^0\mathbf{I}_2 & S_4^0\mathbf{I}_2 \end{bmatrix} \tag{2.40}$$

This is equivalent to the shape function of a displacement based formulation.

- **Equation of motion**

The equation of motion of the C0 ANCF plane element is similar to the equation of motion of C1 ANCF described in **section 2.1**. However, since the degree of freedom uses only the absolute position compare to absolute position and its derivative of C1 ANCF element, the shape function changes to the previously derived shape function of C0 ANCF plane element and a distorted mesh can be used, so the Jacobian in the integration must be considered.

First, the shape function of the C0 ANCF plane element is applied to the kinetic energy as

$$\begin{aligned} \mathrm{T} &= \frac{1}{2}\int_V \rho\left(\mathbf{S}^0\dot{\mathbf{e}}\right)^T \mathbf{S}^0\dot{\mathbf{e}}dV = \frac{1}{2}\int_V \rho\dot{\mathbf{e}}^T\left(\mathbf{S}^0\right)^T \mathbf{S}^0\dot{\mathbf{e}}dV \\ &= \frac{1}{2}\dot{\mathbf{e}}^T\left[\int_V \rho\left(\mathbf{S}^0\right)^T \mathbf{S}^0 dV\right]\dot{\mathbf{e}} = \frac{1}{2}\dot{\mathbf{e}}^T\mathbf{M}\dot{\mathbf{e}} \\ \mathbf{M} &= \int_V \rho\left(\mathbf{S}^0\right)^T \mathbf{S}^0 dV \end{aligned} \tag{2.41}$$

Since the shape function is derived from the natural coordinate and the integral period is the global coordinate, the mass matrix of **Equation 2.41** can be calculated by applying Jacobian as

$$\mathbf{M} = \int_V \rho\left(\mathbf{S}^0\right)^T \mathbf{S}^0 dV = t\int_{-1}^{1}\int_{-1}^{1} \rho\left(\mathbf{S}\left(\xi,\eta\right)^0\right)^T \left(\mathbf{S}\left(\xi,\eta\right)^0\right)\det\mathbf{J}d\xi d\eta \tag{2.42}$$

, where t is thickness of the structure, and $\mathbf{J}$ is a Jacobian matrix which calculated as

$$\mathbf{J} = \begin{bmatrix} \dfrac{\partial x}{\partial\xi} & \dfrac{\partial y}{\partial\xi} \\ \dfrac{\partial x}{\partial\eta} & \dfrac{\partial y}{\partial\eta} \end{bmatrix} = \begin{bmatrix} J_{11} & J_{12} \\ J_{21} & J_{22} \end{bmatrix} \tag{2.43}$$

The Gaussian quadrature, a numerical integral method is applied to obtain the mass matrix. Since Gaussian quadrature is commonly used in CAE and CAD fields such as finite element analysis, an explanation of this is attached to **Appendix A**.

The internal energy is also very similar to that of **Equation form 2.29 to 2.34**. If the shape function of the previously used C1 ANCF element, S, is changed to shape function C0 ANCF plane element, S0, internal energy and internal force can be obtained in the C0 formulation. In the process of deriving the strain and strain derivative to handle distorted mesh, these are calculated by chain rule as

$$\begin{aligned}\mathbf{S}_x^0 &= \frac{\partial \mathbf{S}^0}{\partial x} = \frac{\partial \mathbf{S}^0}{\partial \xi}\frac{\partial \xi}{\partial x} + \frac{\partial \mathbf{S}^0}{\partial \eta}\frac{\partial \eta}{\partial x} \\ \mathbf{S}_y^0 &= \frac{\partial \mathbf{S}^0}{\partial y} = \frac{\partial \mathbf{S}^0}{\partial \xi}\frac{\partial \xi}{\partial y} + \frac{\partial \mathbf{S}^0}{\partial \eta}\frac{\partial \eta}{\partial y}\end{aligned} \tag{2.44}$$

Finally, the internal force applying Jacobian can be expressed as

$$\mathbf{Q} = \frac{\partial U}{\partial \mathbf{e}} = t\int_{-1}^{1}\int_{-1}^{1}\left(\frac{\partial \boldsymbol{\varepsilon}}{\partial \mathbf{e}}\right)^T \mathbf{E}\boldsymbol{\varepsilon}\left(\det \mathbf{J}\right) d\xi d\eta \tag{2.45}$$

The damping matrix is calculated as shown in **Equation 2.24** by the Rayleigh damping model as mentioned in **section 2.1**.

- **Time integration scheme**

In order to simulation this nonlinear equation of motion, iterative evaluation of deformed states according to time is required. In general, the Newton-Raphson method is used to solve these iterative nonlinear problems. For the iterative calculation in the equation of motion, **Equation 2.23**, the internal force can be expressed as a function of tangent stiffness, the absolute position change, and the absolute position of the previous step as

$$\mathbf{M}\ddot{\mathbf{e}}_{T+\Delta T}+\mathbf{C}\left(\mathbf{e}_T\right)\dot{\mathbf{e}}_{T+\Delta T}+\mathbf{K}^t\left(\mathbf{e}_T\right)\Delta\mathbf{e}+\mathbf{Q}_i\left(\mathbf{e}_T\right)=\mathbf{Q}_e \tag{2.46}$$

,where $\mathbf{K}^t\left(\mathbf{e}_T\right)$ is tangent stiffness matrix, T is calculated time, ΔT is time interval, $\Delta\mathbf{e}$ is an increment of absolute position, and $\mathbf{e}_T$ is an absolute position at time T. The tangent stiffness is obtained from the derivative of the degree of freedom of the internal force as

$$\mathbf{K}^t\left(\mathbf{e}_T\right)=\left.\frac{\partial\mathbf{Q}}{\partial\mathbf{e}}\right|_{\mathbf{e}=\mathbf{e}_T} \tag{2.47}$$

Tangent stiffness matrix can be obtained using numerical derivatives because analytical derivatives of internal force are difficult to obtain.

To obtain the time-dependent value of the equation of motion, **Equation 2.46**, the time integration method should be used. In this study, Newmark's-beta time integration scheme, which is highly stable and widely applied, is utilized, and detail explanation of it is attached in **Appendix B**. The acceleration and velocity at the current time step can be represented by the value of the previous step by the Newmark's beta formulation as

$$\ddot{\mathbf{e}}_{T+\Delta T}=\frac{\Delta\mathbf{e}}{\beta\left(\Delta T\right)^2}-\frac{\dot{\mathbf{e}}_T}{\beta\left(\Delta T\right)}-\frac{1}{\beta}\left(\frac{1}{2}-\beta\right)\ddot{\mathbf{e}}_T \tag{2.48a}$$

$$\dot{\mathbf{e}}_{T+\Delta T}=\dot{\mathbf{e}}_T+\left(\Delta T\right)\left[\left(1-\gamma\right)\ddot{\mathbf{e}}_T+\gamma\frac{\Delta u}{\beta\left(\Delta T\right)^2}-\gamma\frac{\dot{\mathbf{e}}_T}{\beta\left(\Delta T\right)}-\frac{\gamma}{\beta}\left(\frac{1}{2}-\beta\right)\ddot{\mathbf{e}}_T\right] \tag{2.48b}$$

, where γ and β is Newmark's coefficient. By substituting the above **Equation 2.32** into **2.30** and summarizing increment of absolute position, it can be expressed as

$$\Delta\mathbf{e}=\left[\frac{\mathbf{M}}{\beta(\Delta t)^2}+\frac{\mathbf{C}\gamma}{\beta(\Delta t)}+\mathbf{K}^t\right]^{-1}\left[\begin{array}{l}\mathbf{F}_{i+1}-\mathbf{F}_{\text{int}}+\mathbf{M}\left[\frac{\dot{\mathbf{e}}_T}{\beta(\Delta t)}+\frac{1}{\beta}\left(\frac{1}{2}-\beta\right)\ddot{\mathbf{e}}_T\right]\\ -\mathbf{C}\left[\left(1-\frac{\gamma}{\beta}\right)\dot{\mathbf{e}}_T+\left(1-\frac{1}{2}\frac{\gamma}{\beta}\right)\ddot{\mathbf{e}}_T\right]\end{array}\right] \quad (2.49)$$

By repeating Equations 30-33 until Equation 30 meets the equilibrium, the response of the structure over time can be obtained.

2.2.2. Numerical examples

Some dynamic problems have been simulated by using the C0 ANCF plane element proposed this study. The simulation results are compared with the existing C1 ANCF element calculation for the regular mesh. Regular mesh, distorted mesh, and non-square structure are simulated with C0 ANCF plane element and confirmed to converge. The C0 ANCF plane element confirms that the total energy is maintained for gravity conservation problems

- **Static patch test**

In order to verify that the proposed C0 ANCF element can get accurate results from static, uniaxial tensile test and simple shear test are performed. For the uniaxial tensile test, a model with a distorted mesh is assumed as shown in **Figure 2.8 (a)**. The y-direction position of the bottom surface constrained so that there is no change, and the x-direction position of the left side also constrained from changing. A force of the same magnitude 5e7N acts on the two nodes at the right end in the x direction. The result of the stress distribution is shown in **Figure 2.8 (b)**. From the results of stress distribution, it can be

seen that the same stress value can be obtained up to six significant figures for the distorted mesh. This results in an order that is the same as the order of the numerical differentiation used when calculating the tangent stiffness.

Next, accuracy of the calculation of shear is confirmed by simple shear test. For the simple shear test, a model such as **Figure 2.8 (c)** is assumed. The bottom surface is fixed with respect to the x and y directions, and the upper surface is kept horizontal. The side surfaces are constrained to be parallel. For the upper two nodes, the 1e7N force is applied in the x direction. As can be seen from the stress distribution of the deformed shape in **Figure 2.8 (d)**, it is confirmed that up to 6 significant figures can be obtained exactly like the uniaxial tensile test. Therefore, the proposed C0 ANCF element gives a reliable result for static analysis.

- **Free falling pendulum single-body**

As a first example, the 2D beam falling by gravity is assumed as shown in **Figure 2.9**. The left end of the beam is fixed by a pin joint and falls by gravity. The physical property and the length information used in the simulation are shown in **Table 2.1.** In the original configuration, the velocity of the beam is zero, and the acceleration is $9.81 m/s^2$ acts due to the gravitational acceleration.

In order to compare the results of the C0 ANCF element and the C1 ANCF element, the shape change snapshot of the free pendulum for 1.4 seconds is shown in **Figure 2.10 (a)**, and the calculation time of each element are described in **Figure 2.10 (b)**.

Finally, the change in the vertical and horizontal positions of the tip is shown in **Figures 2.10 (c) and (d)**. As shown in **Figures 2.10 (a), (c) and (d)**, the results of the C1 ANCF element and the C0 ANCF element are well matched. Because the C1 ANCF element uses more degrees of freedom, when the same number of elements is used, this makes C1 ANCF element more accurate, which is advantageous, but requires more computation time as shown in **Figure 2.10 (b)**.

Finally, to verify the accuracy of the C0 ANCF element, the results of free pendulum single-body is observed as an energy point of view. The free falling pendulum that is driven by gravity is a conservation system that the sum of energy is constant. There are three types of energy. : Kinetic energy, strain energy, potential energy. The kinetic energy can be obtained from **Equation 2.21**, which are used in the previous formulation process. The strain energy can be obtained as shown in **Equation 2.26**, and strain can be obtained in each element through the absolute position at each step. The potential energy can be calculated through how much the center of mass is moved from initial state to deformed state in each element as

$$\mathrm{V}^i = m^i g \Delta y_G^i, \quad \mathrm{V}=\sum_{i=1}^{n} \mathrm{V}^i \tag{2.50}$$

, where V^i is element potential energy, m^i is mass of an element, Δy_G^i is the difference of vertical position of mass center between the initial state and deformed state which can be calculated as

$$\Delta y^i = y_G^T - y_G^0 \tag{2.51}$$

, where y_G^T and y_G^0 are the vertical position of the mass center of the deformed state and initial state respectively. Since the system is a conservation system, the sum of the three energy types must be constant as

$$\mathrm{T} + U + \mathrm{V} = const. \tag{2.52}$$

In this case, the constant value is zero because all the energies in the initial state are assumed to be zero. **Figure 2.11** shows the change of three energy types and the total energy according to time, which is obtained from the C0 ANCF plane element. As shown in **Figure 2.11**, the total energy is well maintained at zero over time. Therefore, it is proved that the simulation including the large deformation through the C0 ANCF plane element can simulate the physics well.

- **Free falling pendulum multi-body**

It is verified that the results of the time response in single-body are well matched to existing simulation methods. In order to verify whether the proposed element fits well in a multi-body simulation, a multibody system with two 2D beams falling by gravity is assumed as shown in **Figure 2.12**. The left end of the left pendulum A is fixed with a pin joint, and the right end of A and the left end of B are connected. The physical property information and the length information used in the simulation are shown in Table 2.2. The velocity of the beam in the original configuration is zero, and the acceleration to the vertical direction is 9.81m/s2 by the gravitational acceleration as in the single-body simulation.

To compare the results of the C0 ANCF element and the C1 ANCF element, a shape change snapshot of the free pendulum for 1.2 seconds is shown in **Figure 2.13 (a)**,

and the vertical and horizontal positions of the tip are shown in **Figures 2.13 (b)** and **(c)**. The results are presented together with beam ANCF element results for comparison. As shown in **Figure 2.13 (a) to (c),** the results of the C1 ANCF element and the C0 ANCF element agree very well with the reference solution ANCF beam multi-body simulation results. Therefore, the C0 ANCF element gives a reliable result in multibody simulation as well as a single body.

- **Free falling circle multi-body**

It is verified that the results of the time response in a multi-body using a regular mesh with proposed C0 ANCF element are well matched to the results of the existing C1 ANCF element. This time, a circle-type structure that can not be simulated by the C1 ANCF element is assumed, in order to verify that the C0 ANCF element can handle it. As shown in **Figure 2.14**, two circle-type multibody systems falling by gravity are assumed. The left end of the left circle C1 is fixed with a pin joint, and the right end of C1 is connected to the left end of C2. The physical property information and the length information used in the simulation are shown in **Table 2.3**. In the original configuration, the velocity of C1 and C2 is zero, and the acceleration to the vertical direction is 9.81m/s2 by the gravitational acceleration as the previous simulation.

Since the circle shape cannot be interpreted as a C1 ANCF element, the result using the C0 ANCF element is shown in **Figure 2.15**. A one-second shape change snapshot of the C0 ANCF element simulation is shown in **Figure 2.15 (a)**, and the vertical and horizontal position changes of the tip are shown in **Figure 2.15 (b) and (c)**. In addition, the

change in energy over time is also shown in **Figure 2.15 (d)**. As shown in **Figure 2.15 (a) to 14 (c)**, converged results with non-rectangular mesh can be obtained through C0 ANCF element simulation. The change of energy with time in **Figure 2.15 (d)** shows that the total energy is preserved to zero through the simulation. This proves that the dynamic simulation of a distorted mesh or non-rectangular shape structure that cannot be interpreted as a C1 ANCF element through the C0 ANCF element can be achieved.

- **Vibration with damping**

In order to verify that the C0 ANCF element achieves the same results as the existing vibration simulation results for the vibration problem with damping, the vibration and damping simulation for the cantilever beam model is performed. As shown in **Figure 2.16 (a)**, the Young's modulus is assumed to be 70GPa, Poisson's ratio 0.3, and density 2700kg/m^3. First, the vibration simulation is performed assuming that the deformation in the **Figure 2.16 (b)** obtained by the static analysis with the force of 100KN at the end is assumed to be the initial state. **Figure 2.17 (a)** shows the result of the absolute position change on the y-axis obtained from the simulation without damping. **Figure 2.17 (b)** shows the results of the fast Fourier transform (FFT) of time-dependent absolute position change. The ANCF simulation is a simulation involving geometric nonlinearity, but it is compared with the first order natural frequency of the linear system because the variation of the absolute position is relatively small in the vibration simulation. The natural frequency obtained from the FFT obtained in **Figure 2.17 (b)** is 333 Hz, and the analytical first-order natural frequency obtained through the linear assumption is 328.97 Hz, which is very

similar to the one shown in **Figure 2.17 (b)**.

For the damping simulation, the Rayleigh damping mentioned in **Equation from 2.24 to 25** is applied. To determine the Rayleigh damping coefficient α and β, the values are determined so that the damping ratio by α and β is 0.02, respectively. By substituting the first-order natural frequencies obtained by the non-damping simulation previously performed to Equation 2.25, α and β values of 9.64e-6 and 82.93 are obtained, respectively. First, simulation results using only mass proportional damping (α) is shown in **Figure 2.17 (c)**. The amplitude of the vibration decreased with time. The damping ratio can be obtained by the decreasing amplitude as

$$\delta = \frac{1}{n} \ln \frac{A(t)}{A(t+nT)}$$

$$\zeta = \frac{1}{\sqrt{1+\left(\frac{2\pi}{\delta}\right)^2}}$$

,where A is amplitude of vibration, n is the number of vibration, and T is frequency of vibration. The obtained damping ratio is 0.02, and it can be confirmed that the theoretical damping ratio and the damping ratio obtained through the simulation coincide with each other.

Next, stiffness proportional damping simulation through β is performed. The simulation result is shown in **Figure 2.17 (d)**. Compared to the result of mass proportional damping, the damping ratio obtained by simulation is 0.022, which is somewhat different from the theoretical damping ratio of 0.02. This is because the theoretical damping ratio

does not consider the nonlinearity. Since the same values are used for the mass matrix in the linear and nonlinear simulations throughout the simulation, the same results can be obtained in the linear and nonlinear analysis respect to damping. However, since the tangent stiffness is calculated differently from the linear system in the simulation considering the geometric nonlinearity, the stiffness proportional damping, which is affected by the tangent stiffness matrix, differs from the damping ratio obtained from the linear assumption.

Finally, simulation is performed considering mass and stiffness proportional damping simultaneously. The change in the tip position in y-axis is shown in **Figure 2.17 (e)**. Simulation results show that the damping ratio is 0.042. This is equal to the sum of the damping ratios obtained from the mass proportional damping and the stiffness proportional damping. Based on these results, accurate results of vibration and vibration with damping simulation can be obtained through the C0 ANCF plane element.

2.3. C0 ANCF 3D solid element formulation

In this section, the formulation process of the C0 ANCF 3D solid element for three-dimensional analysis is described. A four-node quadrilateral ANCF element for the plane analysis is proposed in the previous section and a corresponding eight-node hexahedron element for 3D analysis is proposed in this section. In addition, numerical examples are demonstrated to verify the C0 ANCF solid element is suitable for 3D dynamic simulation.

2.3.1. Eight node C0 ANCF solid element

As with the C0 ANCF plane element, since only the absolute position is utilized as degrees of freedom, the degree of freedom per node is reduced like **Equation 2.36**, and the degree of freedom per element of eight node elements is given by

$$\mathbf{e}^0 = \left\{ \left(\mathbf{e}_1^0\right)^T \quad \left(\mathbf{e}_2^0\right)^T \quad \left(\mathbf{e}_3^0\right)^T \quad \left(\mathbf{e}_4^0\right)^T \quad \left(\mathbf{e}_5^0\right)^T \quad \left(\mathbf{e}_6^0\right)^T \quad \left(\mathbf{e}_7^0\right)^T \quad \left(\mathbf{e}_8^0\right)^T \right\}^T \quad (2.53)$$

For an arbitrary point within an element, the absolute position of it can be represented by ninety-six degrees of freedom per element, twelve degrees of freedom per node, in the C1 ANCF solid element. However, it can be represented by twenty-four degrees of freedom per element, three degrees of freedom per node, in C0 ANCF solid element as expressed in **Equation 2.37**.

- **Shape function of eight node C0 ANCF solid element**

The shape function of C0 ANCF can be easily obtained by transforming the element in the global coordinate to the cube of which range is from -1 to 1 in the natural coordinates as shown in **Figure2.3**. Since only the absolute position is used as the degree of freedom, it should satisfy only C0 continuity. Since the shape function obtained through this process is consistent with the shape function obtained from the displacement based formulation, the shape function of the well-known eight-node brick element can be used as is. The shape function of each node and the shape function matrix of the eight-node C0 ANCF 3D solid element are expressed as

$$
\begin{aligned}
S_1^0 &= \frac{(1-\xi)(1-\eta)(1-\zeta)}{8} \quad S_2^0 = \frac{(1+\xi)(1-\eta)(1-\zeta)}{8} \\
S_3^0 &= \frac{(1+\xi)(1+\eta)(1-\zeta)}{8} \quad S_4^0 = \frac{(1-\xi)(1+\eta)(1-\zeta)}{8} \\
S_5^0 &= \frac{(1-\xi)(1-\eta)(1+\zeta)}{8} \quad S_6^0 = \frac{(1+\xi)(1-\eta)(1+\zeta)}{8} \\
S_7^0 &= \frac{(1+\xi)(1+\eta)(1+\zeta)}{8} \quad S_8^0 = \frac{(1-\xi)(1+\eta)(1+\zeta)}{8}
\end{aligned}
\tag{2.54a}
$$

$$
\mathbf{S}^0 = \begin{bmatrix} S_1^0\mathbf{I}_3 & S_2^0\mathbf{I}_3 & S_3^0\mathbf{I}_3 & S_4^0\mathbf{I}_3 & S_5^0\mathbf{I}_3 & S_6^0\mathbf{I}_3 & S_7^0\mathbf{I}_3 & S_8^0\mathbf{I}_3 \end{bmatrix} \tag{2.54b}
$$

- **Equation of motion**

The detail formulation process of the equation of motion of the C0 ANCF plane element is described in **Section 2.2.1**. Therefore, it can be applied to the C0 ANCF solid element by expanding the 2D integral to the 3D integral in the process of obtaining the mass matrix and internal force. The mass matrix **Equation 2.42** and the internal force vector **Equation 2.45** are expanded to three dimensions as

$$
\mathbf{M} = \int_V \rho\left(\mathbf{S}^0\right)^T \mathbf{S}^0 dV = \int_{-1}^{1}\int_{-1}^{1}\int_{-1}^{1} \rho\left(\mathbf{S}(\xi,\eta)^0\right)^T \left(\mathbf{S}(\xi,\eta)^0\right) \det\mathbf{J} d\xi d\eta d\zeta \tag{2.55a}
$$

$$
\mathbf{Q} = \frac{\partial U}{\partial \mathbf{e}} = \int_{-1}^{1}\int_{-1}^{1}\int_{-1}^{1} \left(\frac{\partial \boldsymbol{\varepsilon}}{\partial \mathbf{e}}\right)^T \mathbf{E}\boldsymbol{\varepsilon}\left(\det\mathbf{J}\right) d\xi d\eta d\zeta \tag{2.55b}
$$

The three-dimensional Jacobian matrix can be obtained as

$$
\mathbf{J} = \begin{bmatrix} \dfrac{\partial x}{\partial \xi} & \dfrac{\partial y}{\partial \xi} & \dfrac{\partial z}{\partial \xi} \\ \dfrac{\partial x}{\partial \eta} & \dfrac{\partial y}{\partial \eta} & \dfrac{\partial z}{\partial \eta} \\ \dfrac{\partial x}{\partial \zeta} & \dfrac{\partial y}{\partial \zeta} & \dfrac{\partial z}{\partial \zeta} \end{bmatrix} = \begin{bmatrix} J_{11} & J_{12} & J_{13} \\ J_{21} & J_{22} & J_{23} \\ J_{31} & J_{32} & J_{33} \end{bmatrix} \tag{2.56}
$$

The differential equation of the shape function to obtain derivative of the strain can be extended to three dimensions from Equation 2.44 to

$$\begin{aligned}
\mathbf{S}_x^0 &= \frac{\partial \mathbf{S}^0}{\partial x} = \frac{\partial \mathbf{S}^0}{\partial \xi}\frac{\partial \xi}{\partial x} + \frac{\partial \mathbf{S}^0}{\partial \eta}\frac{\partial \eta}{\partial x} + \frac{\partial \mathbf{S}^0}{\partial \zeta}\frac{\partial \zeta}{\partial x} \\
\mathbf{S}_y^0 &= \frac{\partial \mathbf{S}^0}{\partial y} = \frac{\partial \mathbf{S}^0}{\partial \xi}\frac{\partial \xi}{\partial y} + \frac{\partial \mathbf{S}^0}{\partial \eta}\frac{\partial \eta}{\partial y} + \frac{\partial \mathbf{S}^0}{\partial \zeta}\frac{\partial \zeta}{\partial y} \\
\mathbf{S}_z^0 &= \frac{\partial \mathbf{S}^0}{\partial z} = \frac{\partial \mathbf{S}^0}{\partial \xi}\frac{\partial \xi}{\partial z} + \frac{\partial \mathbf{S}^0}{\partial \eta}\frac{\partial \eta}{\partial z} + \frac{\partial \mathbf{S}^0}{\partial \zeta}\frac{\partial \zeta}{\partial z}
\end{aligned} \tag{2.57}$$

2.3.2. Numerical examples

For the verification of the C0 ANCF solid element proposed in Section 2.3.1, it is applied to the 3D dynamic problem. First, the three-dimensional behavior problem of the falling pendulum multi-body problem is assumed for comparing the results of the regular mesh simulated by C0 and C1 ANCF solid element. For a non-rectangular structure, a multi-body three-dimensional behavior problem with two spherical objects with non-constant Jacobian is assumed for verifying convergence of the C0 ANCF element.

- **Free falling pendulum multi-body**

The problem as shown in **Figure 2.18** is assumed in order to verify whether C0 ANCF solid element can obtain the converged result in the multi-body and be matched well to the results of the existing C1 ANCF element. The multi-body structure shown in **Figure 2.18** falls by gravity in the vertical direction (z-direction) and one-third of the gravity acceleration in the horizontal direction (y-direction). The left end of the left pendulum A is fixed with a pin joint, and the right end of pendulum A and the left end of pendulum B are

connected. The simulation is performed by constraining the end node so that it can not rotate in the longitudinal direction with respect to the fixed end as shown in **Figure 2.18**. The physical property information and the length information used in the simulation are shown in **Table 2.4**. The velocity in the initial state is zero, and the acceleration acts by the gravitational acceleration in the vertical direction and by one-third of gravitational acceleration in the horizontal y-direction.

To compare the results of the C0 and C1 ANCF solid element, a shape change snapshot for 1.2 seconds is shown in **Figure 2.19 (a)**, and the tip positions of x-, y-, and z-direction are shown in **Figures 2.19 (b)-(d)**. As shown in **Figures 2.19 (a)-(d)**, the results of C1 and C0 ANCF solid element are very consistent about both absolute position and deformed snapshot over time.

- **Free falling sphere multi-body**

Similar to the 2D example, a multi-body system as shown in **Figure 2.20** is assumed for verifying that the C0 ANCF solid element gives a converged solution of the dynamic problem, which includes not only the regular mesh but also the distorted mesh. This model is a multi-body system with two spheres with an arbitrary mesh. **Table 2.5** shows the physical properties and simulation coefficients. The deformed shape snapshot of the multi-body according to the time change and the change of the absolute position of the right sphere end are shown in **Figure 2.21**. As shown in the figure, the converged solution of the non-regular mesh dynamic simulation can be obtained through the C0 ANCF solid element. In addition, as shown in **Figure 2.22**, it can be seen that the C0 ANCF solid

element simulation satisfies the physical law even from the viewpoint of energy through the preservation of the sum of energy in the conservation system as zero.

- **Vibration with damping**

As with the C0 ANCF plane element, the vibration damping simulation of the C0 ANCF solid element is verified. A three-dimensional model including a distorted mesh is assumed through a 1/4 disc model as shown in **Figure 2.23 (a)**. The radius is assumed to be 0.05 m and the thickness 0.001 m, assuming a length ratio of 50 to 1, Young's modulus to 1.4 MPa, Poisson's ratio to 0.3, and density to 7100 kg/m^3. First, the same result is obtained as **Figure 2.23 (b)** through simulation without damping. As shown in **Figure 2.23 (c),** the damping ratio 0.0108 is obtained when alpha value is 1. Then, as shown in **Figure 2.23 (d),** the damping ratio 0.0290 is obtained when the beta value is 0.003. Finally, damping ratio of 0.043 is obtained by damping simulation with alpha and beta.

- **3D practical example with vibration**

The proposed C0 ANCF solid element is applied to the practical problem where vibration occurs while performing 3D motion. Wafer transfer robot(WTR) is a robot that can move each arm to move the wiper to a desired position. Such a WTR is subjected to three-dimensional motion, and vibrations are generated by an impact when the wiper is lifted. Therefore, the motion and vibration analysis of the WTR has an important influence on the control and design of the robot. It is difficult to simulate using the actual WTR model. Therefore, simulation is performed by simplifying the WTR robot as shown in **Figure 2.24 (a).** Simulation is simulated for 0.45 seconds to attain the same posture as **Figure 2.24 (b)**

and return to the original state. The change in the absolute position of the tip in the z direction at this simulation is shown in **Figure 2.25 (a)**. As shown in the figure, when the wiper is not lifted up, the amplitude of vibration is about 0.001, which is very small. Next, a simulation is performed in which the WTR is vibrated by applying a force of 10 N for 0.01 s while lift up the wiper after it posture as **Figure 2.24 (b)** at 0.45s. At this time, the amplitude of the vibration after the impact is increased by about 0.004 or more, as shown in **Figure 2.25 (b)**. Therefore, it is expected that this simulation can predict the change of WTR by attitude control and vibration, and it can be expected to improve the performance and design the robot with high reliability by reflecting it to the design.

2.4. Difference between ANCF and displacement based formulation

The C0 ANCF plane and solid element are proposed in the previous sections. In this section, the differences between the existing C0 element, displacement-based plane and solid element, and the proposed C0 ANCF element are described.

A typical difference is a degree of freedom. The displacement-based formulation literally has displacement as a degree of freedom, and the C0 ANCF element has an absolute position. The displacement-based formulation represents the displacement of the arbitrary point in the element as

$$\mathbf{U}=\begin{bmatrix} u \\ v \end{bmatrix}=\begin{bmatrix} N_1\mathbf{I}_2 & N_2\mathbf{I}_2 & N_3\mathbf{I}_2 & N_4\mathbf{I}_2 \end{bmatrix}\begin{bmatrix} u_1 \\ v_1 \\ \vdots \\ u_4 \\ v_4 \end{bmatrix}=\mathbf{Nu} \tag{2.58}$$

Since the orders of degrees of freedom are matched, the shape function $\mathbf{N}$ of the displacement-based formulation and the shape function $\mathbf{S}^0$ of the C0 ANCF element have the same shape. Therefore, the process of calculating kinetic energy and mass are agreed.

However, this difference in degrees of freedom affects the strain form. In the C0 ANCF element proposed in this dissertation, the strain is obtained from the vectorizing Green-Lagrangian strain obtained from the deformation gradient, as mentioned in the previous section. However, in the displacement-based formulation, the strain is defined by introducing a $\mathbf{B}$, a differential of shape function matrix, and a $\mathbf{B}_N$, a nonlinear term of strain, for nonlinear formulation as

$$\boldsymbol{\varepsilon}=\left(\mathbf{B}+\mathbf{B}_N\right)\mathbf{u} \tag{2.59}$$

$$\mathbf{B}=\begin{bmatrix} \frac{\partial N_1}{\partial x} & & \cdots & \frac{\partial N_n}{\partial x} & \\ & \frac{\partial N_1}{\partial y} & \cdots & & \frac{\partial N_n}{\partial y} \\ \frac{\partial N_1}{\partial y} & \frac{\partial N_1}{\partial x} & \cdots & \frac{\partial N_n}{\partial y} & \frac{\partial N_n}{\partial x} \end{bmatrix} \tag{2.60}$$

$$\mathbf{B}_N = \begin{bmatrix} F_{11}\dfrac{\partial N_1}{\partial x} & F_{21}\dfrac{\partial N_1}{\partial x} & \cdots & F_{11}\dfrac{\partial N_4}{\partial x} & F_{21}\dfrac{\partial N_4}{\partial x} \\ F_{12}\dfrac{\partial N_1}{\partial y} & F_{22}\dfrac{\partial N_1}{\partial y} & \cdots & F_{12}\dfrac{\partial N_4}{\partial y} & F_{22}\dfrac{\partial N_4}{\partial y} \\ F_{11}\dfrac{\partial N_1}{\partial y}+F_{12}\dfrac{\partial N_1}{\partial x} & F_{21}\dfrac{\partial N_1}{\partial y}+F_{22}\dfrac{\partial N_1}{\partial x} & \cdots & F_{11}\dfrac{\partial N_4}{\partial y}+F_{12}\dfrac{\partial N_4}{\partial x} & F_{21}\dfrac{\partial N_4}{\partial y}+F_{22}\dfrac{\partial N_4}{\partial x} \end{bmatrix} \quad (2.61)$$

, where F_{ij} is i and jth components of deformation gradient.

This difference in strain definition also affects the internal force and tangent stiffness matrix obtained through the differentiation of internal energy. In the C0 ANCF element, the internal force and tangent stiffness are obtained by direct differentiation of internal energy as shown in **Equation 2.45 and 47**. In the displacement-based formulation, the internal force and the tangent stiffness are obtained by linearization as

$$\mathbf{Q}_{\text{int}} = \int \left[\mathbf{B}_N\right]^T \mathbf{S} dV \quad (2.62a)$$

$$\mathbf{K}_{\tan} = \int \left[\mathbf{B}_N\right]^T \mathbf{E}\left[\mathbf{B}_N\right] dV + \int \left[\mathbf{B}_G\right]^T \left[\Sigma\right]\left[\mathbf{B}_G\right] dV \quad (2.63b)$$

, where

$$\mathbf{B}_G = \begin{bmatrix} \dfrac{\partial N_1}{\partial x} & & \cdots & \dfrac{\partial N_4}{\partial x} & \\ \dfrac{\partial N_1}{\partial y} & & \cdots & \dfrac{\partial N_4}{\partial y} & \\ & \dfrac{\partial N_1}{\partial x} & \cdots & & \dfrac{\partial N_4}{\partial x} \\ & \dfrac{\partial N_1}{\partial y} & \cdots & & \dfrac{\partial N_4}{\partial y} \end{bmatrix} \quad (2.64)$$

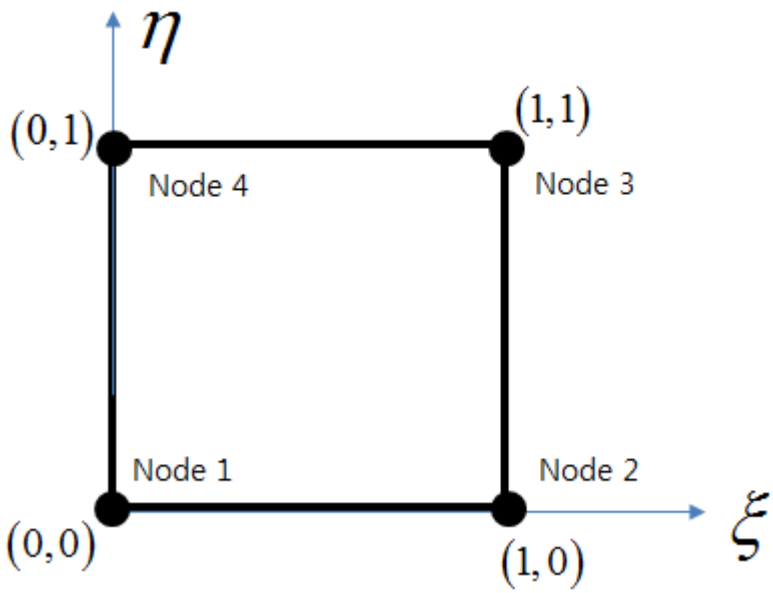

Figure 2.1. Four node square element in natural coordinate for C1 ANCF element isoperimetric formulation.

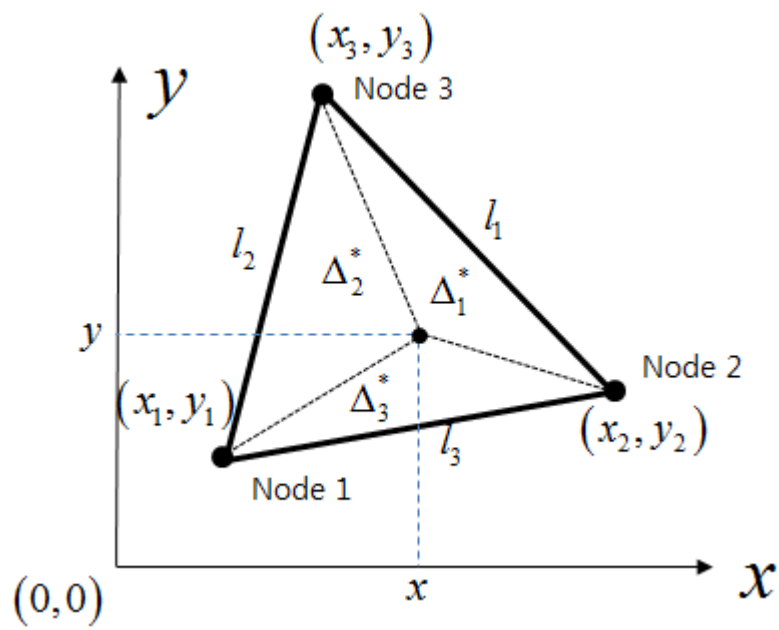

Figure 2.2. Area coordinate definition in triangle.

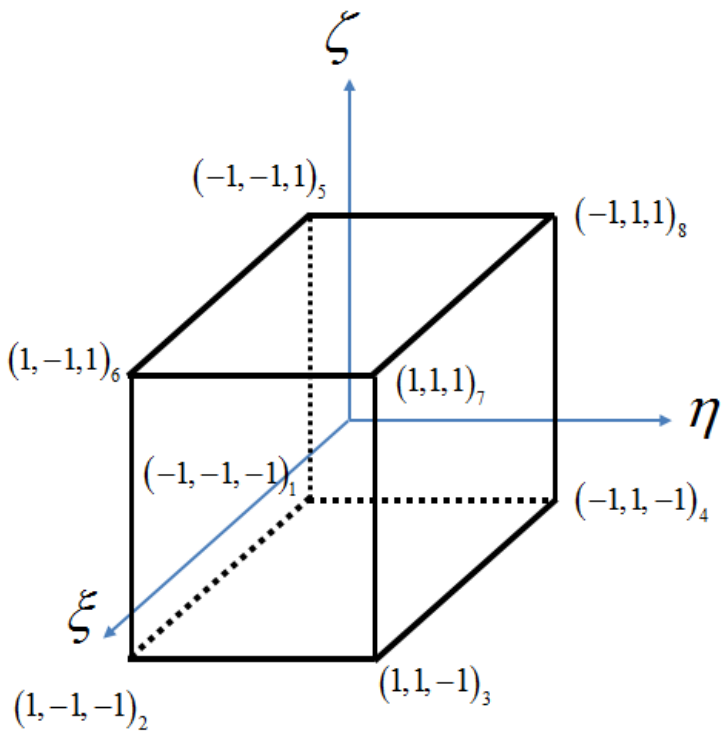

Figure 2.3. Eight node hexahedron element in natural coordinate for isoperimetric formulation.

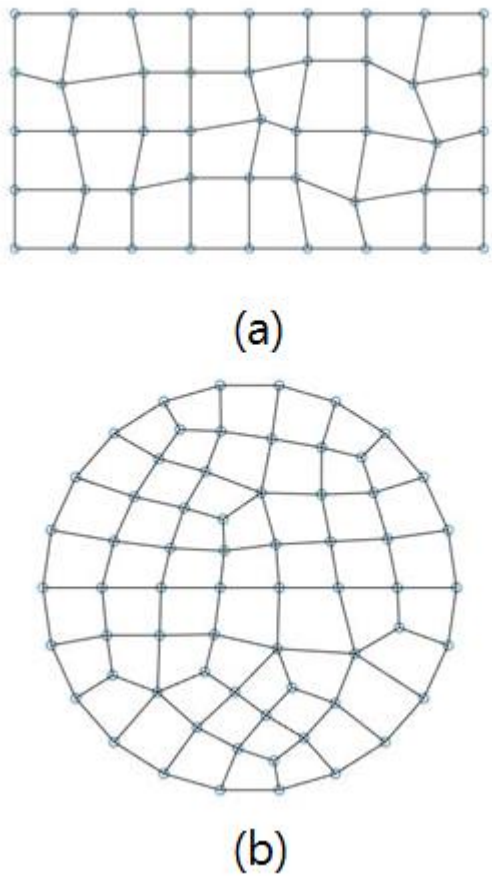

Figure 2.4. (a) distorted mesh in rectangular structure and (b) non-rectangular structure mesh configuration that cannot be simulated by C1 element

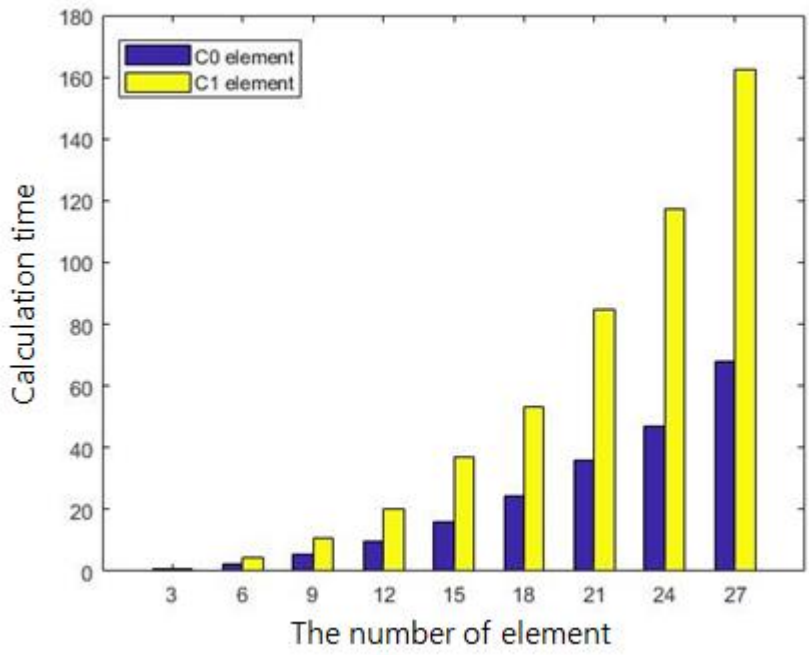

Figure 2.5. Computation time comparison with increase of the number of element in C1 element and C0 element

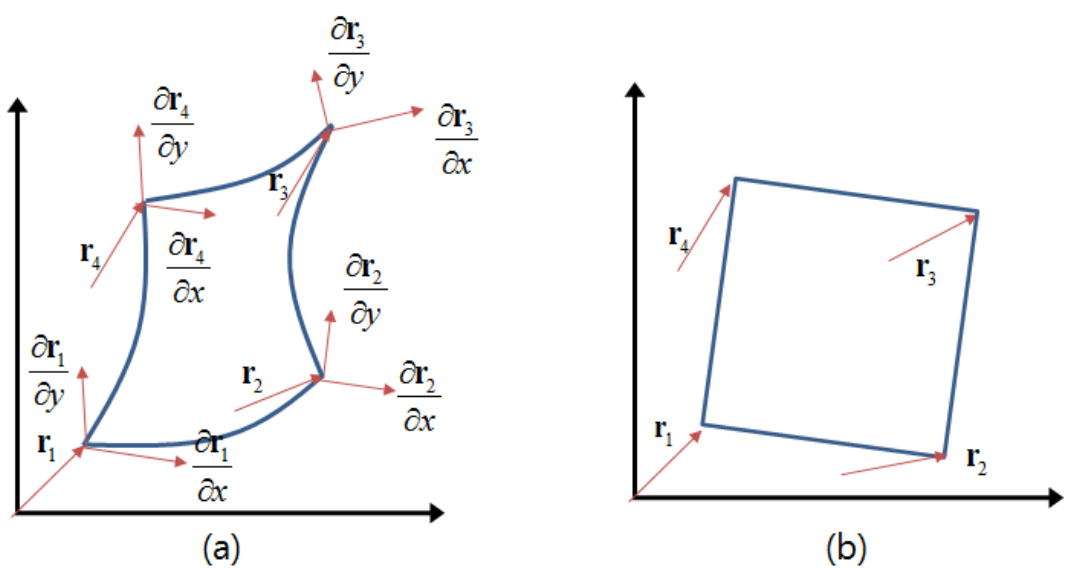

Figure 2.6. element degree of freedom in (a) C1 ANCF element and (b) C0 ANCF element

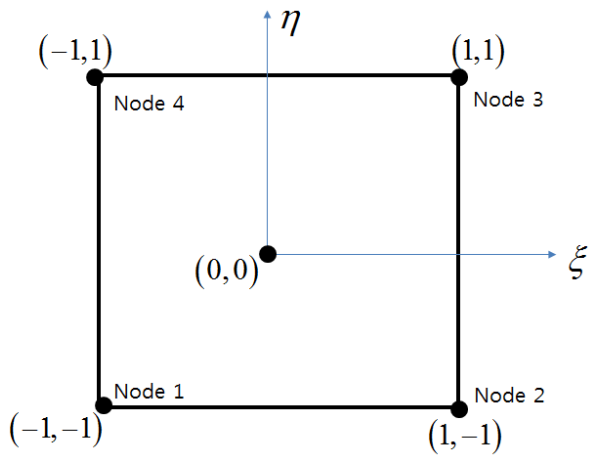

Figure 2.7. Four node square element in natural coordinate for C0 ANCF element isoperimetric formulation.

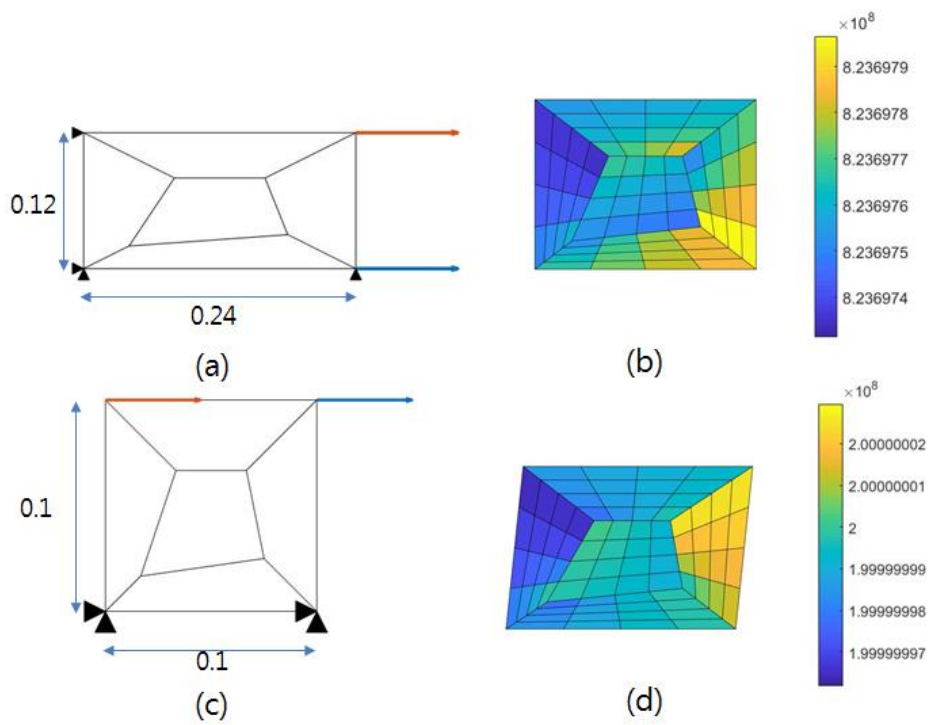

Figure 2.8. (a) Example model for patch test and (b) deformed shape and stress distribution of uniaxial tensile test, and (c) model and (d) results for simple shear test.

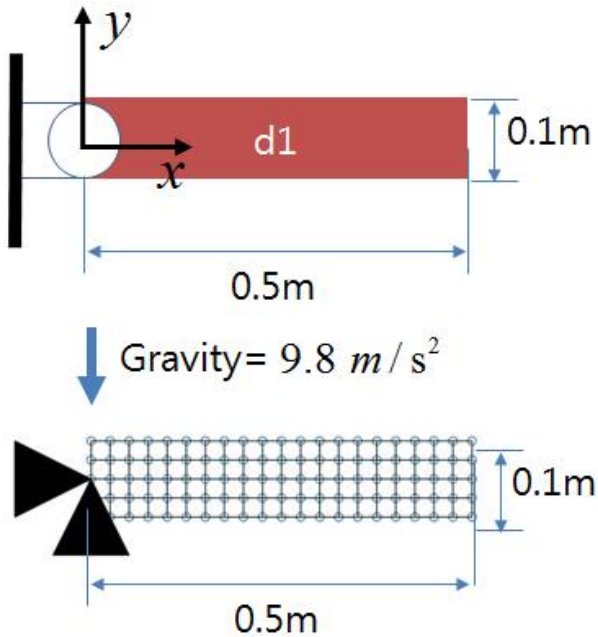

Figure 2.9. Free falling pendulum single-body numerical example problem

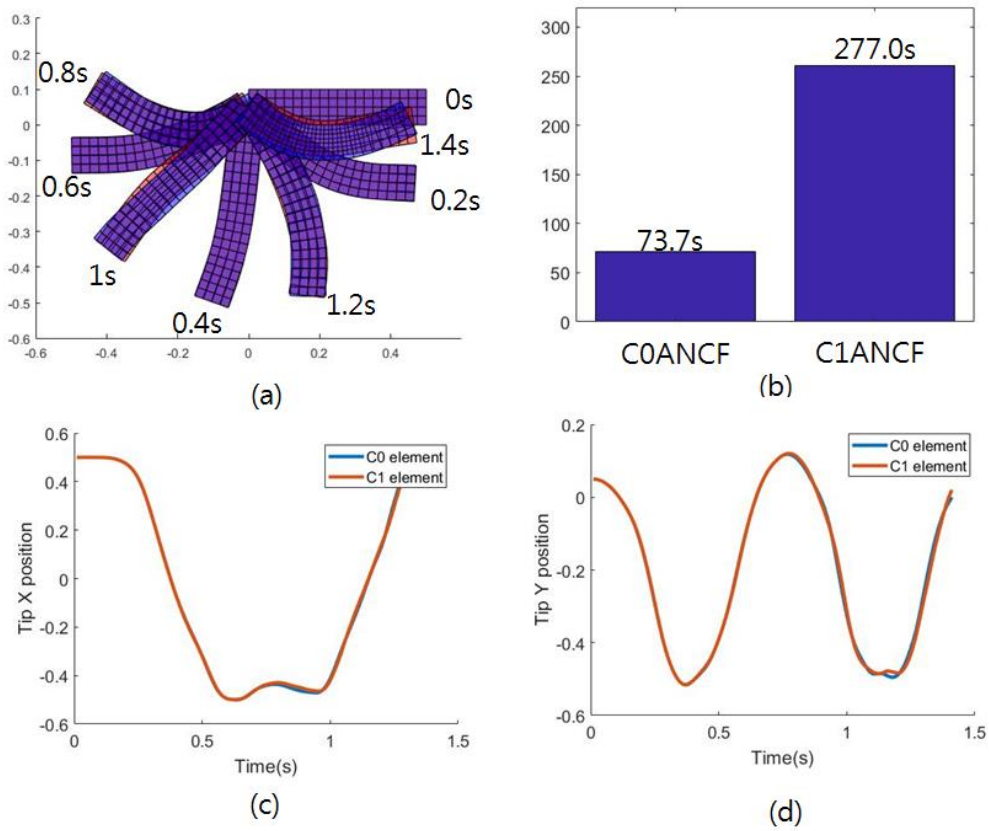

Figure 2.10. Simulation results of single-body (a) deformation snap-shot, (b) computation time comparison, absolute tip position of (c) x-direction and (d) y-direction

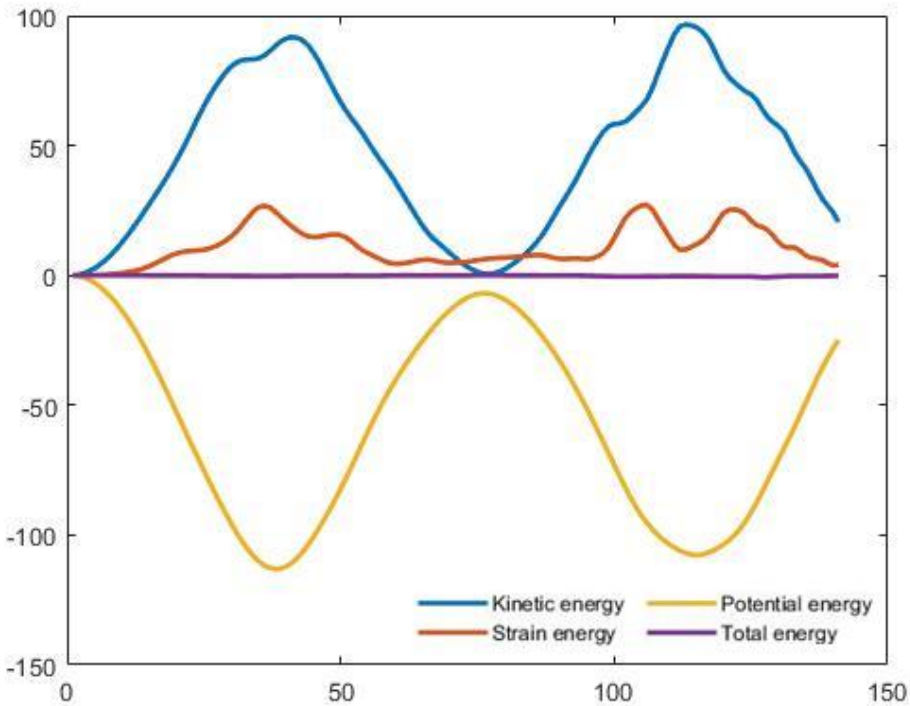

Figure 2.11. Energy balance for the free falling pendulum single body

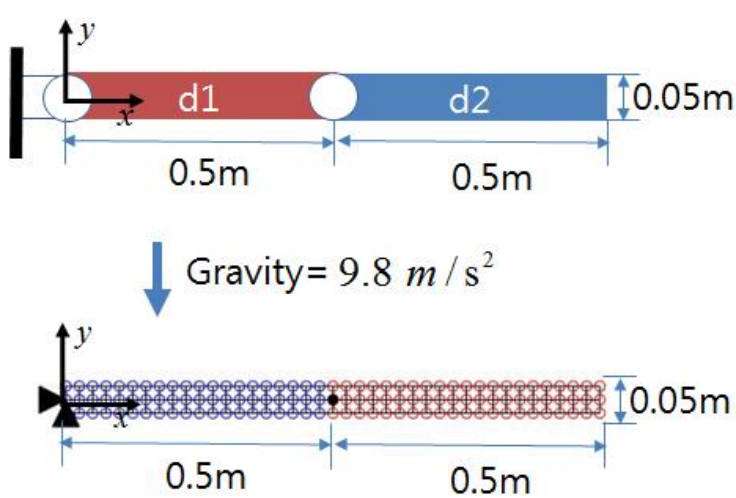

Figure 2.12. Free falling multi-body numerical example problem

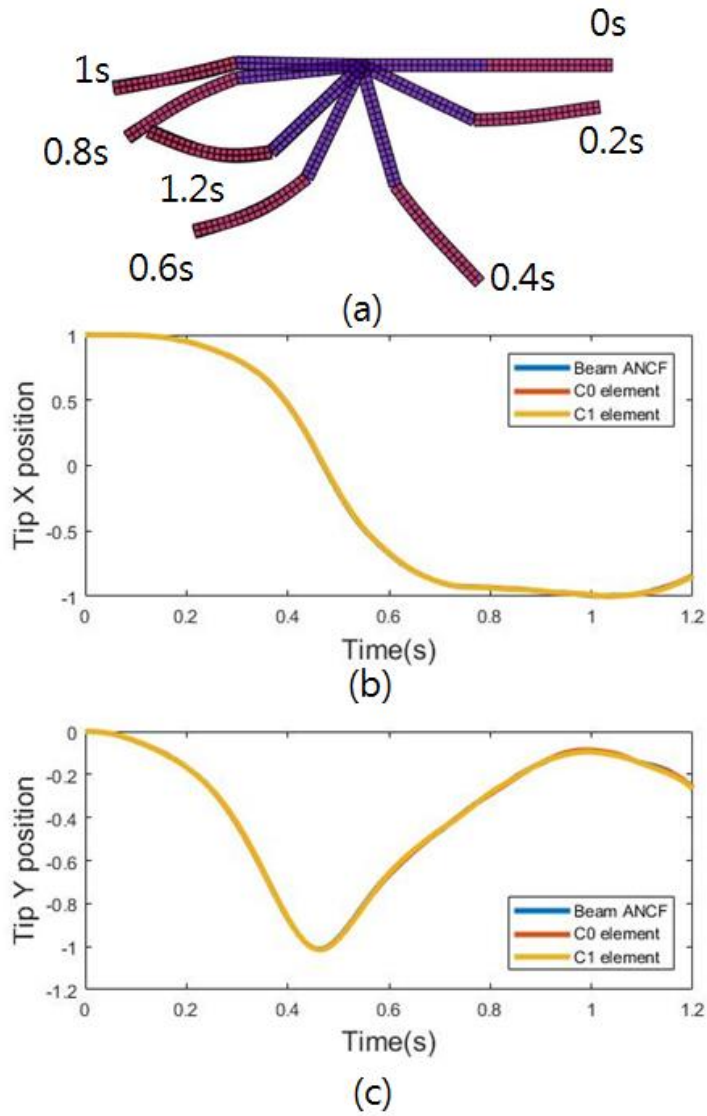

Figure 2.13. . Simulation results of multi-body pendulum (a) deformation snap-shot, absolute tip position of (b) x-direction and (c) y-direction

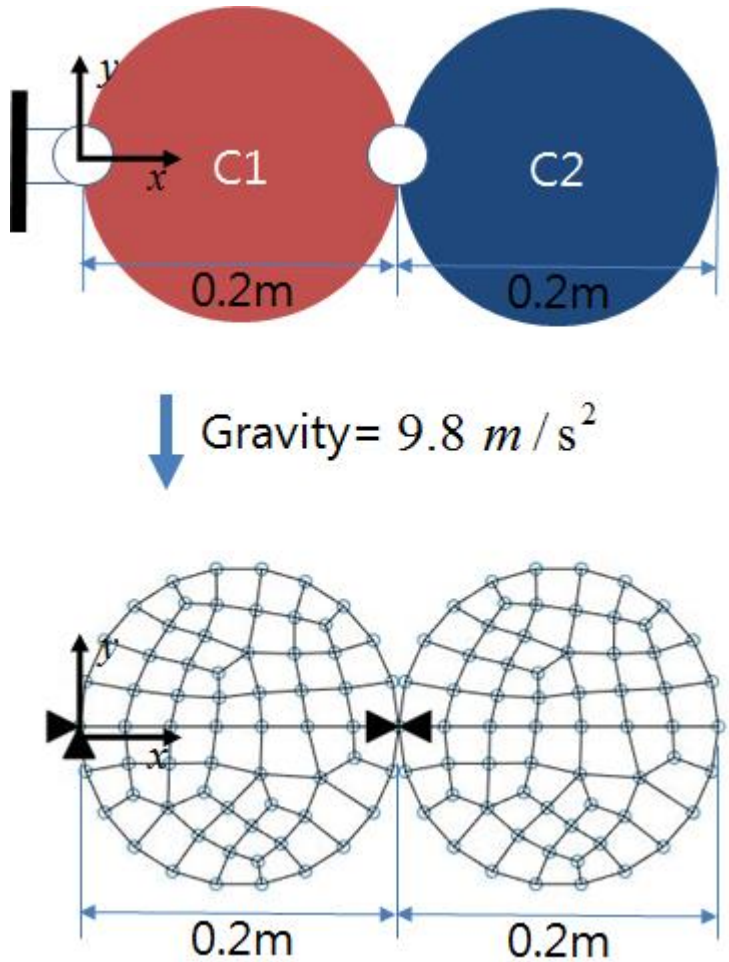

Figure 2.14. Numerical example problem for non-rectangular mesh configuration, multi-body circle structure.

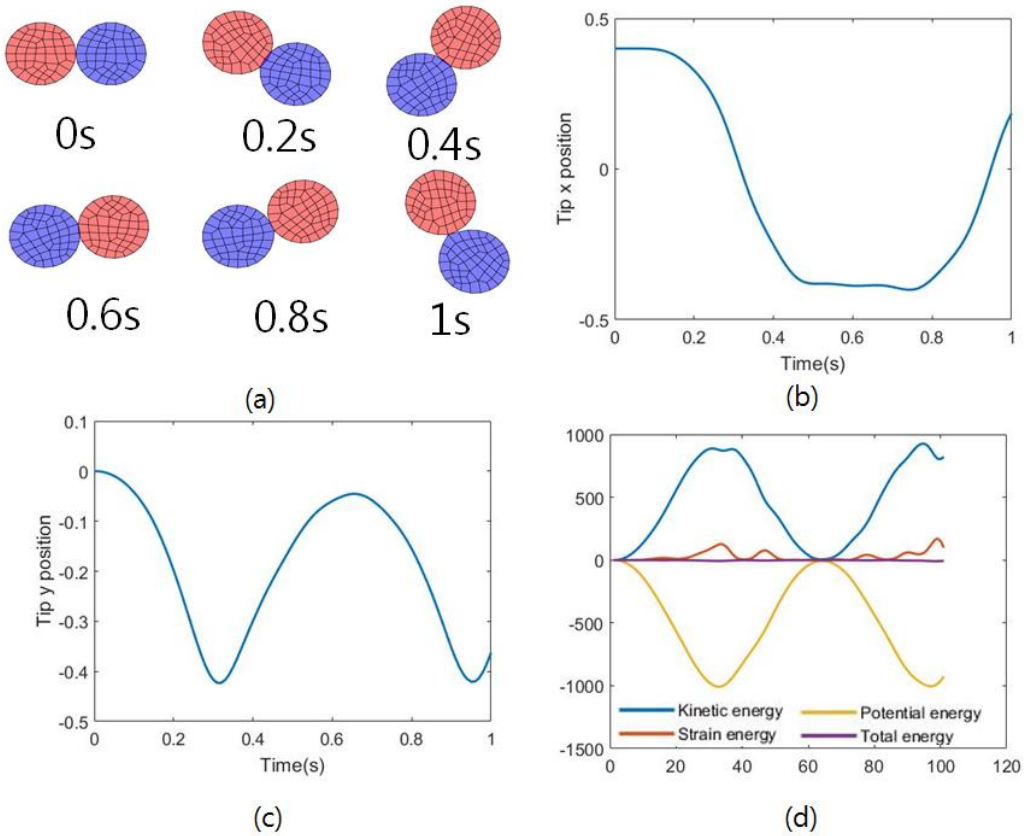

Figure 2.15. . Simulation results of multi-body circle (a) deformation snap-shot, absolute tip position of (b) x-direction ,(c) y-direction and (d) energy balance.

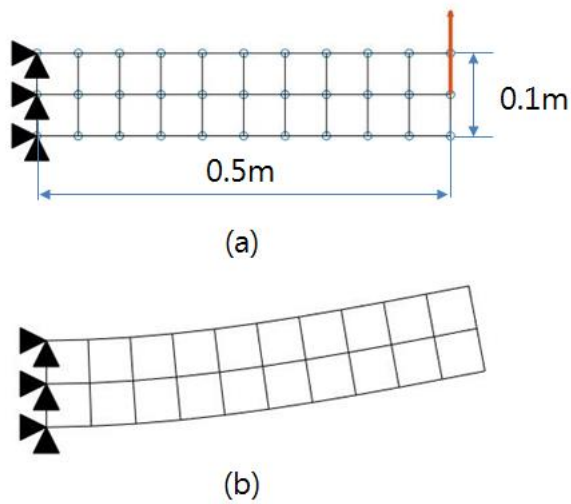

Figure 2.16. (a) model for vibration simulation and (b) initial state of vibration simulation deformed by initial force.

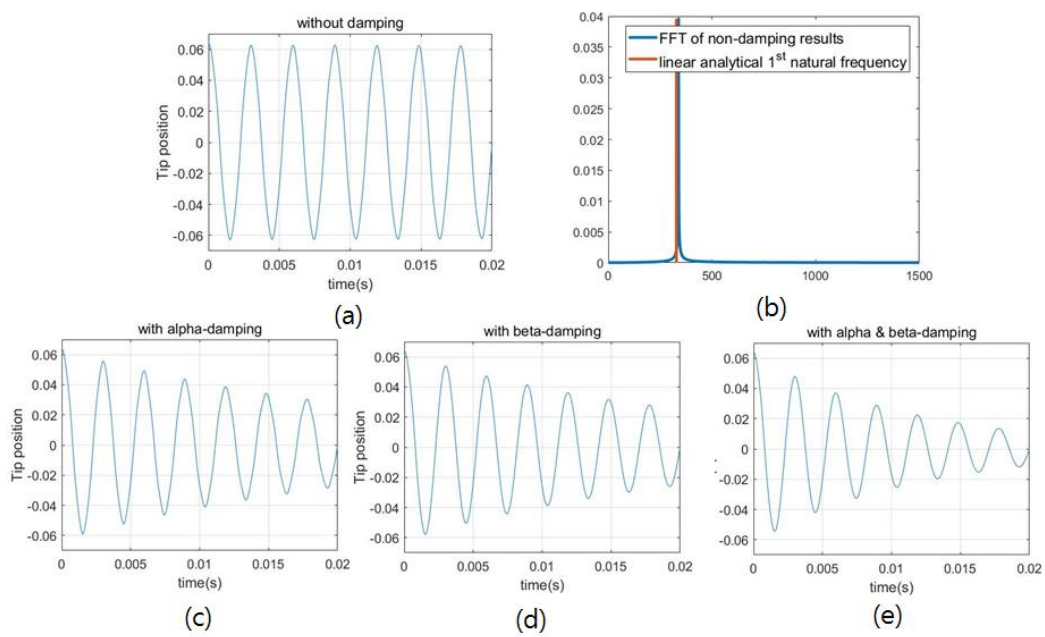

Figure 2.17. Tip position change of 2D plane vibration example (a) without damping (b) and its FFT results, (c) with alpha damping, (d) with beta damping and (e) with alpha and beta damping.

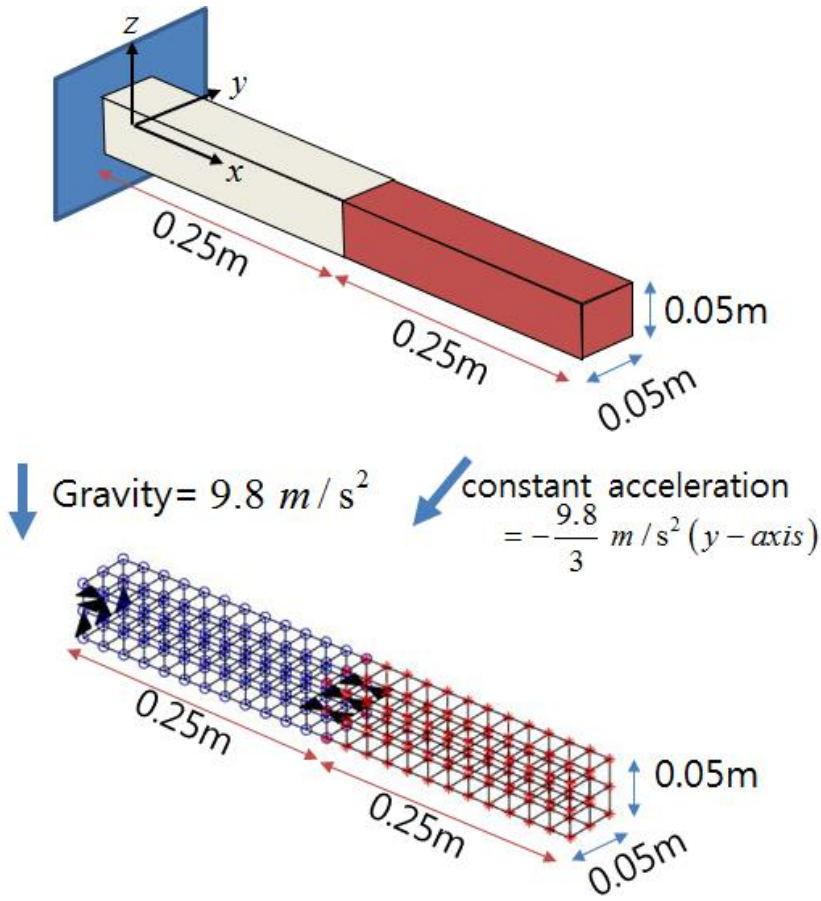

Figure 2.18. 3-dimensional dynamic numerical example problem for ANCF simulation(multi-body connected pendulum with regular mesh)

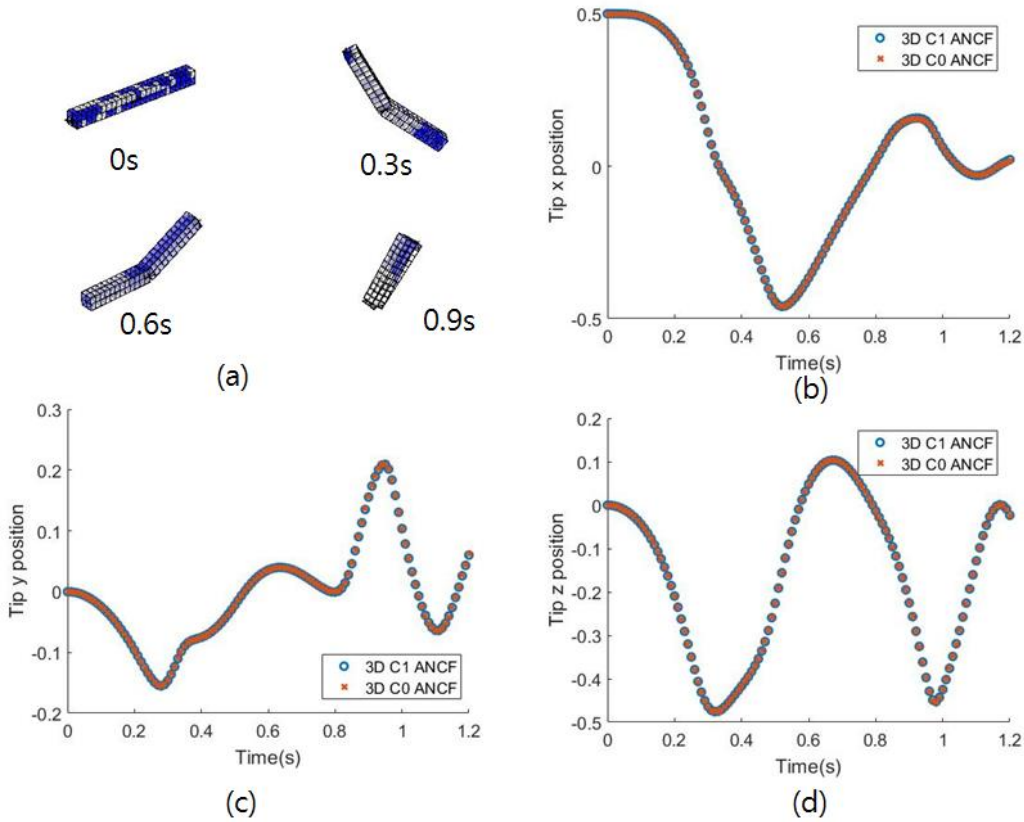

Figure 2.19. . Simulation results of 3D multi-body pendulum (a) deformation snap-shot, absolute tip position of (b) x-direction ,(c) y-direction and (d) z-direction.

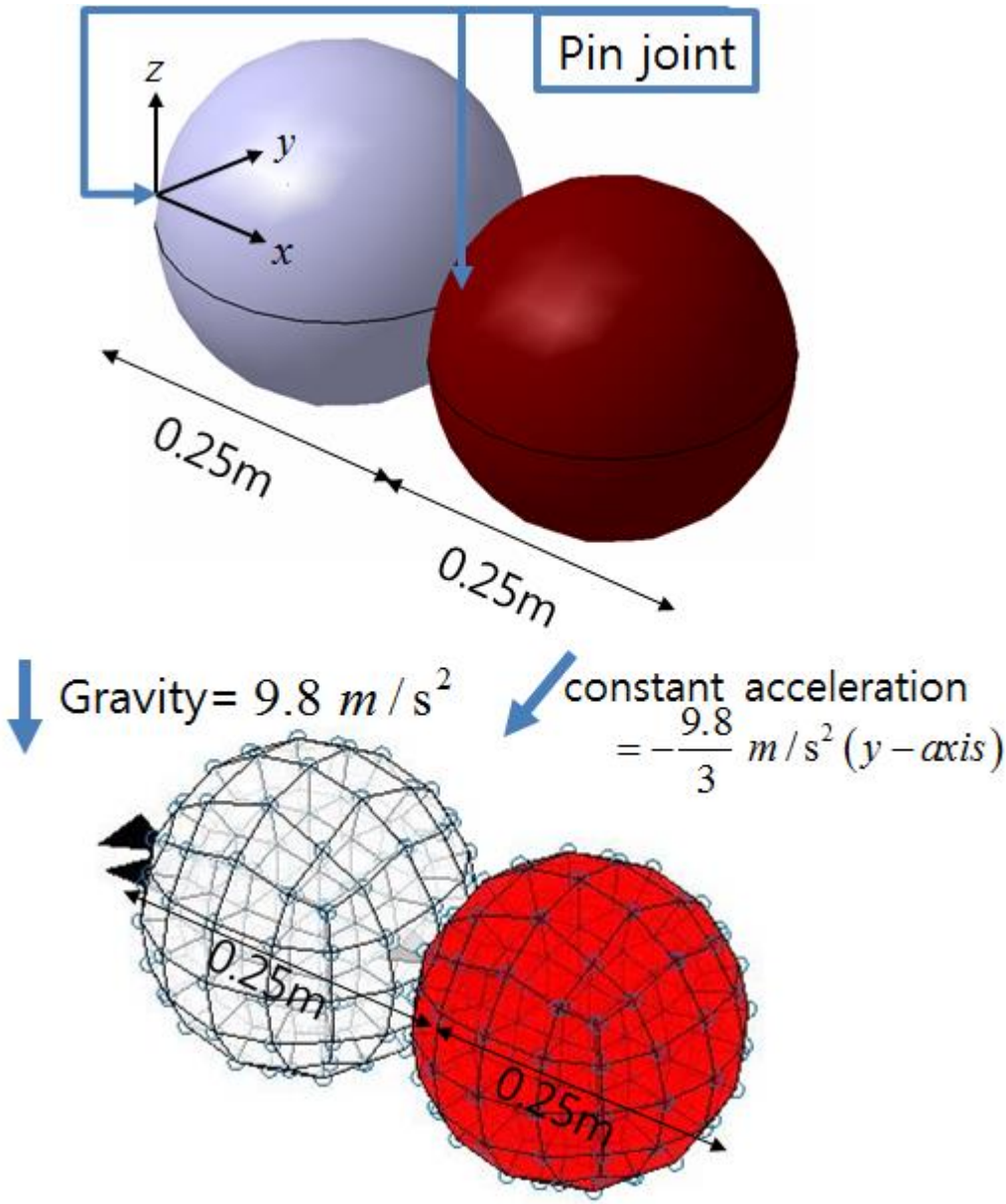

Figure 2.20. 3-dimensional dynamic numerical example problem for ANCF simulation(multi-body connected sphere with non-regular mesh)

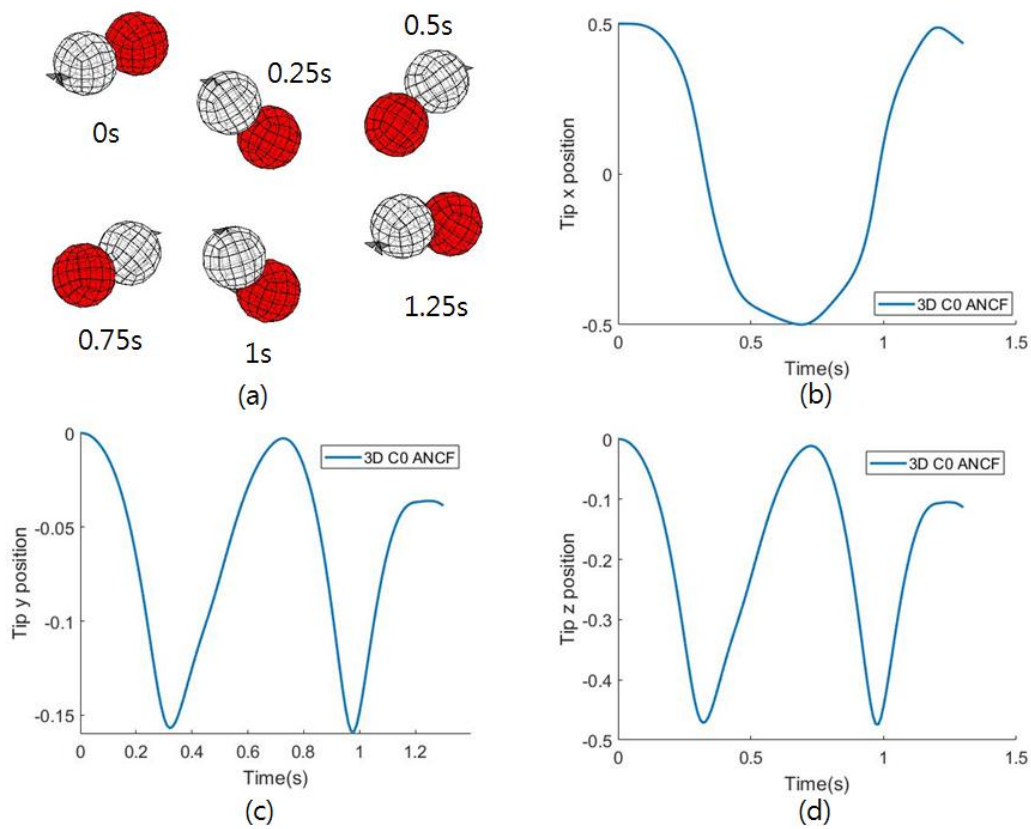

Figure 2.21. Simulation results of 3-dimensional sphere multi-body (a) deformation snap-shot, absolute tip position of (b) x-direction, (c) y-direction and (d) z-direction

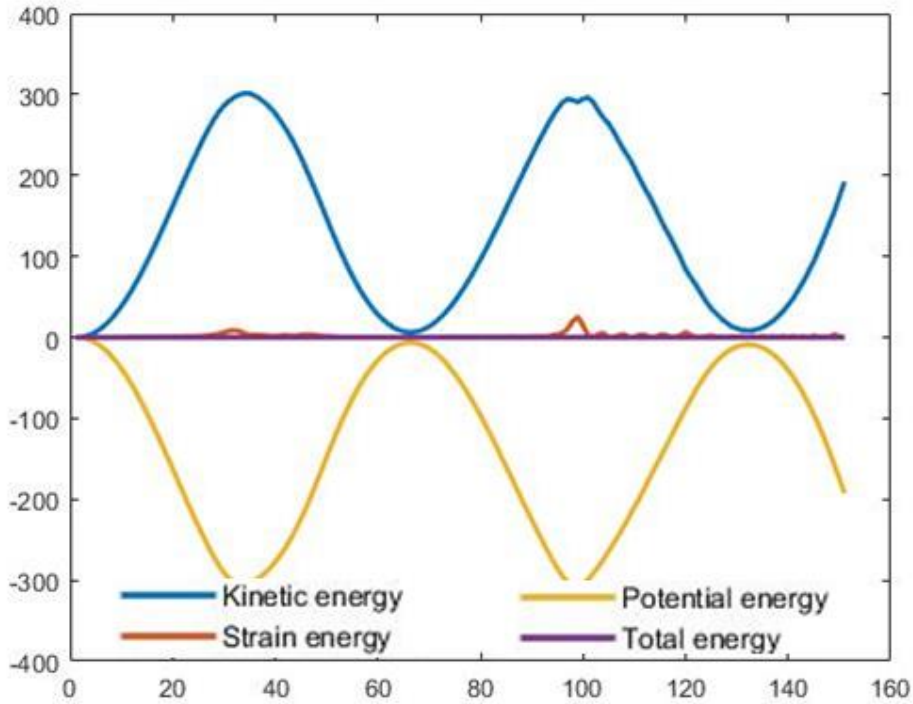

Figure 2.22. Energy balance for the of three-dimensional sphere multi-body

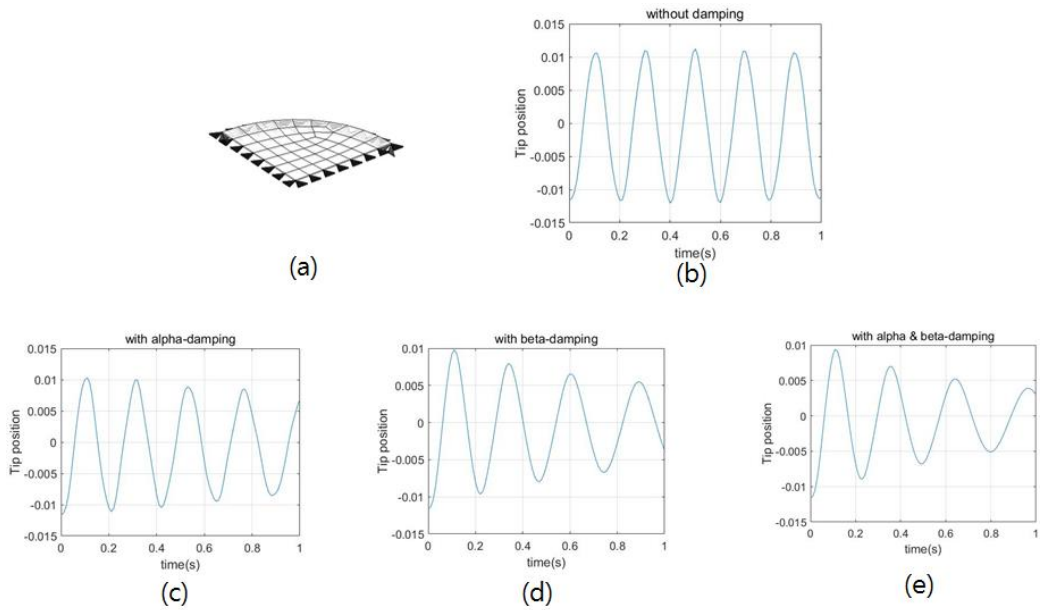

Figure 2.23. (a) 3D vibration example model, and change of the absolute position of center point of disc (a) without damping, (b) with alpha damping, (c) with beta damping, and (e) with alpha and beta damping.

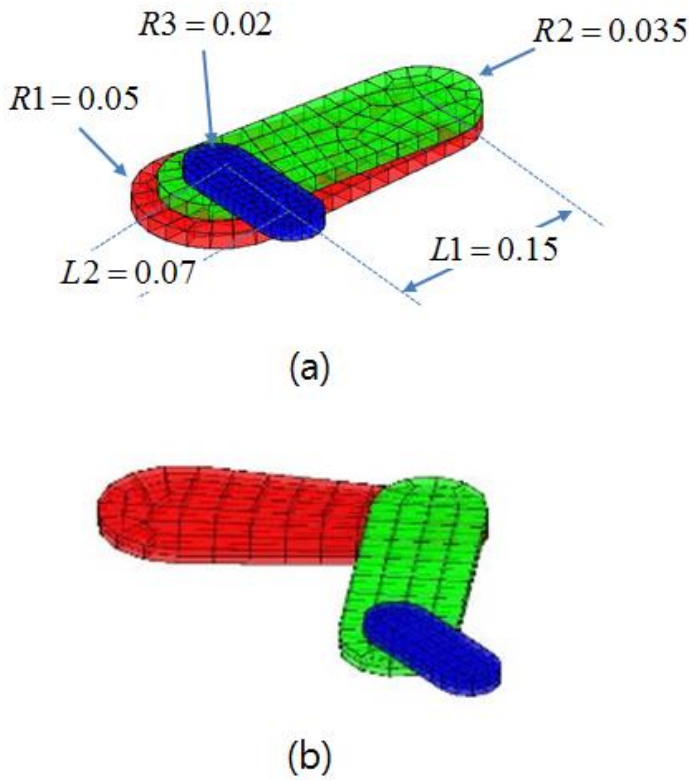

Figure 2.24. (a) Simplified wafer transfer robot for practical 3-dimensional motion and vibration example and (b) its deformed shape at T=0.45s

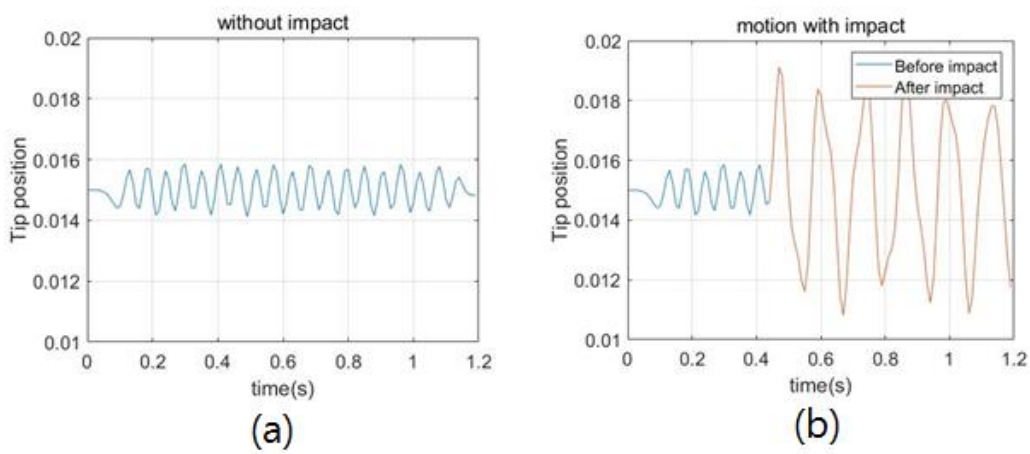

Figure 2.25. The absolute position change of WTR tip (a) without Wafer lift(impact) and (b) with wafer lift(impact) at T=0.45

Table 2.1. Two-dimensional free falling pendulum properties and simulation coefficients used in single-body simulation

Mass density (kg/m^2)	Modulus of elasticity(N/m^2)	Poission's Ratio	Length(m)	Height(m)	Thickness(m)
7800	40e4	0.3	0.5	0.1	1

Rayleigh damping coefficient		Newmark's coefficient		Total time	Time step
α_D	β_D	γ	β		
0	0	0.5	0.25	1.4	0.01

Table 2.2. Two-dimensional free falling pendulum properties and simulation coefficients used in multi-body simulation

	Mass density (kg/m^2)	Modulus of elasticity(N/m^2)	Poission's Ratio	Length (m)	Height (m)	Thickness (m)
A	2702.8	5e5	0.3	0.5	0.05	0.1
B	2181.7	5e4	0.3	0.5	0.05	0.1

Rayleigh damping coefficient		Newmark's coefficient		Total time	Time step
α_D	β_D	γ	β		
0	0	0.5	0.25	1.2	0.01

Table 2.3. Two-dimensional free falling multi-body circle properties and simulation coefficients used in simulation

	Mass density (kg/m^2)	Modulus of elasticity(N/m^2)	Poission's Ratio	Radius (m)	Thickness (m)
A	7800	5e6	0.3	0.5	1
B	7800	1e6	0.3	0.5	1

Rayleigh damping coefficient		Newmark's coefficient		Total time	Time step
α_D	β_D	γ	β		
0	0	0.5	0.25	1	0.01

Table 2.4. Three-dimensional free falling pendulum properties and simulation coefficients used in multi-body simulation

	Mass density (kg/m^2)	Modulus of elasticity(N/m^2)	Poission's Ratio	Length (m)	Height (m)	Thickness (m)
A	7800	1e9	0.3	0.25	0.05	0.05
B	7800	1e8	0.3	0.25	0.05	0.05

Rayleigh damping coefficient		Newmark's coefficient		Total time	Time step
α_D	β_D	γ	β		
0	0	0.5	0.25	1.2	0.01

Table 2.5 Three-dimensional free falling sphere properties and simulation coefficients used in multi-body simulation

	Mass density (kg/m^2)	Modulus of elasticity(N/m^2)	Poission's Ratio	Radius (m)	Thickness (m)
A	2702.8	5e5	0.3	0.5	0.1
B	2181.7	5e4	0.3	0.5	0.1

Rayleigh damping coefficient		Newmark's coefficient		Total time	Time step
α_D	β_D	γ	β		
0	0	0.5	0.25	1.2	0.01

3. C0 ANCF plane-beam and solid-shell element

In this chapter, the formulation process of ANCF plane-beam and solid-shell elements are described. First, the existing ANCF beam, plate and shell element are discussed. Since the formulation process of beam elements, plate and shell elements include some assumption; there are models that are not suitable for the application. Since thickness cannot be described in these formulations, these cannot apply to the model which of thickness is an important factor of structure deformation.

There are several ways to solve the thickness problem. The first is a formulation that explicitly calculates the thickness. Thickness is a new degree of freedom, so there is a problem coupling with existing elements that do not consider thickness as a degree of freedom. Secondly, a method of solving a beam using a two-dimensional element and a shell using a three-dimensional element is proposed. This formulation method can formulate without special assumption, and its application range is very wide. However, if the length ratio of the element is very large, the performance drops and the locking phenomenon occurs. The elements that can solve such locking phenomena and provide the same performance as beams, plates and shell elements without special assumptions are called plane-beam or solid-shell elements.

In this chapter, ANCF C0 plane-beam element and ANCF C0 solid-shell element formulation by applying enhanced assumed strain, which is most suitable for C0 ANCF element, are proposed. Numerical example results for each proposed element are conducted.

3.1. Basic information of ANCF beam, plate and shell

- **ANCF beam**

Shabana et al proposed a one-dimensional ANCF beam element to analyzing two-dimension space deformation of the beam with the absolute and its derivatives in global coordinate as degrees of freedom. The ANCF beam element thus has four degrees of freedom per node, and the element degree of freedom is given as

$$\mathbf{e}=\begin{bmatrix} r_1|_{x=0} & r_2|_{x=0} & \left.\frac{\partial r_1}{\partial x}\right|_{x=0} & \left.\frac{\partial r_1}{\partial y}\right|_{x=0} & \cdots \\ r_1|_{x=l} & r_1|_{x=l} & \left.\frac{\partial r_1}{\partial x}\right|_{x=l} & \left.\frac{\partial r_1}{\partial x}\right|_{x=l} \end{bmatrix} \tag{3.1}$$

The shape function is given by the third order polynomial order as

$$\begin{aligned} &s_1=1-3\xi^2+2\xi^3,\ \ s_2=\xi-2\xi^2+\xi^3, \\ &s_3=3\xi^2-2\xi^3\ \ ,\ \ s_4=\xi^3-\xi^2 \end{aligned} \tag{3.2}$$

, where ξ is x/l, and l is length of element. By using the position derivative in ANCF instead of the rotation used in the conventional beam element, the shape as shown in **Figure 3.1** can be represented by a small number of elements. The degree of freedom used in the figure is: $\mathbf{e}=\begin{bmatrix}-1 & 1 & 2 & -3 & 1.4 & 1.4 & 3 & 2\end{bmatrix}^T$.

Kinetic energy can be expressed as **Equation 2.19** as 2D plane or 3D solid element. The internal energy is divided by longitudinal energy and transverse energy as

$$U=U_l+U_t=\frac{1}{2}\int_0^l\left[EA\varepsilon_l^2+EI\kappa^2\right]dx \tag{3.3}$$

, where U_l is longitudinal energy, U_t transverse energy, A is area, ε_l is longitudinal strain, I is second moment of area and κ is curvature.

- **ANCF plate and shell element**

The degree of freedom per node of the ANCF plate or shell element is the same as that of the ANCF solid element in **section 2.1**. It has twelve degrees of freedom per node, and the four node plate or shell -element has forty-eight degrees of freedom per element. The Shape function is very similar to the C1 ANCF plane element. The degrees of freedom and corresponding shape functions of absolute position, x derivative, and y derivative, which are included in the C1 ANCF plane element, can be used directly in the shape function of the plate and shell elements. The full shape function can be obtained by adding a shape function of z-direction derivative degrees of freedom as

$$
\begin{aligned}
&S_{1,1} = -(1-\xi)(1-\eta)\left(2\xi^2+2\eta^2-\xi-\eta-1\right), \quad S_{1,2} = l\xi(1-\xi)^2(1-\eta)\\
&S_{1,3} = w\eta(1-\xi)(1-\eta)^2, \quad S_{1,4} = t(\xi-1)(\eta-1)\zeta\\
&S_{2,1} = -\xi(1-\eta)\left(2\xi^2+2\eta^2-3\xi-\eta\right), \quad S_{2,2} = -l\xi^2(1-\xi)(1-\eta)\\
&S_{2,3} = w\xi\eta(1-\eta)^2, \quad S_{2,4} = -t\xi(\eta-1)\zeta\\
&S_{3,1} = -\xi\eta\left(2\xi^2+2\eta^2-3\xi-3\eta+1\right), \quad S_{3,2} = -l\xi^2\eta(1-\xi)\\
&S_{3,3} = -w\xi\eta^2(1-\eta), \quad S_{3,4} = t\xi\eta\zeta\\
&S_{4,1} = -\eta(1-\xi)\left(2\xi^2+2\eta^2-\xi-3\eta\right), \quad S_{4,2} = l\xi\eta(1-\xi)^2\\
&S_{4,3} = -w\eta^2(1-\xi)(1-\eta), \quad S_{4,4} = -t(\xi-1)\eta\zeta
\end{aligned}
\tag{3.4}
$$

, where t is thickness plate or shell element.

As with ANCF beam elements, complex element variations can be represented by a small number of elements. For example, Figure 3.2 shows the shape of the element with the following degrees of freedom.

$$\mathbf{e}=\begin{bmatrix} 0 & 0 & 0 & 1 & 0 & -1 & 0 & 1 & 1 & 0 & 1 & -1 \\ 1 & 0 & 0 & 1 & 0 & -1 & 0 & 1 & -1 & 1 & 0 & 1 \\ 1 & 1 & 0 & 1 & 0 & -1 & 0 & -1 & -1 & 0 & 1 & 1 \\ 0 & 1 & 0 & 1 & 0 & -1 & 0 & 1 & 1 & 1 & 0 & -1 \end{bmatrix}^T$$

Since the process of formulating kinetic energy and internal energy is consistent with the process derived from the 3D ANCF element, it is not described in this section.

3.2. Enhanced assumed strain (EAS) formulation with ANCF

The internal energy for the enhanced assumed strain (EAS) method application is the Hu-Washizu principle as

$$U=\int\left[\frac{1}{2}\boldsymbol{\varepsilon}_h^T\mathbf{E}\boldsymbol{\varepsilon}_h-\boldsymbol{\sigma}_h^T\boldsymbol{\varepsilon}_h+\boldsymbol{\sigma}_h^T\boldsymbol{\varepsilon}_h^{(\mathbf{e})}\right]dV \tag{3.5}$$

, where $\boldsymbol{\varepsilon}_h$ and $\boldsymbol{\sigma}_h$ is approximated strain and stress from EAS formulation and $\varepsilon_h^{(e)}$ is strain vector from ordinary ANCF formulation which is corresponding to **Equation 2.27** in **section 2.1**. The approximated strain can be expressed as the sum of the ANCF compatible strain and the enhanced strain as

$$\boldsymbol{\varepsilon}_h=\boldsymbol{\varepsilon}_h^{(e)}+\tilde{\boldsymbol{\varepsilon}}_h \tag{3.6}$$

, where $\tilde{\boldsymbol{\varepsilon}}_h$ is an extra strain field. $\boldsymbol{\varepsilon}_h$ becomes the enhanced assumed strain field by enhancing compatible strain field, $\boldsymbol{\varepsilon}_h^{(e)}$, by extra strain field, $\tilde{\boldsymbol{\varepsilon}}_h$. Applying this enhanced assumed strain to **Equation 3.4**, the equation becomes as

$$\begin{aligned} U_e&=\int\left[\frac{1}{2}\left(\boldsymbol{\varepsilon}_h^{(e)}+\tilde{\boldsymbol{\varepsilon}}_h\right)^T\mathbf{E}\left(\boldsymbol{\varepsilon}_h^{(e)}+\tilde{\boldsymbol{\varepsilon}}_h\right)-\boldsymbol{\sigma}_h^T\left(\boldsymbol{\varepsilon}_h^{(e)}+\tilde{\boldsymbol{\varepsilon}}_h\right)+\boldsymbol{\sigma}_h^T\boldsymbol{\varepsilon}_h^{(\mathbf{e})}\right]dV \\ &=\int\left[\frac{1}{2}\left(\boldsymbol{\varepsilon}_h^{(e)}+\tilde{\boldsymbol{\varepsilon}}_h\right)^T\mathbf{E}\left(\boldsymbol{\varepsilon}_h^{(e)}+\tilde{\boldsymbol{\varepsilon}}_h\right)-\boldsymbol{\sigma}_h^T\left(\tilde{\boldsymbol{\varepsilon}}_h\right)\right]dV \end{aligned} \tag{3.7}$$

, where U_e is internal energy with enhanced assumed strain. If the strain field and the stress are determined as a vector perpendicular to each other, the final term of the internal energy becomes zero, so that **Equation 3.7** can be simply expressed as

$$U_e = \int \left[\frac{1}{2} \left(\boldsymbol{\varepsilon}_h^{(e)} + \tilde{\boldsymbol{\varepsilon}}_h \right)^T \mathbf{E} \left(\boldsymbol{\varepsilon}_h^{(e)} + \tilde{\boldsymbol{\varepsilon}}_h \right) \right] dV \tag{3.8}$$

The variables explicitly calculated in Equation 3.8 are the compatible strain, which is calculated from the absolute position as Equation 2.27, and extra strain. If the internal strain parameters, $\boldsymbol{\alpha}$, are taken into account for the additional degrees of freedom of each element, the extra strain field can be expressed as

$$\tilde{\boldsymbol{\varepsilon}}_h = \mathbf{M}\boldsymbol{\alpha} \tag{3.9}$$

, where $\mathbf{M}$ is interpolation matrix for the extra strain fields. **Equation 3.9** is substituted into **Equation 3.8** and summarized as

$$U_e = \frac{1}{2} \int \left[\left(\boldsymbol{\varepsilon}_h^{(e)} \right)^T \mathbf{E} \left(\boldsymbol{\varepsilon}_h^{(e)} \right) + \left(\boldsymbol{\varepsilon}_h^{(e)} \right)^T \mathbf{E}\mathbf{M}\boldsymbol{\alpha} + \left(\mathbf{M}\boldsymbol{\alpha} \right)^T \mathbf{E} \left(\boldsymbol{\varepsilon}_h^{(e)} \right) + \left(\mathbf{M}\boldsymbol{\alpha} \right)^T \mathbf{E} \left(\mathbf{M}\boldsymbol{\alpha} \right) \right] dV \tag{3.10}$$

From the variation principle, the system equation consisting of unknown parameters absolute position and internal strain parameter alpha can be obtained as

$$\frac{\partial U_e}{\partial \boldsymbol{\alpha}} = \int_V \left[\mathbf{M}^T \mathbf{E} \boldsymbol{\varepsilon}_h^{(e)} + \mathbf{M}^T \mathbf{E}\mathbf{M}\boldsymbol{\alpha} \right] dV = \mathbf{0} \tag{3.11a}$$

$$\frac{\partial U_e}{\partial \mathbf{e}} = \int_V \left[\frac{\partial \left(\boldsymbol{\varepsilon}_h^{(e)} \right)^T}{\partial \mathbf{e}} \mathbf{E} \left(\left(\boldsymbol{\varepsilon}_h^{(e)} \right) + \mathbf{M}\boldsymbol{\alpha} \right) \right] dV = \mathbf{Q}_i \tag{3.11b}$$

For return mapping analysis to solve the geometric nonlinear problem, calculating the

tangent stiffness and deriving the relationship between external force and internal force are required. Equation 3.11 can be modified as

$$\begin{bmatrix} \mathbf{D} & \mathbf{L} \\ \mathbf{L}^T & \mathbf{K}^t \end{bmatrix} \begin{bmatrix} \Delta\boldsymbol{\alpha} \\ \Delta\mathbf{e} \end{bmatrix} = \begin{bmatrix} \mathbf{0} \\ \mathbf{Q}_e - \mathbf{Q}_i \end{bmatrix} \tag{3.12}$$

, where $\mathbf{D}$ and $\mathbf{L}$ is

$$\mathbf{D} = \frac{\partial^2 U_e}{\partial\boldsymbol{\alpha}\partial\boldsymbol{\alpha}} = \int_V \left[\mathbf{M}^T\mathbf{E}\mathbf{M}\right] dV \tag{3.13a}$$

$$\mathbf{L} = \frac{\partial^2 U_e}{\partial\boldsymbol{\alpha}\partial\mathbf{e}} = \int_V \left[\mathbf{M}^T\mathbf{E}\frac{\partial\boldsymbol{\varepsilon}_h^{(e)}}{\partial\mathbf{e}}\right] dV \tag{3.13b}$$

,and $\mathbf{K}^t$ is tangent stiffness matrix which can be calculated as derivative of internal force

$$\frac{\partial\mathbf{Q}_i}{\partial\mathbf{e}} = \frac{\partial^2 U_e}{\partial\mathbf{e}\partial\mathbf{e}} = \frac{\partial\left[\int_V \left[\frac{\partial\left(\boldsymbol{\varepsilon}_h^{(e)}\right)^T}{\partial\mathbf{e}}\mathbf{E}\left(\left(\boldsymbol{\varepsilon}_h^{(e)}\right)+\mathbf{M}\boldsymbol{\alpha}\right)\right] dV\right]}{\partial\mathbf{e}} \tag{3.13c}$$

To apply this enhanced assumed strain formulation to the equation of motion, **Equation 3.12** should be represented only by the function of absolute position. Therefore, by summarizing **Equation 3.12**, it can be expressed as

$$\begin{aligned} \Delta\boldsymbol{\alpha} &= -\mathbf{D}^{-1}\mathbf{L}\Delta\mathbf{e} \\ \left[\mathbf{K}^t - \mathbf{L}^T\mathbf{D}^{-1}\mathbf{L}\right]\Delta\mathbf{e} &= \mathbf{Q}_e - \mathbf{Q}_i \end{aligned} \tag{3.14}$$

The static nonlinear response of the structure can be simulated through the relationship between the external force and the internal force and the incremental of absolute position.

To observe the dynamic response, **Equation 3.14** is substituted into **Equation 2.46**. Then, it can be expressed by enhanced assumed strain parameters as

$$\mathbf{M}\ddot{\mathbf{e}}_{T+\Delta T} + \mathbf{C}\left(\mathbf{e}_T\right)\dot{\mathbf{e}}_{T+\Delta T} + \left[\mathbf{K}^t - \mathbf{L}^T\mathbf{D}^{-1}\mathbf{L}\right]\Delta\mathbf{e} = \mathbf{Q}_e - \mathbf{Q}_i \tag{3.15}$$

By utilizing the Newmark's-beta time integration mentioned in chapter 2, and the modified equation of motion, time response of the structure according to the time can be obtained, when the enhanced assumed strain formulation is applied to the C0 ANCF element.

3.2.1. C0 plane-beam ANCF element

- **C0 plane-beam ANCF element**

In order to apply the EAS formulation to the ANCF element, it is important to determine how many extra strain modes to be used and how to determine the interpolation matrix, respectively. As known in the reference, a maximum of extra strain modes is eleven in a plane element, and three interpolation matrices can be considered.[63] In fact, more extra modes can be added, but this can not achieve meaningful results when more than eleven modes, so reference define eleven is maximum. The interpolation matrix is expressed in the natural coordinate system as

$$\mathbf{M}_\xi = \begin{bmatrix} \xi & & & & \xi\eta & & & 3\xi^2-1 & & & \\ & \eta & & & & \xi\eta & & & 3\eta^2-1 & & \\ & & \xi & \eta & & & \xi\eta & & & 3\xi^2-1 & 3\eta^2-1 \\ 1 & 2 & 3 & 4 & 5 & 6 & 7 & 8 & 9 & 10 & 11 \end{bmatrix} \tag{3.16}$$

In Equation 3.16, three EAS plane formulations can be defined depending on whether four, seven or eleven modes are used. It is known that the locking effect is solved in a rectangular mesh with only four modes. However, performance on a distorted mesh is poor. The stiffness matrix in the rectangular mesh almost coincides in the four modes and in the seven

modes. However, in the distorted mesh, the behavior of bending of four modes elements is not represented well than seven modes, so locking occurs in four modes. The seven modes solve locking not only in rectangular mesh but also in distorted mesh because the bilinear term in interpolation matrix added in the four modes improves bending performance. when eleven modes are used, the actual strain order is increased, but because the distorted mesh or bending performance is not improved, the seven modes are the most optimal formulation.

To use Equation 3.16 defined in the Natural coordinate in global coordinates, Jacobian of the distorted mesh must be considered. By considering Jacobian, the interpolation matrix of the natural coordinate can be transformed into the interpolation matrix of the global coordinate as

$$\mathbf{M} = \frac{\det(\mathbf{J}_0)}{\mathbf{J}} \mathbf{T}_0^{-T} \mathbf{M}_\xi \tag{3.17}$$

, $\mathbf{J}_0$ is Jacobian matrix at origin ($\mathbf{J}\big|_{\xi=0,\eta=0}$) and $\mathbf{T}_0$ is transformation matrix which can be calculated from $\mathbf{J}_0$ as

$$\mathbf{T}_0 = \begin{bmatrix} (J_{11})^2 & (J_{21})^2 & 2J_{11}J_{21} \\ (J_{12})^2 & (J_{22})^2 & 2J_{12}J_{22} \\ J_{11}J_{12} & J_{21}J_{22} & J_{11}J_{22} + J_{12}J_{21} \end{bmatrix}_{\xi=0,\eta=0} \tag{3.18}$$

The nonlinear static response and the dynamic time response of the C0 ANCF 2D plane element with the EAS formulation can be obtained by applying the interpolation matrix obtained from **Equation 3.17, 18,** and the Jacobian matrix to **Equation from 3.11 to 15**. And C0 ANCF element with EAS formulation is called as EAS- C0 ANCF element.

- **Numerical example – Statics**

The results of several static examples are compared to show the response of the proposed EAS-C0 ANCF element to shear locking and volumetric locking. First, how the shear locking phenomenon improved is observed. The shear locking is a locking phenomenon caused by the fact that when a 2D plane element or a 3D solid element is deformed by bending, the number of elements in the thickness direction is insufficient, or when the element order is low, the element cannot describe bending. This phenomenon is usually solved by using many elements in the thickness or length direction. However, as the number of elements increases, the computational efficiency decreases, so the EAS formulation is applied to solve this problem.

To verify how shear locking is improved through the EAS formulation, a thick and thin clamped beam model are assumed as **Figure 3.3**. Each thick and thin model has an aspect ratio of one to five and one to twenty, respectively. The tip absolute position of the results of C0 ANCF plane element and EAS-C0 ANCF plane element are observed while increasing the number of elements. **Figure 3.3** shows the number of element per side is two. The Young's modulus used in the simulation is 3e3N/m^2, the Poisson's ratio is 0.3, and the thickness for the plane problem is 0.1m. The concentrated force is applied to the upper and lower ends in different directions so the moment as to be 1 Nm. **Figure 3.4 (a)** shows that the EAS applied element has almost the same value as the converged value even when only one element in the thickness direction is utilized. However, it can be observed that the absolute position does not change sufficiently due to the locking effect when the

number of elements is small in the simulation that EAS formulation is not applied to. In this case, the converged value can be achieved as the element increases, and the error under 10% can be achieved when using eight elements.

In the case of large aspect ratio like one to twenty, as shown in **Figure 3.4 (b)**, the tendency is different from the case when the aspect ratio is small. In the case of EAS formulation applied, when one element is used, about 20% error is observed, but when the number of elements is more than 3, the value almost coincides with the reference solution. However, if the EAS is not applied, the error tends to decrease as the element increases, but the error is about 20% for the eight elements. This is an error similar to when using one EAS-C0 ANCF element. From the above results, it is confirmed that the C0 ANCF element of the EAS formulation can obtain improved results for shear locking.

Secondly, it is examined that the performance improvement of ANCF C0 element through EAS formulation in volumetric locking. The volumetric locking refers to a phenomenon in which the stiffness is overestimated as the constitutive matrix approaches infinity in the plane strain or 3D problem when the material is incompressible, ie, the Poisson's ratio is close to 0.5. Although methods such as the B-bar method for solving this volumetric locking have been proposed, it is not easy to apply this method to ANCF element because ANCF does not use B matrix when defining strain. Therefore, it is appropriate to use the EAS formulation again to solve the volumetric locking of the ANCF element.

An example of how volumetric locking is solved with the EAS formulation is

presented. The thin clamped beam problem with aspect ratio one to five is used again. Eight elements are used, and the change in tip absolute position is shown in **Figure 3.5**, with Poisson's ratio increasing from 0.3 to 0.499. In order to observe how much the absolute position is locked, the tip positions of each Poisson's ratio are divided by the result of Poisson's ratio equal to 0.3 for each element. As can be seen in the figure, in both cases, it can be seen that as the Poisson's ratio increases to 0.4, the tip position is similarly reduced. However, when the Poisson ratio is increased to 0.4 or more, the results of the C0 ANCF element decreases sharply from 0.45 or more. On the other hand, if the Poisson ratio of the ANCF C0 element applied with EAS formulation increases by 0.4 or more and approaches 0.5, the decrease of the tip position does not change much. Therefore, it can be confirmed that volumetric locking of the C0 ANCF element is solved through EAS formulation.

- **Numerical example - Dynamics**

To determine whether the dynamic response of the C0 ANCF plane element with the EAS formulation is better than the C0 ANCF plane element, the free falling pendulum single-body example used in **chapter 2** is applied as is. The time response for 1.4 seconds for different the number of elements is shown in Figure 3.6. **Figures 3.7 (a) and (b)** show the change in tip position when both elements have eight longitudinal elements. As shown in the figure, when the number of elements is equal to eight, the values between 0.7 and 0.8 seconds and the values after 1.1 seconds are slightly different. The C0 ANCF element is expected to be more inaccurate. Therefore, the results obtained by using sixteen C0 ANCF elements in the longitudinal direction and eight EAS-C0 ANCF elements are shown

in **Figure 3.7 (c) and (d)**. As shown in the figure, it is confirmed that EAS-C0 ANCF element result using eight elements and C0 ANCF result using sixteen elements are well matched each other. As a result, by applying the EAS formulation to the C0 ANCF element, it is possible to obtain improved results in not only static analysis but also dynamic time response analysis.

3.2.2. C0 solid-shell ANCF element

The C0 ANCF solid-shell element can be developed by applying the EAS formulation to the C0 ANCF solid element proposed in **Chapter 2**. This makes it possible to apply to large aspect ratio structure that is not suitable to be interpreted by a C0 ANCF solid element. Up to 30 extra strain modes can be used in the solid element. The interpolation matrix can be expressed as

$$\mathbf{M}_\epsilon = \begin{bmatrix} \xi\ \eta\ \zeta\ \xi\eta\ \xi\zeta\ \eta\zeta\ \xi\eta\ \xi\zeta\ \cdots & \text{EAS9} & \text{EAS15} \\ \xi\eta\ \xi\zeta\ \eta\zeta\ \xi\eta\zeta\ \cdots & \text{EAS21} & \text{EAS30} \end{bmatrix} \tag{3.19}$$

In 3D solid element, four kinds (EAS9, EAS15, EAS21, EAS30) of EAS modes are widely used as shown in **Equation 3.19**. Like the EAS4 in plane element, the EAS9 improves the locking effect, but the performance in the distorted mesh is not that good. The EAS15

improves bending behavior compared to the EAS9, but still volumetric locking occurs. The reason for this is that volumetric locking free EAS elements need to include 1 to 3 modes and 16 to 21 modes. These nine modes allow three normal strains to be in the same polynomial fields, so that the sum of normal strains, the volumetric change, is zero and does not generate spurious constraints.[63] Therefore, in the case of EAS21 including all these modes, it becomes volumetric locking free element. For the EAS30, mathematically all the strain components are complete trilinear fields. However, despite the fact that it takes nine more degrees of freedom per element than EAS21, it is not well used because it has little computational gain and only computation effort increases. Therefore, in this research, the EAS21 formulation is applied to the C0 ANCF solid element to realize C0 ANCF solid -shell element.

Equation 3.19 defined in the Natural coordinate can be modified to be used in the global coordinate through **Equation 3.17**. $\mathbf{J}$ is a three-dimensional Jacobian matrix expressed in **Equation 2.56**. The transformation matrix $\mathbf{T}_0$ of the three-dimensional solid element is expressed as

$$\mathbf{T}_0 = \mathbf{T}_0 = \begin{bmatrix} J_{11_0}^2 & J_{21_0}^2 & J_{31_0}^2 & 2J_{11_0}J_{21_0} & 2J_{21_0}J_{31_0} & 2J_{11_0}J_{31_0} \\ J_{12_0}^2 & J_{22_0}^2 & J_{32_0}^2 & 2J_{12_0}J_{22_0} & 2J_{22_0}J_{32_0} & 2J_{12_0}J_{32_0} \\ J_{13_0}^2 & J_{23_0}^2 & J_{33_0}^2 & 2J_{13_0}J_{23_0} & 2J_{23_0}J_{33_0} & 2J_{13_0}J_{33_0} \\ J_{11_0}J_{22_0} & J_{21_0}J_{22_0} & J_{31_0}J_{32_0} & J_{11_0}J_{22_0}+J_{21_0}J_{12_0} & J_{21_0}J_{32_0}+J_{31_0}J_{22_0} & J_{11_0}J_{32_0}+J_{31_0}J_{12_0} \\ J_{12_0}J_{23_0} & J_{22_0}J_{23_0} & J_{32_0}J_{33_0} & J_{12_0}J_{23_0}+J_{22_0}J_{13_0} & J_{22_0}J_{33_0}+J_{32_0}J_{23_0} & J_{12_0}J_{33_0}+J_{32_0}J_{13_0} \\ J_{11_0}J_{23_0} & J_{21_0}J_{23_0} & J_{31_0}J_{33_0} & J_{11_0}J_{23_0}+J_{21_0}J_{13_0} & J_{21_0}J_{33_0}+J_{31_0}J_{23_0} & J_{11_0}J_{33_0}+J_{31_0}J_{13_0} \end{bmatrix} \quad (3.20)$$

The interpolation matrix obtained from **Equation 19 to 20** can be applied to **Equation 3.9 to 3.15** to simulate nonlinear static response and dynamic time response by transforming C0 ANCF solid element to C0 ANCF solid-shell element with EAS formulation.

- **Numerical example - Statics**

To verify the C0 ANCF solid-shell element proposed in this section, a clamped plate problem as shown in **Figure 3.7** is assumed and results of static response of each element are compared. A plate with a length of 100 and a thickness of 1 which is a thickness ratio of 100 to 1 is assumed. In order to observe the nonlinear static response, a deformation greater than the thickness should be observed. Therefore, the physical properties and external forces are determined by the results of ABAQUS nonlinear simulation that deformation achieved is about 2.7. The Young's modulus is 1e4 N/m^2, the Poisson's ratio is 0.3, and the concentrated load acting at the center of the plate is defined as 163.67N.

Figure 3.8 shows the absolute position change of the center according to the increase in the number of elements of C0 ANCF solid and C0 ANCF solid-shell element applied with EAS9 and 21, with sufficient convergence value obtained from ABAQUS as a reference solution. Comparing the results of EAS9 and EAS21, it is confirmed that the bending behavior of EAS9 is improved of EAS21 as mentioned above. However, if the number of element is enough in both EAS formulation, a convergence value can be obtained. When using only C0 ANCF elements without EAS formulation, the convergence rate is very slow as shown in the figure. Therefore, C0 ANCF solid-shell element is more suitable than C0 ANCF element for shell-like 3D structure analysis with large length-to-thickness ratio.

- **Numerical example - Dynamics**

To test the dynamic response of a C0 ANCF solid-shell element, a pendulum

model is introduced, which is often used in the dynamic response test of shell elements. The Young's modulus is 1e5 N/m^2, the material density is 7810 kg/m^2, the Poisson's ratio is 0.3, the length and of the pendulum is 0.3 m, and the thickness is 0.01 m. Simulation is performed for 0.3 seconds, and using 2 x 2, 4 x 4, 8 x 8 EAS 21 formulated C0 ANCF elements. Boundary conditions only apply to one corner point for all translation degree of freedom. **Figure 3.9** shows the deformed shape at time 0.3s and tip position change according to the time of the number of each element. The convergent value is obtained regardless of the number of elements, but the result of 8 x 8 elements is very consistent with the results observed in the existing reference [36-42]. Therefore, it can be seen that the proposed C0 ANCF solid-shell element with EAS21 formulation is suitable for the dynamic response analysis of shell element.

The proposed C0 ANCF solid-shell element is applied to practical examples. An example of this is the deployment system of the solar panel. These systems have hinges between many body-structures and structures, and stresses and strains in the deployment process affect the normal operation of these systems. Therefore, simulation methods for the analysis of stress and strain occurring in the three-dimensional development process and the development process of such a system have been proposed. [51] The proposed C0 ANCF solid-shell element in this research is applied to this system. In the initial state with three solar panels overlapping of **Figure 3.10**, the process of deploying the final state A and final state B of **Figure 3.10** is simulated. A snapshot of each process is shown in **Figure 3.11**. **Figure 3.11 (a) and (b)** are snapshots of the sequential deployment process for the

final states A and B, respectively. **Figure 3.11** (c**)** is a snapshot of the concurrent deployment process for final state B. In this way, the C0 ANCF solid-shell element can be applied to the time response analysis of various shell-like structures as well as the deployment process used in this example.

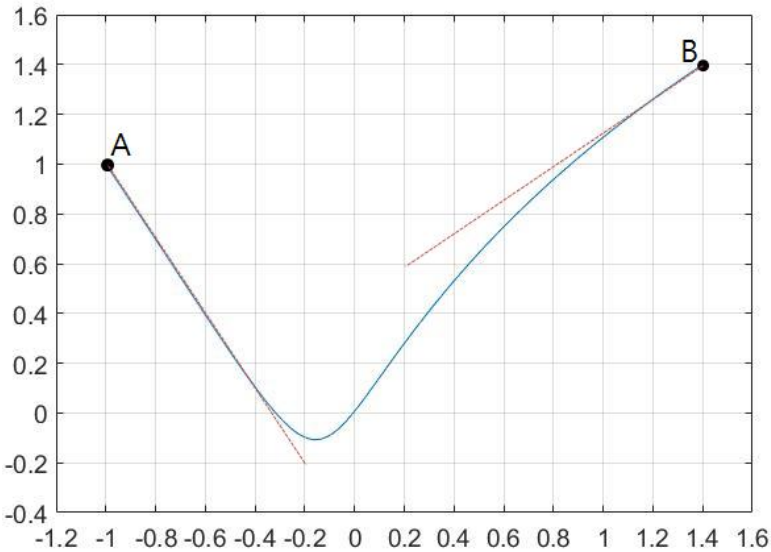

Figure 3.1. Configuration of a ANCF beam element with length : 2 and e=[-1 1 2 -3 1.4 1.4 3 2]^T

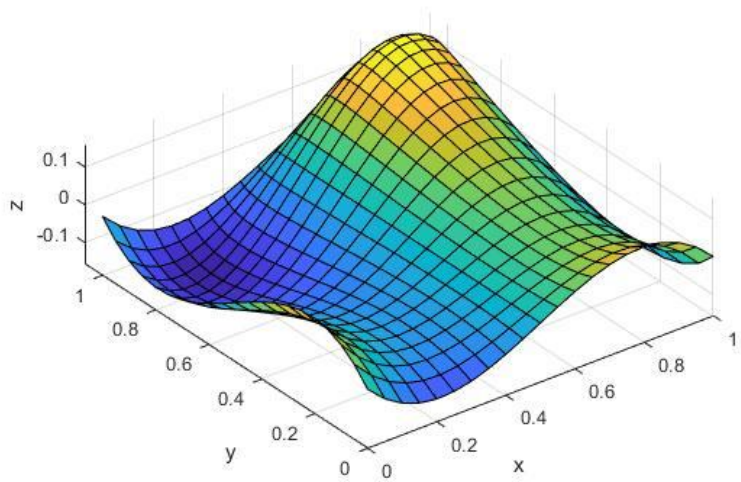

Figure 3.2. Configuration of a ANCF plate element with length : 1, width 1, and e=[-0 0 0 1 0 -1 0 1 1 0 1 -1 1 0 0 1 0 -1 0 1 -1 1 0 1 1 1 0 1 0 -1 0 -1 -1 0 1 1 0 1 0 1 0 -1 0 1 1 1 0 -1]^T

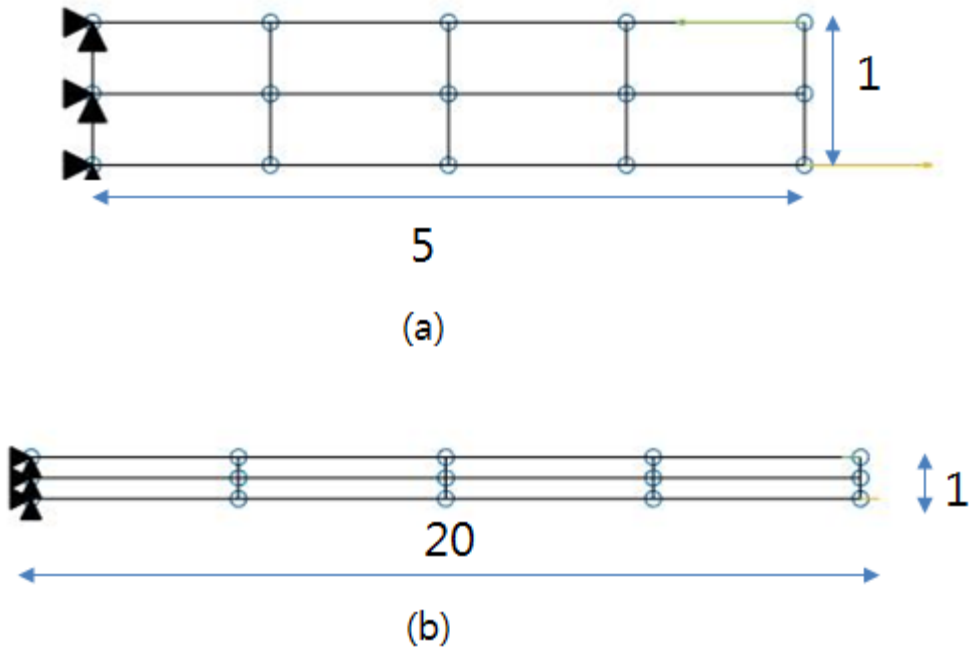

Figure 3.3. example problem for shear locking test with various aspect ratio. (a) five versus one, and (b) twenty versus one.

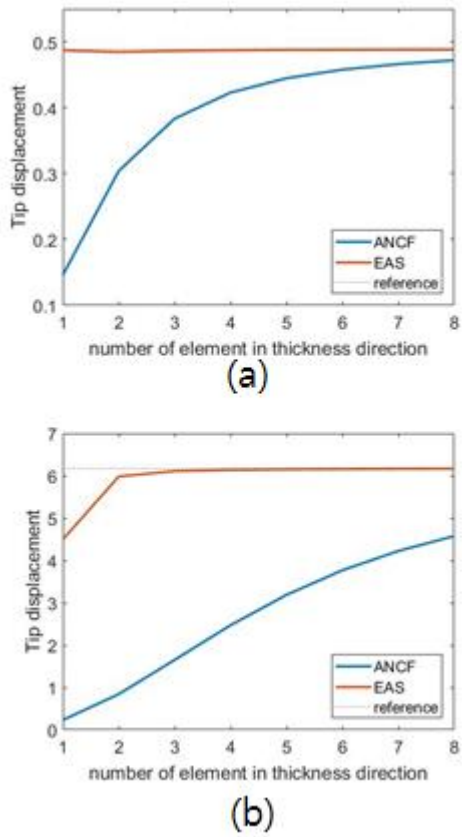

Figure 3.4. The tip position change according to the number of element in thickness direction to observe shear locking, (a) results of rive versus one model, and (b) results of twenty versus one model.

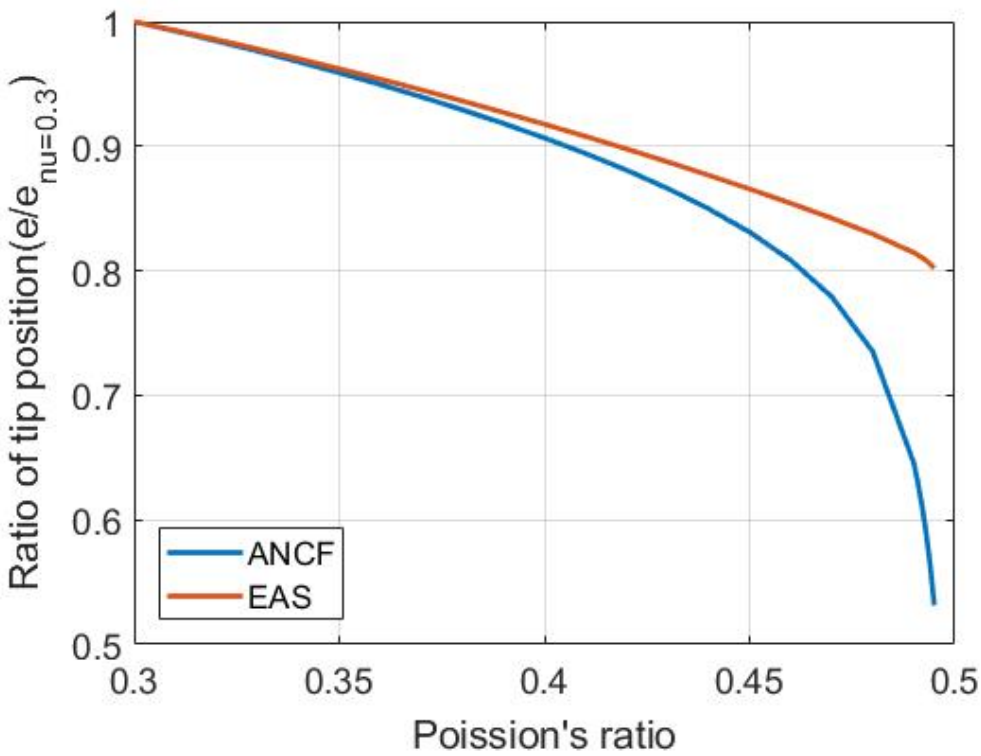

Figure 3.5. The results of volumetric locking test. The ratio of tip position in increasing poisson's ratio.

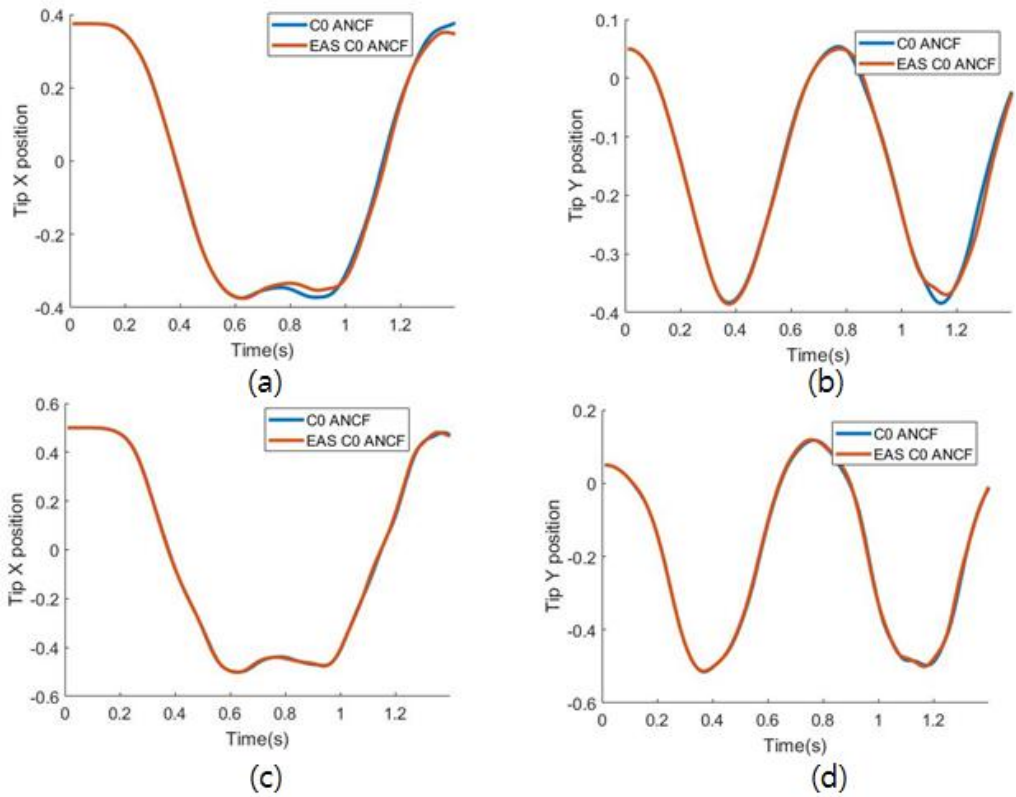

Figure 3.6. Dynamic results of C0 ANCF element and EAS C0 ANCF element. The tip position of (a) X and (b) Y direction with same number of element and the tip position of (c) X and (d) Y with double the number of element in C0 ANCF element.

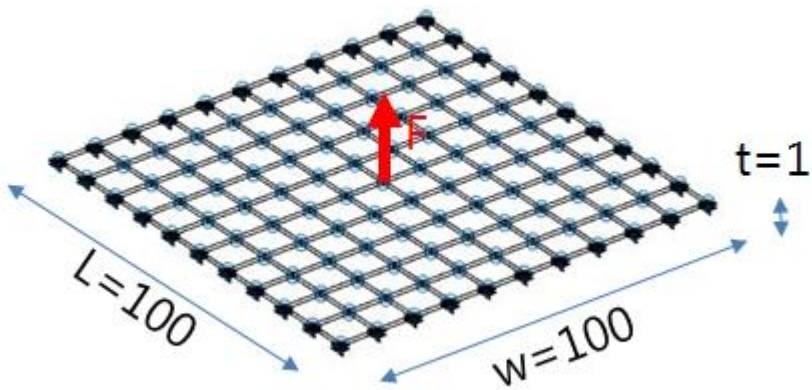

Figure 3.7. The clamped plate for example problem for 3D EAS-C0 ANCF element static test.

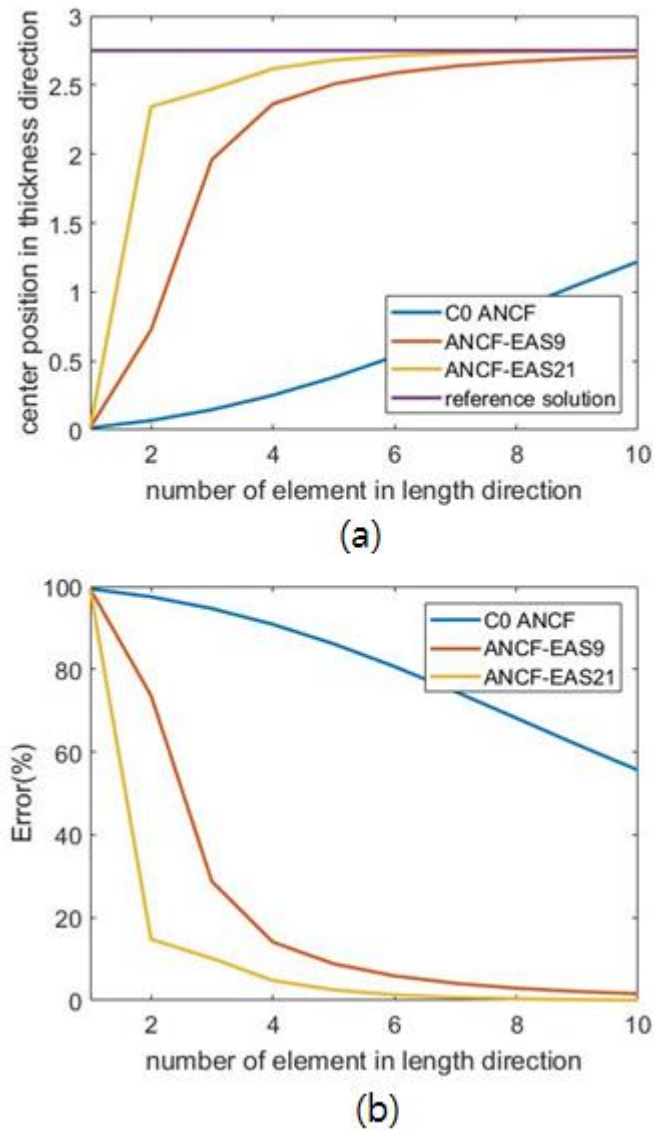

Figure 3.8. (a) The center position in thickness direction and (b) the error according to the number of element in length and width direction in the clamped plate test.

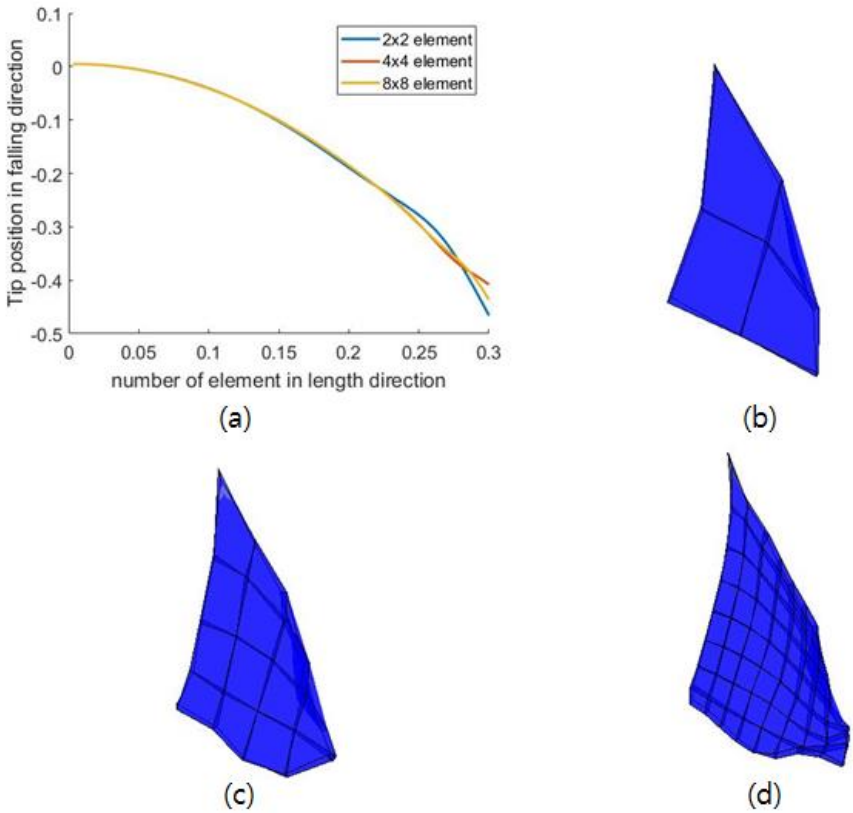

Figure 3.9. (a) The tip position in falling direction according to the number of element and final deformed shape with (b) 2x2 element, (c) 4x4 element, and 8x8 element.

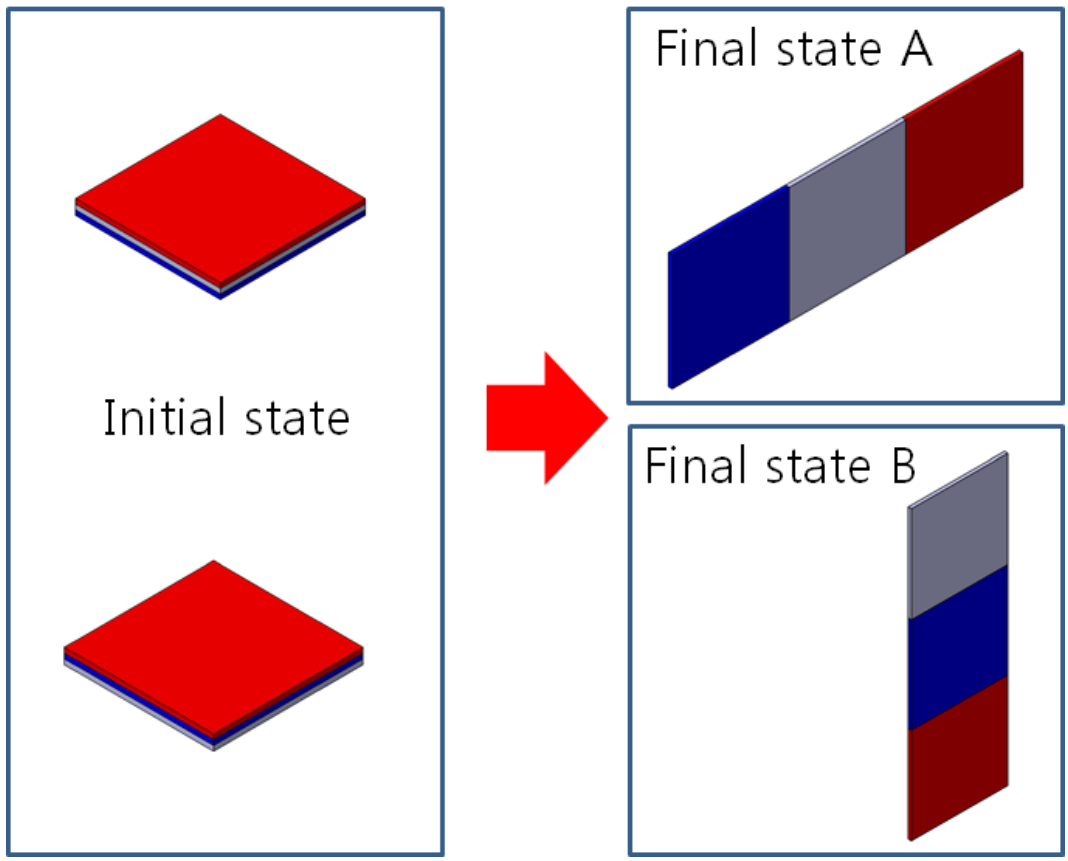

Figure 3.10. the deployment of solar panel. From initial state to two final states.

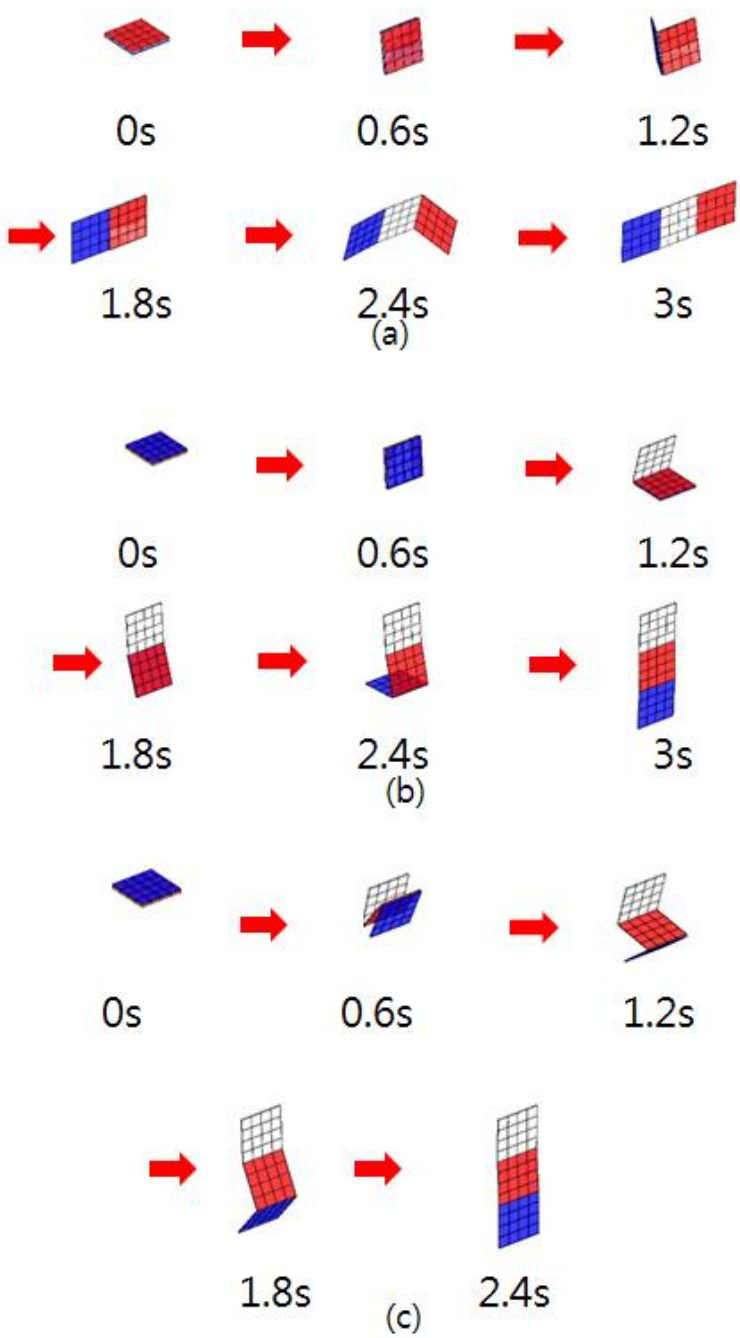

Figure 3.11. the snap shot of deployment process, sequential deployment for (a) final stat A and (b) final state B and (c) simultaneous deployment for final state B.

4. Improvement of C0 ANCF element

In this chapter, two methods to improve the performance of the proposed C0 ANCF element is proposed. The first is the application of incompatible mode. The C0 ANCF element represents the absolute position in the element for each axis as the bilinear function. These low-order elements have limitations as described in chapter 3. Therefore, the limit can be overcome by applying a second or more incompatible mode. It is reported that the accuracy of the simulation is improved by applying incompatible mode to existing displacement based element[78-80]. In **Section 4.1**, this incompatible mode also can be applied to the C0 ANCF element to achieve better performance than the existing C0 ANCF element.

The second improvement is the methods to reduce the calculation time. Various studies have been made to reduce calculation time in finite element analysis.[67-77] In this research, proper orthogonal decomposition (POD) method and element-wise stiffness evaluation procedure (E-STEP) method are focused on. Both methods have a commonality in that they use a snapshot of full analysis results to reduce computation time. These commonalities can be used synergistically to minimize computation time. In section 4.2, The POD method and the E-STEP method are simultaneously applied to the C0 ANCF element to reduce the computation time.

4.1. Incompatible mode

Wilson et al. have developed an incompatible displacement mode to improve the performance of the displacement based finite element analysis. This incompatible model is

applied to the C0 ANCF element [78]. The conventional displacement based element and C0 ANCF are common lower order elements. These elements are inaccurate because they can not express a specific stress gradient. For example, if pure bending is applied to beam structure, the structure should have a curved shape. However, a lower order element does not represent a curved shape as an element. Because the equilibrium for pure bending is satisfied in the parallelogram shape or curved shape, the accuracy of the analysis becomes poor. To solve this problem, Wilson et al. have defined the displacement in the arbitrary point in element by adding a high order term for each element with respect to the displacement as

$$\mathbf{u} = \sum_{i=1}^{4} N_i \mathbf{u}_i + \sum_{i=1}^{2} \mathbf{a}_i P_i \tag{4.1}$$

, where $\mathbf{a}_i$ is displacement amplitudes, and P_i is

$$P_1 = \left(1-\xi^2\right), \quad P_2 = \left(1-\eta^2\right) \tag{4.2}$$

to satisfy zero at the element nodes. Then, the strain term become the function of displacement and displacement amplitudes as

$$\boldsymbol{\varepsilon} = \begin{bmatrix} \varepsilon_{11} \\ \varepsilon_{22} \\ \gamma_{12} \end{bmatrix} = \sum_{i=1}^{4} \mathbf{B}_i \mathbf{u}_i + \sum_{i=1}^{2} \mathbf{G}_i \mathbf{a}_i \tag{4.3}$$

, where $\mathbf{B}$ is calculated from **Equation 2.60** and $\mathbf{G}_i$ is

$$\mathbf{G}_i = \begin{bmatrix} \dfrac{\partial P_i}{\partial x} & \\ & \dfrac{\partial P_i}{\partial y} \\ \dfrac{\partial P_i}{\partial y} & \dfrac{\partial P_i}{\partial x} \end{bmatrix} \tag{4.4}$$

Applying this incompatible displacement model to the C0 ANCF element, Equation 4.1 can be transformed to the function of position instead of displacement as

$$\mathbf{r} = \sum_{i=1}^{4} S_i \mathbf{e}_i + \sum_{i=1}^{2} \boldsymbol{\alpha}_i P_i \tag{4.5}$$

, where $\boldsymbol{\alpha}_i$ is additional position amplitudes. Since P_i values use the same order, **Equation 4.2** can be used as it is. The strain of the C0 ANCF element can be obtained as in **Equation 2.27**, and the derivative of the absolute position is transformed as

$$\begin{aligned} \mathbf{r}_x &= \sum_{i=1}^{4} \frac{\partial S_i}{\partial x} \mathbf{e}_i + \sum_{i=1}^{2} \frac{\partial P_i}{\partial x} \boldsymbol{\alpha}_i \\ \mathbf{r}_y &= \sum_{i=1}^{4} \frac{\partial S_i}{\partial y} \mathbf{e}_i + \sum_{i=1}^{2} \frac{\partial P_i}{\partial y} \boldsymbol{\alpha}_i \end{aligned} \tag{4.6}$$

The process of applying the equation of motion is omitted because it is the same as that of the C0 ANCF element described in **Chapter 2**.

- **Numerical example - Dynamics**

The tapered multi-beam model as shown in **Figure 4.1** is assumed to verify how much the incompatible mode improves the performance of the dynamic response of the C0 ANCF element. The height of the tapered beam is reduced from the initial 0.05m to 0.014m

and the length is 0.15m. The two bodies are assumed to be symmetrical about the connecting point, and the center of the left body is fixed by a pin joint. Both bodies used the same material properties, with a Young's modulus of 1e6 N/m^2, a Poisson's ratio of 0.3, and a density of 7800kg/m^3.

The simulation results are shown in **Figure 4.2** for a one-second time response with a thickness of 0.1m and gravity of 9.8m/s^2. The results of the C0 ANCF element and the C0 ANCF element, considered the incompatible mode, obtained from the 2 x 6 element appear as solid lines in **Figure 4.2**. Both results show some differences after 0.5 seconds. The result of using more elements in the C0 ANCF element is shown in **Figure 4.2** as 'o'. The results of the C0 ANCF element using more elements is very consistent with the result of the element with incompatible mode using fewer elements. As a result, By applying the incompatible mode, the performance of the existing C0 ANCF element can be improved.

4.2. Computational time improvement

The nonlinear dynamic simulation requires Newton-Rapson iteration calculation to calculate nonlinear relation at every time step. In addition, the tangent stiffness due to the nonlinear relation must be obtained for every iteration step. Therefore, as the time step increases, the number of iterations increases so that the dynamic simulation time is greatly increased. Therefore, it is important to reduce computation time to efficiently utilize the C0 ANCF element developed for nonlinear dynamic response analysis. Through this dissertation, a method to reduce computation time by applying the POD method and E-

STEP method to C0 ANCF element is proposed. The results obtained with the small calculation time is compared to the results obtained through full analysis.

The POD method and the ESTEP method are suitable for use together because they have a commonality in that they utilize full analysis snapshot data. Also, even if the full analysis is not possible, two methods can be applied to the dynamic response simulation of the structure based on the absolute position obtained from the experiment. This chapter explains the POD method and the E-STEP method, and the process of applying it to the C0 ANCF element together. Finally, the results of full analysis and the results of each method are compared to verify how much these methods benefit the calculation time.

4.2.1. Proper orthogonal decomposition (POD) reduction method

The POD method utilize Eigen mode vector and Eigen value based on high-order data obtained from experiment or simulation and applies it to reducing of the analysis model. The Eigen modes that have a great influence on the dynamic response of the structure are found and governing equation of structure response is approximated and reduced by low dimensional data values. First, the analysis degree of freedom according to the time obtained from full analysis or experiment can be expressed as **Equation 4.7**

$$\mathbf{E}_{m\times n} = \underbrace{\begin{bmatrix} e_1^{t_1} & e_1^{t_2} & \cdots & e_1^{t_i} & \cdots & e_1^{t_n} \\ e_2^{t_1} & e_2^{t_2} & \cdots & e_2^{t_i} & \cdots & e_2^{t_n} \\ \vdots & \vdots & \ddots & \vdots & \ddots & \vdots \\ e_{m-1}^{t_1} & e_{m-1}^{t_2} & \cdots & e_{m-1}^{t_i} & \cdots & e_{m-1}^{t_n} \\ e_m^{t_1} & e_m^{t_2} & \cdots & e_m^{t_i} & \cdots & e_m^{t_n} \end{bmatrix}}_{m\times n}_{sampling} \tag{4.7}$$

, where $e_j^{t_i}$ is value of j th degree of freedom at a time step t_i. When the total number of degrees of freedom is m and the total time step is n, the snapshot full data can be obtained with the m-by-n matrix as **Equation 4.7**. Through the singular value decomposition of snapshot data, the proper orthogonal mode (POM) ($\underset{m\times m}{\mathbf{\Phi}}$), singular value ($\underset{m\times n}{\mathbf{\Sigma}}$), and time modulation of POMs ($\underset{n\times n}{\mathbf{V}}$) can be obtained. The relationship between the snapshot data and these values is expressed as

$$\mathbf{E}_{m\times n} = \underset{m\times m}{\mathbf{\Phi}}\ \underset{m\times n}{\mathbf{\Sigma}}\ \underset{n\times n}{\mathbf{V}}^T \tag{4.8a}$$

$$\mathbf{\Phi} = \begin{bmatrix} \phi_1 & \phi_2 & \cdots & \phi_m \end{bmatrix} \tag{4.8b}$$

$$diag(\mathbf{\Sigma}) = \begin{bmatrix} \sigma_1 & \sigma_2 & \cdots & \sigma_n \end{bmatrix} \tag{4.8c}$$

, where ϕ_i is each proper orthogonal mode and σ_i is i th singular value that is a energy ratio that how much i th POM influence time response of full system. How many POMs to use for reduction is related to this singular value. It is common to construct the POM so that ratio of full energy and total energy of the reduced modes to be 99.99% or more as

$$\varepsilon = \frac{\sum_{i=1}^{R} \sigma_i}{\sum_{i=1}^{m} \sigma_i} \geq 0.9999 \tag{4.9}$$

Once the number of reduced modes is determined by the energy ratio, a reduced POM can be constructed as

$$\mathbf{\Phi}_R = \begin{bmatrix} \phi_1 & \phi_2 & \cdots & \phi_R \end{bmatrix} \tag{4.10}$$

The degree of freedom of the full analysis can be expressed by the reduced POM($\underset{(m\times R)}{\mathbf{\Phi}_R}$)

and the reduced degree of freedom $\underset{(R\times 1)}{\mathbf{p}}$ as

$$\underset{(m\times 1)}{\mathbf{e}} = \underset{(m\times R)}{\mathbf{\Phi}_R}\,\underset{(R\times 1)}{\mathbf{p}} \tag{4.11}$$

Equation of motion, **Equation 2.46**, can be transformed into a reduced equation of motion by **Equations 9 and 10** as

$$\mathbf{M}_R\ddot{\mathbf{p}} + \mathbf{C}_R\dot{\mathbf{p}} + \mathbf{K}_R^t\Delta\mathbf{p} + \mathbf{Q}_{\text{int}}^R = \mathbf{Q}_{ext}^R \tag{4.12a}$$

, where

$$\begin{aligned} &\mathbf{M}_R = \mathbf{\Phi}^T\mathbf{M}\mathbf{\Phi}, \quad \mathbf{C}_R = \mathbf{\Phi}^T\mathbf{C}\mathbf{\Phi}, \\ &\mathbf{K}_R^t = \mathbf{\Phi}^T\mathbf{K}^t\mathbf{\Phi}, \quad \mathbf{Q}_{\text{int}}^R, \mathbf{Q}_{ext}^R = \mathbf{\Phi}^T\mathbf{Q}_{\text{int}}, \mathbf{\Phi}^T\mathbf{Q}_{ext} \end{aligned} \tag{4.12b}$$

By reducing the equation of motion like **Equation 4.12**, the mass, damping, and tangent stiffness metrics are reduced from m by m to n by n. Since the size of the matrix to be handled is reduced from m by m to n by n, it is expected to benefit from computation time.

4.2.2. Element-wise stiffness evaluation procedure (E-STEP) method

The stiffness evaluation procedure (STEP) starts from the fact that the nonlinear internal force of a structure can be expressed as a polynomial function of degrees of freedom. If the internal force can be expressed as a polynomial function of degrees of freedom, the internal force of each iteration step can be obtained directly through the degrees of freedom of each iteration. In addition, the tangent stiffness matrix can be obtained directly from the derivatives of polynomial bases. The equation of motion,

Equation 2.46, can be expressed as an index form with N total degrees of freedom as

$$M_{ij}\ddot{e}_j + C_{ij}\dot{e}_j + K^t_{ij}\Delta e_j + Q^{\text{int}}_i = Q^{ext}_i \qquad i, j = 1, 2, ..., \text{N} \tag{4.13}$$

And, internal force Q^{int}_i is represented by the polynomial function of e_i,

$$Q^{\text{int}}_i = K^{(1)}_{ij}e_j + K^{(2)}_{ijk}e_j e_k + K^{(3)}_{ijkl}e_j e_k e_l \tag{4.14}$$

, where $K^{(1)}_{ij}$ is linear stiffness coefficient and $K^{(2)}_{ijk}$ and $K^{(3)}_{ijkl}$ are nonlinear stiffness coefficient. In this paper, Q^{int}_i is assumed to be a third order polynomial function of absolute position. For convenience, the third order polynomial function is presented in compact form as

$$Q^{\text{int}}_i = \tilde{K}_{ijkl}\tilde{e}_j\tilde{e}_k\tilde{e}_l = \tilde{K}_{iL}\hat{e}_L, \quad \begin{matrix} i = 1, 2, \cdots, \text{N} \\ j, k, l = 1, 2, \cdots, \text{N+1} \\ L = 1, 2, \cdots, \text{L} \end{matrix} \tag{4.15}$$

Where, $\tilde{e}_i$ and $\hat{e}_L$ is

$$\tilde{\mathbf{e}} = \begin{bmatrix} \tilde{\mathbf{e}} \\ 1 \end{bmatrix}, \quad \hat{e}_L = \hat{e}_j\hat{e}_k\hat{e}_l, \qquad j, k, l = 1, 2, \cdots, \text{N+1} \tag{4.16}$$

respectively. $\tilde{K}_{iL}$ is nonlinear stiffness coefficient matrix, of which size is N by L. Where L is the number of all first, second, and third order polynomial bases that can be made through the element's connectivity information. The tangent stiffness matrix can be expressed through the derivative of the internal force as

$$K^t_{ij} = \frac{\partial Q^{\text{int}}_i}{\partial e_j} = \tilde{K}_{ipqr}\frac{\partial \hat{e}_{pqr}}{\partial e_j} = \tilde{K}_{ipqr}\left(\delta_{jp}\tilde{e}_q\tilde{e}_r + \delta_{jq}\tilde{e}_r\tilde{e}_p + \delta_{jr}\tilde{e}_p\tilde{e}_q\right) \tag{4.17}.$$

, where δ_{ij} is Kronecker delta function as

$$\delta_{ij} = \begin{cases} 1 & when \;\; i = j \\ 0 & when \;\; i \neq j \end{cases} \tag{4.18}$$

The internal force and tangent stiffness can be obtained directly from the nonlinear stiffness coefficient matrix, the polynomial bases vector and the polynomial bases differential matrix at each iteration step through from **Equation 14 to 17**.

In general, since the off-diagonal term of the global stiffness matrix is zero, it is very inefficient to obtain the nonlinear stiffness coefficient for global degree of freedom at once for all degrees of freedom. Therefore, it is effective to obtain the nonlinear stiffness coefficient matrix for each element through the element-wise stiffness evaluation (E-STEP) method and assemble it. In order to obtain the coefficient for each element, a snap-shot for the internal force and the absolute position is required for each element to obtain the coefficient. In the case of absolute position snapshot, it is possible to extract the degree of freedom corresponding to each element in the global absolute position snapshot used in the POD method as shown in **Equation 4.7**. For Internal force snapshot, it needs to save the internal force for each iteration step calculated in full analysis. Since the degrees of freedom per element of the C0 ANCF plane element are eight, the relationship between the internal force to obtain the stiffness coefficient and the absolute position snapshot is given as

$$\underset{8\times n(sampling)}{\begin{bmatrix} f_1^{t_1} & f_1^{t_2} & \cdots & f_1^{t_n} \\ f_2^{t_1} & f_2^{t_2} & \cdots & f_2^{t_n} \\ \vdots & \vdots & \ddots & \vdots \\ f_8^{t_1} & f_8^{t_2} & \cdots & f_8^{t_n} \end{bmatrix}} = \underset{8\times 165}{\begin{bmatrix} \tilde{K}_{11} & \tilde{K}_{12} & \cdots & \tilde{K}_{1s} \\ \tilde{K}_{21} & \tilde{K}_{22} & \cdots & \tilde{K}_{2s} \\ \vdots & \vdots & \ddots & \vdots \\ \tilde{K}_{p1} & \tilde{K}_{p2} & \cdots & \tilde{K}_{ps} \end{bmatrix}} \underset{165\times n(sampling)}{\begin{bmatrix} \hat{e}_1^{t_1} & \hat{e}_1^{t_2} & \cdots & \hat{e}_1^{t_n} \\ \hat{e}_2^{t_1} & \hat{e}_2^{t_2} & \cdots & \hat{e}_2^{t_n} \\ \vdots & \vdots & \ddots & \vdots \\ \hat{e}_s^{t_1} & \hat{e}_s^{t_2} & \cdots & \hat{e}_s^{t_n} \end{bmatrix}} \tag{4.19}$$

, where the number of sampling time is n. 165 is the number of polynomial combinations

that can be represented in eight degrees of freedom. This can be achieved through the formulation of combination with repetition, ${}_n\Pi_k$. In the case of the C0 ANCF plane element, n becomes nine, because there are eight degrees of freedom per element and it has to include 1 to represent a constant term. Because it is used up to the third polynomial, k becomes 3. Therefore, 165 of **Equation 4.19** is obtained as

$$ {}_{8+1}\mathbf{\Pi}_3 = {}_9\mathbf{\Pi}_3 = {}_{9+3-1}\mathbf{C}_3 = {}_{11}\mathbf{C}_3 = \frac{11\cdot 10\cdot 9}{3\cdot 2\cdot 1} = 165 \tag{4.20}. $$

The number of polynomial bases, 165, differs by twenty-times compared to element degree of freedom, eight. However, since the internal force and the tangent stiffness matrix must be calculated for each Gauss point in general method, the stiffness evaluation method can shorten the time. The element-wise stiffness coefficient obtained from **Equation 19** can be assembled for each polynomial bases to obtain the global stiffness coefficient.

By applying the E-STEP method, the internal force vector and the tangent stiffness matrix can be obtained by vector and matrix multiplication without using the Gaussian quadrature, which can greatly shorten the time.

4.2.3. E-STEP and POD mixed formulation

As mentioned earlier, applying the POD method and the E-STEP method together, which utilize the snapshot data, can achieve a synergy effect in shortening the calculation time. The equation of motion of E-STEP method, **Equation 4.13**, is still an equation for N global degrees of freedom. Applying the pod method described in **Section 4.2.1** to

Equation 4.13, it can be transformed into a computation for a reduced degree of freedom R. Applying the reduced POM matrix to **Equation 4.13** through the POD method described in **Section 4.2.1**, the equation is transformed as

$$\begin{aligned} &\phi_{ki}^{R} M_{kl} \phi_{lj}^{R} \ddot{p}_j + \phi_{ki}^{R} C_{kl} \phi_{lj}^{R} \dot{p}_j + \phi_{ki}^{R} K_{kl}^{t} \phi_{lj}^{R} \Delta p_j + \phi_{ki}^{R} Q_k^{\text{int}} = \phi_{ki}^{R} Q_k^{ext} \\ &\qquad k,l = 1,2,....,\text{N}, \qquad i,j = 1,2,....R \\ &\Rightarrow M_{ij}^{R} \ddot{p}_j + C_{ij}^{R} \dot{p}_j + K_{kl}^{Rt} \Delta p_j + Q_k^{R\text{int}} = Q_k^{Rext} \end{aligned} \tag{4.21}$$

, where ϕ_{ij}^{R} is i, jth component of reduced POM matrix $\mathbf{\Phi}_R$. The reduced mass matrix and the damping matrix can be obtained as shown in **Equation 4.12b** in **Section 4.2.1**. Reduce internal force는 The reduce internal force can be obtained directly by obtaining the reduced stiffness coefficient $\tilde{K}_{iL}^{R}$ as

$$Q_i^{R\text{int}} = \phi_{ki}^{R} Q_k^{\text{int}} = \phi_{ki} \tilde{K}_{kpqr} \tilde{e}_p \tilde{e}_q \tilde{e}_r = \tilde{K}_{iL}^{R} \hat{e}_L \tag{4.22}$$

Similarly, the reduce tangent stiffness matrix can be obtained as

$$\begin{aligned} K_{ij}^{Rt} &= \phi_{ki}^{R} K_{kl}^{t} \phi_{lj}^{R} = \phi_{ki}^{R} \frac{\partial Q_k^{\text{int}}}{\partial e_l} \phi_{lj}^{R} = \phi_{ki}^{R} \tilde{K}_{kpqr} \frac{\partial \hat{e}_{pqr}}{\partial e_l} \\ &= \tilde{K}_{ipqr}^{R} \left(\delta_{jp} \tilde{e}_q \tilde{e}_r + \delta_{jq} \tilde{e}_r \tilde{e}_p + \delta_{jr} \tilde{e}_p \tilde{e}_q \right) \phi_{lj}^{R} \\ &= \tilde{K}_{ipqr}^{R} \left(\phi_{lp}^{R} \tilde{e}_q \tilde{e}_r + \phi_{lq}^{R} \tilde{e}_r \tilde{e}_p + \phi_{lq}^{R} \tilde{e}_p \tilde{e}_q \right) \end{aligned} \tag{4.23}$$

The number of rows of the polynomial differential matrix for the stiffness evaluation shown in **Equation 4.17** is equal to the number of total degrees of freedom, but the number of rows of the reduced polynomial differential matrix term for the reduced stiffness evaluation of **Equation 4.23** is equal to the number of reduced POMs. Therefore, by reducing the number of polynomial terms for stiffness evaluation, the time gain can be efficiently obtained. The solution of the full degree of freedom can be obtained through the reduced

degree of freedom obtained this process and reduce POMs as **Equation 4.11**.

4.2.4. Numerical examples

To verify how much the E-STEP method and the E-STEP & POD mixed method reduce the calculation time compared to the full analysis in the C0 ANCF plane element, the simple falling pendulum single body problem is assumed as shown in **Figure 4.3**. The length of the pendulum is 0.5m and the height is 0.05m. As a result of comparing the convergence values according to the elements, it is most efficient to use 20 elements in the longitudinal direction and 2 elements in the height direction. At this time, the total number of degrees of freedom is 126. The middle node at the left end was fixed with a pin joint. The Young's modulus is 1e6N/m^2, the Poisson's ratio is 0.3, and the density is 7800kg/m^3. The thickness was 0.5m and gravity was 9.8m/s^2, and the time response is simulated at 0.01 second intervals for 1 second.

Based on the results obtained by full analysis, snapshot data of absolute position change and internal force snapshot of each element are obtained. To apply the POD method, a singular value corresponding to the energy ratio and the POM are obtained by singular value decomposition of the absolute position snapshot as shown in **Equation 4.8**. One-hundred-one singular values for the example model are obtained as

$$diag(\mathbf{\Sigma}) = \begin{bmatrix} 19.62 & 13.14 & 1.548 & 0.5603 & 0.2729 & \cdots & 8.45 \cdot 10^{-10} \end{bmatrix} \qquad (4.24)$$

Since 0.01 second intervals from 0 second to 1 second is simulated, the one-hundred-one singular values can be obtained because the number of time steps is one-hundred-one.

The sum of these singular values is 35.40, and 20 POMs are used so that the energy ratio **Equation 4.9** meets 99.99% as

$$\varepsilon = \frac{\sum_{i=1}^{20} \sigma_i}{\sum_{i=1}^{101} \sigma_i} = \frac{35.396}{35.399} = 0.9999 \tag{4.25}$$

In this way, a reduced POM matrix of 126-by-20 size for POD simulation can be obtained.

To apply the E-STEP method, an 8-by-165 element-wise stiffness coefficient matrix can be obtained through an absolute position snapshot and an internal force snapshot for each element as **Equation 19**. In addition, the global stiffness coefficient matrix of 126-by-5368 can be obtained through the assembling process. The E-STEP & POD mix simulation is possible by applying **Equations 4.21 to 4.23** through the reduced POM matrix and the global stiffness coefficient matrix obtained the previous process.

Figure 4.4 shows the results obtained by applying the E-STEP method, and the E-STEP and POD mixed method, based on the snapshot obtained from full analysis for 1 second. As shown in **Figure 4.4 (a) and (b)**, the results of the tip absolute position change in x- and y-direction of E-STEP method and E-STEP & POD mixed method are very consistent with the results of the full analysis. In **Figure 4.3 (c)**, the calculation time for each method is shown in the bar graph to compare the computational time. The full analysis takes 29.96 seconds, and the E-STEP method use shorten the calculation time about a quarter of full analysis time. In addition, the ESTEP & POD mixed method can predict the exact time response with half the computation time than the E-STEP method. This result is

about eight times less than full analysis, and it is verified that the synergy effect can be obtained by using E-STEP method and POD method together.

To the next, **Figure 4.5** shows the result of E-STEP and E-STEP & POD simulation for 2 seconds based on snapshot data of 1 second. The full analysis is carried out for 2 seconds, and E-STEP and E-STEP & POD are simulated for 2 seconds using reduced POM and stiffness coefficients based on the results for 1 second. As shown in Figures 4.5a-c, the results in E-STEP and E-STEP & POD simulation for 2 seconds by utilizing 1 second of data show a good agreement for the full analysis about tip position and deformed snapshot. For snapshot, the full analysis is red, E-STEP is green, and E-STEP & POD is blue in **Figure 4.5 (c)**. Because the results are exactly the same, the results are overlaid as gray. For computation time, ESTEP & POD result is obtained with 10 times reduced time of full analysis, which is better than 1 second result. Thus, if enough snapshot data for a specific time response is obtained previously, the time response for a longer time through the E-STEP & POD method can be predicted.

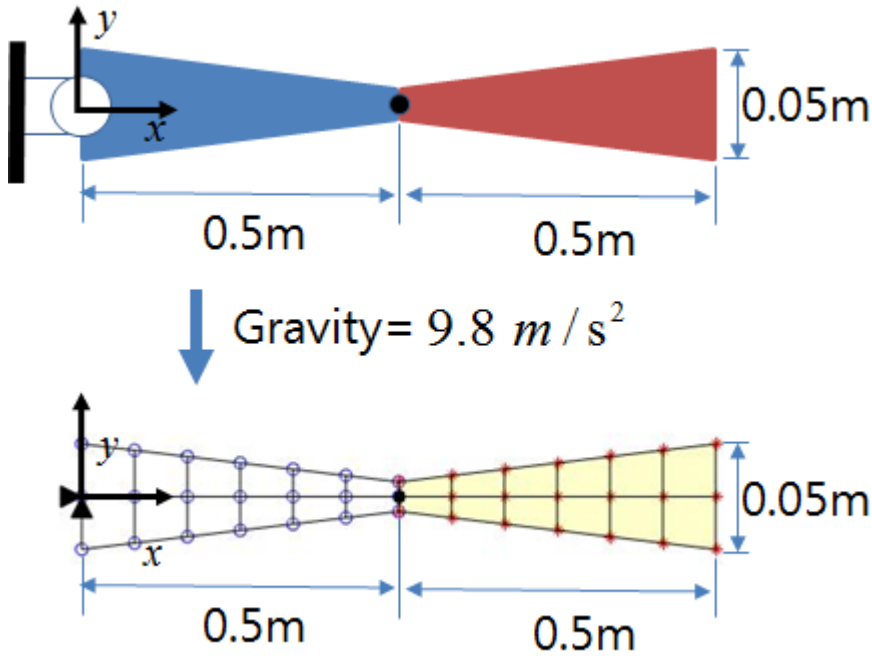

Figure 4.1. The tapered multi beam example problem to compare results of incompatible mode and C0 ANCF plane element.

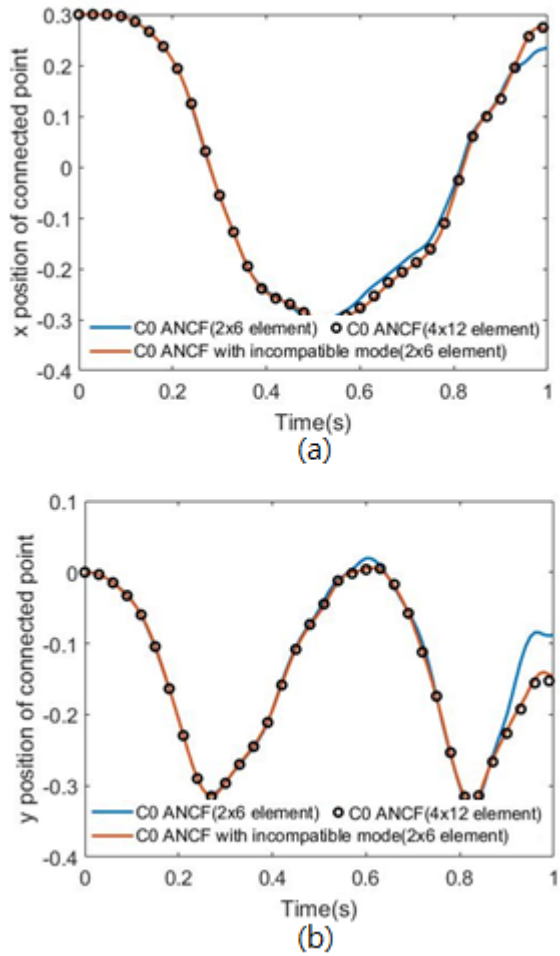

Figure 4.2. The tip position of (a) X and (b) Y direction of C0 ANCF element and incompatible mode element with same number of element and more element in C0 ANCF element.

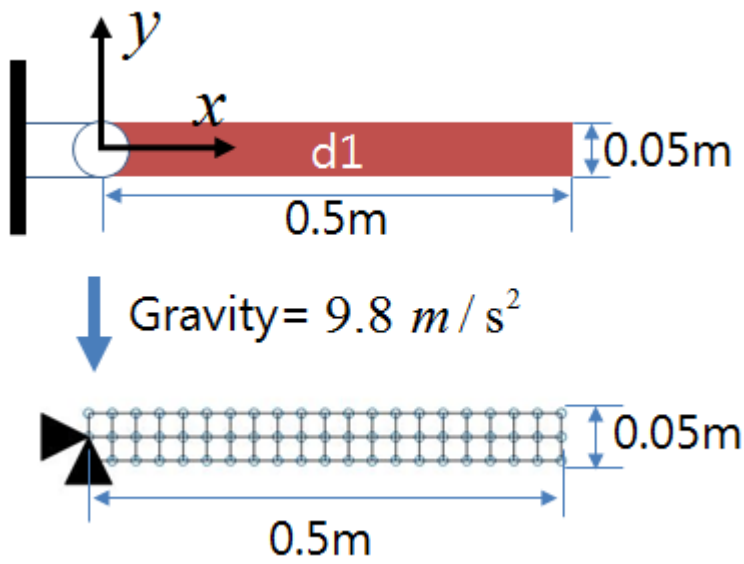

Figure 4.3. the free falling pendulum single-body numerical example problem to compare computational time of full, E-STEP and E-STEP with POD analysis

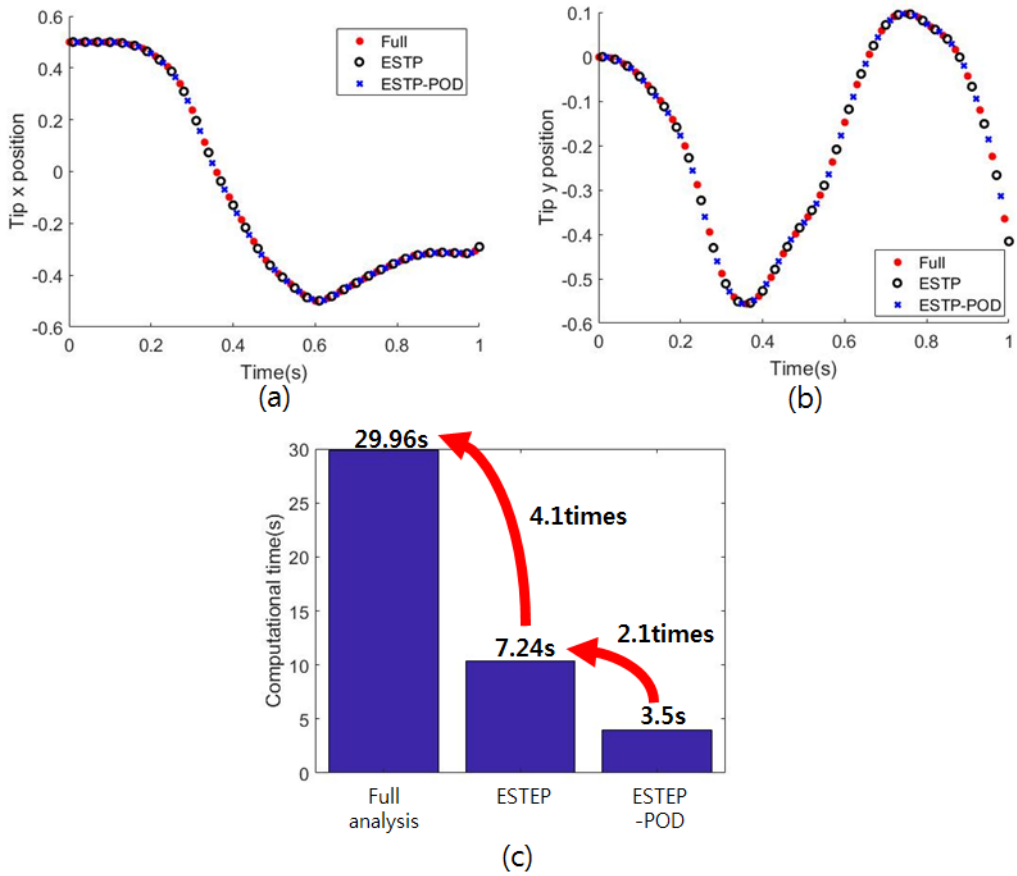

Figure 4.4. The tip position of (a) X and (b) Y direction with different analysis and (c) computational time of each analysis in one seconds simulation with one second snap shot data.

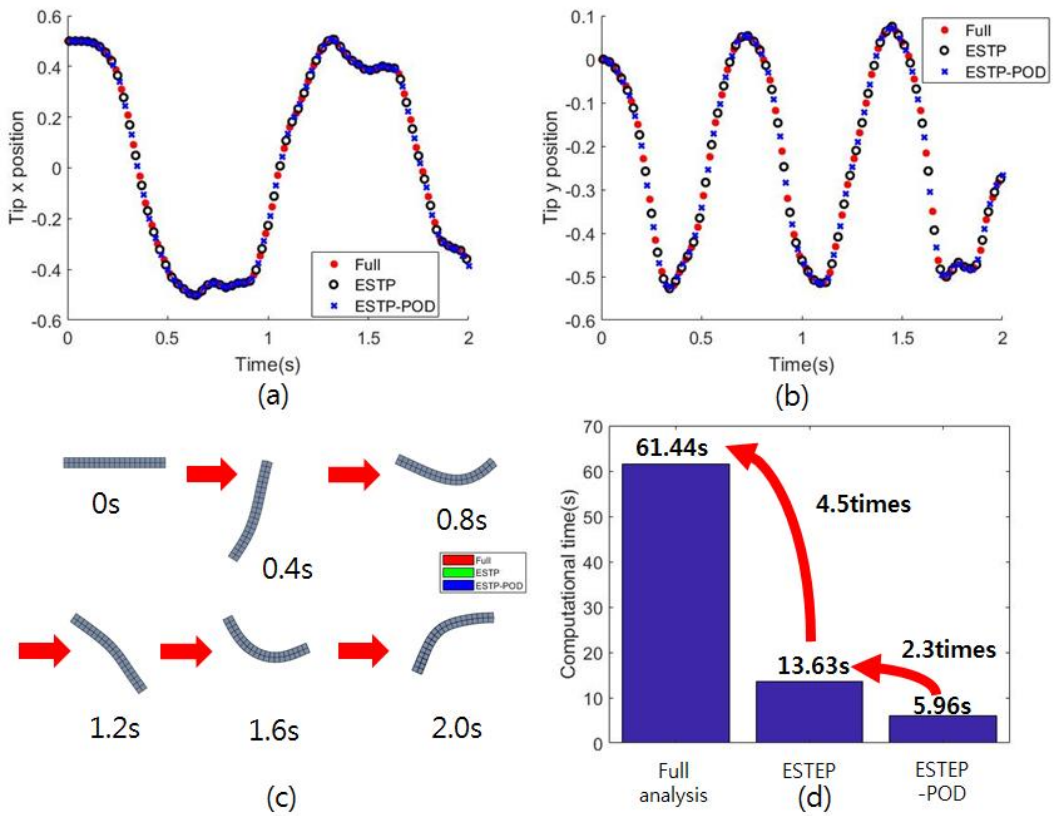

Figure 4.5. The tip position of (a) X and (b) Y direction with different analysis, (c) snapshot of deformed shape of each element, (d) computational time of each analysis in two seconds simulation with one second snapshot data.

5. Concluding remarks

In this dissertation, C0 ANCF plane and solid element, which have an only absolute position as a degree of freedom, are proposed. The existing ANCF element has a limitation because the degree of freedom of it contains the derivative of the position, that is, the slope. First, it can not use various meshes. Second, it requires a lot of computation time because there are many degrees of freedom per node. Finally, since it is a C1 formulation, it is difficult to apply it to existing commercial package. To overcome these limitations, the C0 ANCF elements are developed and research to make these elements practical is conducted.

In **Chapter 2**, the formulation process for C0 ANCF 2D plane element and 3D solid element are introduced. A method to use only absolute position per node in the existing C1 ANCF element is proposed. the time response of the structure by solving the equation of motion through the Newmark's method is observed through proposed elements. The numerical example shows that the computation time can be shortened compared to the C1 element for the same element, and the time response of the non-rectangular structure that could not be handled by the existing C1 element can be simulated with the C0 element. It is also confirmed that the total energy is conserved for the time response simulation of the conservation system. Finally, the difference between the existing C0 element, the displacement-based formulation is explained.

In **Chapter 3**, the EAS formulation is applied to the C0 ANCF elements to propose a C0 ANCF plane-beam element and a solid-shell element. Through the application

of EAS formulation, the responses to shear locking and volumetric locking are improved in the 2D plane beam element static response. In the dynamic response, convergence values are obtained using a smaller number of elements. For the 3D solid-shell element, EAS9 ~ 30 are applicable, and the difference between EAS9 and EAS21 was confirmed for static. For dynamic response, the deployment of a solar panel applicable to aerospace engineering is simulated.

In the first section of **Chapter 4**, the incompatible mode is applied to a C0 ANCF element to improve the performance. By applying the incompatible mode, the accuracy can be improved because the absolute position in the element can be represented by the second order function instead of the first order function. In tapered multi-beam dynamic simulation, improved results by applying incompatible mode can be obtained. Second, the POD method and the E-STEP method are used to shorten the calculation time. In the POD method, the computation time can be shortened by reducing the degree of freedom using the POM obtained through the SVD of the degree of freedom snapshot. In E-STEP method, the nonlinear internal force and tangent stiffness are defined as polynomial functions of degrees of freedom, and the calculation time is shortened by utilizing polynomial coefficient obtained through the snapshot. The POD method and the E-STEP method, which have the commonality of using the snapshot, are applied together to shorten the calculation time efficiently.

In this dissertation, C0 ANCF elements are developed, progressed it for universal application, and proposed methods for efficient simulation. The proposed studies can be

developed in various ways. The various formulations used in existing C0 elements such as ANS formulation or mixed formulation to C0 ANCF element can be applied to get better results than existing simulation. It can also be applied to nonlinear materials such as hyper-elastic and visco-elastic. It is also expected to be applicable to the analysis of the time response of a structure where vibrations occur through vibration simulation.

Appendix A. Gaussian quadrature

In the finite element analysis, mass, stiffness matrix and internal force are obtained through numerical integration. Numerical integration methods include trapezoidal methods, Simpson's rule, Richardson's extrapolation, adaptive integration, and Gaussian quadrature. This numerical integration can be expressed as the sum of the product of the function value of the specific point (x_i) in the integral and the weighting factor (w_i) as

$$\int_a^b f(x)dx = \sum_{i=1}^{n} f(x_i)w_i \quad \text{(A.1)}$$

In general, the specific point uses the same interval spacing point and the weighting factor is determined to integrate precisely for the n-1 order function. However, in Gaussian quadrature, the specific point and the weighting factor are determined to integrate precisely up to 2n-1 points with n points.

In the finite element method, the integration is performed by transforming an element having various shapes in global coordinate into an element of [-1,1] in natural coordinate. Therefore, the specific point, Gauss point, and the weighting factor values is determined in the interval [-1,1] of the Gaussian quadrature. For example, the process of determining the unknowns for the two point Gaussian quadrature is as follows.

1. Check the quadrature formula and the number of unknowns of two-point Gaussian quadrature.

   $$\int_{-1}^{1} f(x)dx = w_1 f(x_1) + w_2 f(x_2) \quad \text{(A.2)}$$

2. Since there are four unknowns to be determined, four conditions are required.

Since the two points have to correctly integrate the third order function, four condition can be obtained as

$$f(x)=1 \;:\; \int_{-1}^{1} 1dx = 2 = w_1 + w_2 \qquad f(x)=x \;:\; \int_{-1}^{1} xdx = 0 = w_1 x_1 + w_2 x_2$$
$$f(x)=x^2 \;:\; \int_{-1}^{1} x^2 dx = \frac{2}{3} = w_1 x_1^2 + w_2 x_2^2 \quad f(x)=x^3 \;:\; \int_{-1}^{1} x^3 dx = 0 = w_1 x_1^3 + w_2 x_2^3 \tag{A.3}$$

3. Solving the four equations in equation A.3 for four unknowns gives the gauss point and weighting factor as

$$x_1 = -x_2 = \sqrt{\frac{1}{3}}, \qquad w_1 = w_2 = 1 \tag{A.4}$$

In this way, the values for the Gauss point and the weighing factor for the n-point Gaussian quadrature method are shown in Table A.1 up to the five-point Gauss quadrature method.

Table A.1. Gauss point and weighting factor of Gauss quadrature

n	x_i	w_i
2	$\pm\sqrt{\frac{1}{3}}$	1
3	$\pm\sqrt{0.6}$ 0	5 / 9 8 / 9
4	±0.861136 ±0.339981	0.347854 0.652145
5	±0.906180 ±0.538469 0	0.236926 0.478628 0.568889

Appendix B. Newmark's time integration

To obtain the time response of a structure in a finite element dynamic simulation, the equation of motion must be solved. Since the equations of motion include the velocity of the first derivative and the acceleration of the second derivative with respect to time of the absolute position, it is necessary to numerically solve this differential equation. Newmark's method is widely used to compute this time derivative. Although it is described for displacement, because the first- and second-order derivatives of the absolute position are equal to the first- and second-order derivatives of the displacement, it can be applicable as it is to ANCF element. In Newmark's method, the velocity at time (n + 1) can be expressed by the velocity and acceleration at time (n) as

$$\dot{e}_{n+1} = \dot{e}_n + \Delta t\left[\left(1-\gamma\right)\ddot{e}_n + \gamma\ddot{e}_{n+1}\right] \tag{B.1}$$

, where γ is Newmark's parameter.

Similarly, the absolute position at time (n + 1) is

$$e_{n+1} = e_n + \Delta t\cdot\dot{e}_n + \frac{1}{2}\Delta t^2\cdot\left[\left(1-2\beta\right)\ddot{e}_n + 2\beta\cdot\ddot{e}_{n+1}\right] \tag{B.2}$$

, where β is Bemark's parameter. Newmarks parameter γ has a value between 0 and 1, and β has a value between 0 and 0.5.

The γ value is most widely used for 0.5 with the best convergence. The β value is exactly equal to the central difference method at 1/6, and generally uses 1/4, which satisfies unconditionally stability.

Appendix C. Singular value decomposition

Singular value decomposition is a method of factorizing matrix. In case of square matrix, eigenvector and diagonal eigenvalue matrix can be obtained through eigenvalue decomposition. However, non-square matrix cannot perform eigenvalue decomposition and can perform matrix factorization through singular value decomposition. If non-square m-by-n matrix is factorized by singular value decomposition, it can be expressed as

$$\underset{m\times n}{\mathbf{E}} = \underset{m\times m}{\mathbf{\Phi}}\ \underset{m\times n}{\mathbf{\Sigma}}\ \underset{n\times n}{\mathbf{V}^T} \tag{C.1}$$

, where $\mathbf{\Phi}$ is left singular vectors, $\mathbf{\Sigma}$ is singular value and $\mathbf{V}$ is right singular vectors. The left singular value is the eigenvector matrix of the m-by-m matrix, $\mathbf{E}\mathbf{E}^T$, and the right singular vectors are the eigenvector matrix of the n-by-n matrix, $\mathbf{E}^T\mathbf{E}$. The singular value matrix is a diagonal matrix with the square root of the eigenvalue of the $\mathbf{E}\mathbf{E}^T$ or $\mathbf{E}^T\mathbf{E}$. Since the left and right singular vectors are the eigenvector matrix of ETE and EET, respectively, it satisfy

$$\mathbf{\Phi}^T\mathbf{\Phi} = \mathbf{I}_m, \quad \mathbf{V}\mathbf{V}^T = \mathbf{I}_n \tag{C.2}$$

References

1. De Jalon, J. G. and E. Bayo (2012). Kinematic and dynamic simulation of multibody systems: the real-time challenge, Springer Science & Business Media.
2. Pan, W. and E. Haug (1999). "Dynamic simulation of general flexible multibody systems." Journal of Structural Mechanics 27(2): 217-251.
3. Haug, E. J. (1989). Computer aided kinematics and dynamics of mechanical systems, Allyn and Bacon Boston.
4. Schiehlen, W. (1997). "Multibody system dynamics: Roots and perspectives." Multibody system dynamics 1(2): 149-188.
5. Otter, M., et al. (1993). An object-oriented data model for multibody systems. Advanced Multibody System Dynamics, Springer: 19-48.
6. Shabana, A. A. (1997). "Flexible multibody dynamics: review of past and recent developments." Multibody system dynamics 1(2): 189-222.
7. Ambrósio, J. A. and M. S. Pereira (1994). Flexibility in multibody dynamics with applications to crashworthiness. Computer-aided analysis of rigid and flexible mechanical systems, Springer: 199-232.
8. Arsenal, R. I. (1975). "Dynamic response of a high-speed slider-crank mechanism with an elastic connecting rod." Journal of Engineering for Industry: 543.
9. Dwivedy, S. K. and P. Eberhard (2006). "Dynamic analysis of flexible manipulators, a literature review." Mechanism and machine theory 41(7): 749-

777.

10. Spong, M. W. (1987). "Modeling and control of elastic joint robots." Journal of dynamic systems, measurement, and control 109(4): 310-318.
11. Ho, J. and D. Herber (1985). "Development of dynamics and control simulation of large flexible space systems." Journal of Guidance, Control, and Dynamics 8(3): 374-383.
12. Belytschko, T., et al. (1977). "Large displacement, transient analysis of space frames." International journal for numerical methods in engineering 11(1): 65-84.
13. Ho, J. (1977). "Direct path method for flexible multibody spacecraft dynamics." Journal of Spacecraft and Rockets 14(2): 102-110.
14. Modi, V., et al. (1991). "An approach to dynamics and control of orbiting flexible structures." International journal for numerical methods in engineering 32(8): 1727-1748.
15. Gladwell, G. (1996). Solid mechanics and its applications, Springer.
16. Li, Y. (2014). "Coupled computational fluid dynamics/multibody dynamics method with application to wind turbine simulations." Renewable Energy.
17. Roberson, R. (1972). "A form of the translational dynamical equations for relative motion in systems of many non-rigid bodies." Acta Mechanica 14(4): 297-308.
18. Belytschko, T. and B. Hsieh (1973). "Non-linear transient finite element analysis with convected co-ordinates." International journal for numerical methods in

engineering 7(3): 255-271.

19. Meirovitch, L. (1974). "A new method of solution of the eigenvalue problem for gyroscopic systems." AiAA Journal 12(10): 1337-1342.

20. Song, J. O. and E. J. Haug (1980). "Dynamic analysis of planar flexible mechanisms." Computer Methods in Applied Mechanics and Engineering 24(3): 359-381.

21. Rankin, C. and F. Brogan (1986). "An element independent corotational procedure for the treatment of large rotations." Journal of pressure vessel technology 108(2): 165-174.

22. Belytschko, T. and L. W. Glaum (1979). "Applications of higher order corotational stretch theories to nonlinear finite element analysis." Computers & Structures 10(1-2): 175-182.

23. Shabana, A. A. and R. A. Wehage (1983). "A Coordinate Reduction Technique for Dynamic Analysis of Spatial Substructures with Large Angular Rotations∗." Journal of Structural Mechanics 11(3): 401-431.

24. Geradin, M., et al. (1994). Finite element modeling concepts in multibody dynamics. Computer-aided analysis of rigid and flexible mechanical systems, Springer: 233-284.

25. Bakr, E. and A. A. Shabana (1986). "Geometrically nonlinear analysis of multibody systems." Computers & Structures 23(6): 739-751.

26. Cardona, A. and M. Geradin (1991). "Modelling of superelements in mechanism

analysis." International journal for numerical methods in engineering 32(8): 1565-1593.

27. Shabana, A. A. (2013). Dynamics of multibody systems, Cambridge university press.

28. Shabana, A. and R. Schwertassek (1998). "Equivalence of the floating frame of reference approach and finite element formulations." International journal of non-linear mechanics 33(3): 417-432.

29. Shabana, A. A. (1997). "Definition of the slopes and the finite element absolute nodal coordinate formulation." Multibody system dynamics 1(3): 339-348.

30. Shabana, A. A., et al. (1998). "Application of the absolute nodal coordinate formulation to large rotation and large deformation problems." Journal of mechanical design 120(2): 188-195.

31. Berzeri, M. and A. A. Shabana (2000). "Development of simple models for the elastic forces in the absolute nodal co-ordinate formulation." Journal of Sound and Vibration 235(4): 539-565.

32. Gerstmayr, J., et al. (2013). "Review on the absolute nodal coordinate formulation for large deformation analysis of multibody systems." Journal of Computational and Nonlinear Dynamics 8(3): 031016.

33. Gerstmayr, J. and H. Irschik (2008). "On the correct representation of bending and axial deformation in the absolute nodal coordinate formulation with an elastic line approach." Journal of Sound and Vibration 318(3): 461-487.

34. Omar, M. and A. Shabana (2001). A two-dimensional shear deformable beam for large rotation and deformation problems, Academic Press.

35. Shabana, A. A. and R. Y. Yakoub (2001). "Three dimensional absolute nodal coordinate formulation for beam elements: theory." Journal of mechanical design 123(4): 606-613.

36. Dmitrochenko, O. and A. Mikkola (2008). "Two simple triangular plate elements based on the absolute nodal coordinate formulation." Journal of Computational and Nonlinear Dynamics 3(4): 041012.

37. Dmitrochenko, O. and D. Y. Pogorelov (2003). "Generalization of plate finite elements for absolute nodal coordinate formulation." Multibody system dynamics 10(1): 17-43.

38. Vaziri Sereshk, M. and M. Salimi (2011). "Comparison of finite element method based on nodal displacement and absolute nodal coordinate formulation (ANCF) in thin shell analysis." International Journal for Numerical Methods in Biomedical Engineering 27(8): 1185-1198.

39. Dufva, K. and A. Shabana (2005). "Analysis of thin plate structures using the absolute nodal coordinate formulation." Proceedings of the Institution of Mechanical Engineers, Part K: Journal of Multi-body Dynamics 219(4): 345-355.

40. Mikkola, A. M. and M. K. Matikainen (2006). "Development of elastic forces for a large deformation plate element based on the absolute nodal coordinate

formulation." Journal of Computational and Nonlinear Dynamics 1(2): 103-108.

41. Mikkola, A. M. and A. A. Shabana (2003). "A non-incremental finite element procedure for the analysis of large deformation of plates and shells in mechanical system applications." Multibody system dynamics 9(3): 283-309.

42. Abbas, L., et al. (2010). "Plate/shell element of variable thickness based on the absolute nodal coordinate formulation." Proceedings of the Institution of Mechanical Engineers, Part K: Journal of Multi-body Dynamics 224(2): 127-141.

43. Sopanen, J. T. and A. M. Mikkola (2003). "Description of elastic forces in absolute nodal coordinate formulation." Nonlinear Dynamics 34(1-2): 53-74.

44. Olshevskiy, A., et al. (2013). "Three-and four-noded planar elements using absolute nodal coordinate formulation." Multibody system dynamics 29(3): 255-269.

45. Olshevskiy, A., et al. (2014). "Three-dimensional solid brick element using slopes in the absolute nodal coordinate formulation." Journal of Computational and Nonlinear Dynamics 9(2): 021001.

46. Olshevskiy, A., et al. (2017). "Absolute nodal coordinate formulation of tetrahedral solid element." Nonlinear Dynamics 88(4): 2457-2471.

47. Kübler, L., et al. (2003). "Flexible Multibody Systems with Large Deformations and Nonlinear Structural Damping Using Absolute Nodal Coordinates." Nonlinear Dynamics 34(1): 31-52.

48. Schwab, A. L. and J. P. Meijaard (2005). "Comparison of Three-Dimensional Flexible Beam Elements for Dynamic Analysis: Finite Element Method and Absolute Nodal Coordinate Formulation." (47438): 1341-1349.

49. Wang, Z., et al. (2019). "Multiple Dynamic Response Patterns of Flexible Multibody Systems With Random Uncertain Parameters." Journal of Computational and Nonlinear Dynamics 14(2): 021008-021008-021015.

50. Ebrahimi, M., et al. (2019). "Design optimization of dynamic flexible multibody systems using the discrete adjoint variable method." Comput. Struct. 213: 82-99.

51. Otsuka, K. and K. Makihara (2018). "Deployment simulation using absolute nodal coordinate plate element for next-generation aerospace structures." AiAA Journal 56(3): 1266-1276.

52. Shabana, A. A. (2015). "ANCF Tire Assembly Model for Multibody System Applications." J. Comput. Nonlinear Dyn. 10(2).

53. Hauptmann, R. and K. Schweizerhof (1998). "A systematic development of 'solid-shell' element formulations for linear and non-linear analyses employing only displacement degrees of freedom." International journal for numerical methods in engineering 42(1): 49-69.

54. Bathe, K.-J. (1996). Finite element procedures / Klaus-Jürgen Bathe. Englewood Cliffs, N.J., Englewood Cliffs, N.J. : Prentice Hall.

55. Ahmad, S., et al. (1970). "Analysis of thick and thin shell structures by curved finite elements." International journal for numerical methods in engineering 2(3):

419-451.

56. Hughes, T. J. R. and T. E. Tezduyar (1981). "Finite Elements Based Upon Mindlin Plate Theory With Particular Reference to the Four-Node Bilinear Isoparametric Element." Journal of Applied Mechanics 48(3): 587-596.

57. Reissner, E. (1976). "On the theory of transverse bending of elastic plates." International Journal of Solids and Structures 12(8): 545-554.

58. Parisch, H. (1995). "A CONTINUUM-BASED SHELL THEORY FOR NONLINEAR APPLICATIONS." Int. J. Numer. Methods Eng. 38(11): 1855-1883.

59. Sze, K. Y. (2002). "Three-dimensional continuum finite element models for plate/shell analysis." Progress in Structural Engineering and Materials 4(4): 400-407.

60. Simo, J. and M. S. Rifai (1990). "A CLASS OF MIXED ASSUMED STRAIN METHODS AND THE METHOD OF INCOMPATIBLE MODES." Int. J. Numer. Methods Eng. 29(8): 1595-1638.

61. Simo, J. and F. Armero (1992). "GEOMETRICALLY NONLINEAR ENHANCED STRAIN MIXED METHODS AND THE METHOD OF INCOMPATIBLE MODES." Int. J. Numer. Methods Eng. 33(7): 1413-1449.

62. Simo, J. C., et al. (1993). "Improved versions of assumed enhanced strain tri-linear elements for 3D finite deformation problems." Computer Methods in Applied Mechanics and Engineering 110(3): 359-386.

63. Andelfinger, U. and E. Ramm (1993). "EAS-elements for two-dimensional, three-dimensional, plate and shell structures and their equivalence to HR-elements." International journal for numerical methods in engineering 36(8): 1311-1337.

64. Korelc, J. and P. Wriggers (1996). "An efficient 3D enhanced strain element with Taylor expansion of the shape functions." Computational Mechanics 19(1): 30-40.

65. de Sousa, R., et al. (2003). "A new volumetric and shear locking-free 3D enhanced strain element." Eng. Comput. 20(7-8): 896-925.

66. Valente, R. A. F., et al. (2004). "An enhanced strain 3D element for large deformation elastoplastic thin-shell applications." Computational Mechanics 34(1): 38-52.

67. Kim, E., kim, H and M. Cho. (2017). "Model order reduction of multibody system dynamics based on stiffness evaluation in the absolute nodal coordinate formulation." An International Journal of Nonlinear Dynamics and Chaos in Engineering Systems 87(3): 1901-1915.

68. Kim, E. and M. Cho (2017). "Equivalent model construction for a non-linear dynamic system based on an element-wise stiffness evaluation procedure and reduced analysis of the equivalent system." Computational Mechanics 60(5): 709-724.

69. Kim, E. and M. Cho (2018). "Design of a planar multibody dynamic system with

ANCF beam elements based on an element-wise stiffness evaluation procedure." Structural and Multidisciplinary Optimization 58(3): 1095-1107.

70. Chinesta, F., et al. (2011). "A Short Review on Model Order Reduction Based on Proper Generalized Decomposition." State of the Art Reviews 18(4): 395-404.

71. Silva, J. M. S., et al. (2007). Outstanding Issues in Model Order Reduction. Berlin, Heidelberg, Berlin, Heidelberg: Springer Berlin Heidelberg.

72. Muravyov, A. A. and S. A. Rizzi (2003). "Determination of nonlinear stiffness with application to random vibration of geometrically nonlinear structures." Computers and Structures 81(15): 1513-1523.

73. Mignolet, M. P., et al. (2013). "A review of indirect/non-intrusive reduced order modeling of nonlinear geometric structures." J. Sound Vibr. 332(10): 2437-2460.

74. Berkooz, G., et al. (1993). "The Proper Orthogonal Decomposition in the Analysis of Turbulent Flows." Annu. Rev. Fluid. Mech. 25(1): 539-575.

75. Kerschen, G., et al. (2005). "The Method of Proper Orthogonal Decomposition for Dynamical Characterization and Order Reduction of Mechanical Systems: An Overview." An International Journal of Nonlinear Dynamics and Chaos in Engineering Systems 41(1): 147-169.

76. Liang, Y. C., et al. (2002). "PROPER ORTHOGONAL DECOMPOSITION AND ITS APPLICATIONS—PART I: THEORY." Journal of Sound and Vibration 252(3): 527-544.

77. Noor, A. K. and J. M. Peters (1980). "Reduced Basis Technique for Nonlinear

Analysis of Structures." AiAA Journal 18(4): 455-462.

78. Wilson, E. L., et al. (1973). Incompatible Displacement Models, Elsevier Inc.

79. Taylor, R. L., et al. (1976). "A non-conforming element for stress analysis." International journal for numerical methods in engineering 10(6): 1211-1219.

80. Kožar, I., et al. (2018). "Method of incompatible modes–overview and application." Građevinar 70(01.): 19-29.

국문 요약

본 논문에서는 비선형 정해석 및 동해석을 위한 C0 연속성을 가지는 절대좌표기반요소(absolute nodal coordinate formulation (ANCF) element)를 제안하였다. 절대좌표공식요소는 절대위치와 그 미분, 즉 기울기를 자유도로 가지기 때문에 모든 자유도가 전역좌표계에 대하여 나타나게 된다. 이러한 유도방식은 동해석(dynamic simulation)에서 질량행렬이 불변한다는 이점을 가지게 된다. 하지만 미분자유도를 포함하는 기존의 절대좌표공식요소 는 C1 연속성을 만족해야하기 때문에 다양한 한계를 가진다. 다양한 요소형태를 다룰 수 없으며, 노드(node)당 자유도를 많이 가지기 때문에 요소가 증가함에따라 계산시간이 많이 필요로 하여 비효율적이다. 또한 아바쿠스(ABAQUS)나 앤시스(ANSIS)같은 상용프로그램은 C0 연속성을 가지는 요소로 문제를 다루는 경우가 많기 때문에 상용프로그램에 적용하거나 다른 요소들과 결합하여 사용하기에 용이하지 않다. 이러한 한계를 극복하기위해 절대좌표공식요소의 C0 유도과정을 본 논문에서 제안하였다.

먼저, 2차원 평면요소와 3차원 C0 ANCF 2차원 평면 요소와 3차원 고체 요소를 기존의 C1 ANCF 요소에서 노드당 자유도로 절대 좌표만을 사용하는 방법으로 공식화하였다. 뉴마크스 (Newmark's) 방법을 통해 운동방정식을 풀어 구조물의 시간에 따른 변형을 수치예제를 통해 검증하였다. 또한, C0 요소로 기존 C1 요소에서 다룰 수 없었던 직사각형이 아닌 구조몰에 대한 동해석을 수행 할 수 있었다. 제안된 요소를 통해 보존계문제에 대한 동해석 결과 전체에너지가 시간에 따라 보존되는 것을 확인할 수 있었다. 또한 기존의 C0 요소인

변위기반공식과의 차이를 설명하였다.

다음으로, 강화된변형률(enhanced assumed strain (EAS)) 공식을 C0 ANCF 평면 및 고체 요소에 적용하여 평면-빔(plane-beam)요소와 고체-쉘(solid-shell)요소를 제안하였다. EAS공식 적용을 통하여 2차원 평면-빔 요소의 정해석 문제에서 전단 잠금과 체적잠금에 대한 해석이 개선되었다. 동해석 에서는 더 적은수의 요소를 사용하여 수렴값을 얻을 수 있었다. 3차원 고체-쉘요소에서는 정해석에 대해 다른 개수의 EAS변수를 사용하여 결과를 비교하였고, 동해석에 대하여 실제 태양전지전계문제를 통해 검증하였다.

마지막으로 C0 ANCF 요소의 성능향상을 위한 연구를 진행하였다. 첫번째로 비호환모드(incompatible mode)를 적용하였다. 요소내의 절대좌표값을 2차 함수인 비호환모드를 적용하여 시뮬레이션 정확도를 향상하였다. 두번째로는 직교 분해 축소법(proper orthogonal decomposition reduction method)과 요소별 강성평가 방법(element-wise stiffness evaluation method)을 통해 계산시간을 단축시켰다. 직교분해축소법에서는, 시간에 따른 절대좌표정보의 특이값분해를 통해 직교모드와 특이값을 구하여 운동방정식의 자유도를 축소하여 계산시간을 단축하였다. 요소별강성평가방법에서는, 절대좌표와 내력의 정보를 통해 비선형 내력과 강성행렬을 절대좌표의 함수가 되도록 하여 계산시간을 단축하였다. 두 방법을 함께 사용하여 효율적으로 계산시간을 단축하였다.

주요어: 다물체동역학, 절대좌표공식, 유한요소해석, 고체－쉘요소, 축소모델

학번: 2013－22497